Design and Optimization of Dielectric Metasurface Optics

Alan Zhan

A dissertation
submitted in partial fulfillment of the
requirements for the degree of

Doctor of Philosophy

University of Washington

2019

Reading Committee:

Arka Majumdar, Chair

Kai-Mei Fu

Silas Beane

Boris Spivak

Program Authorized to Offer Degree:
Physics

University of Washington

Abstract

Design and Optimization of Dielectric Metasurface Optics

Alan Zhan

Chair of the Supervisory Committee:
Assistant Professor Arka Majumdar
Department of Physics

In recent years, sub-wavelength, aperiodic gratings, currently coined metasurfaces have the potential to manipulate electromagnetic fields with extreme control in a remarkably small form factor. These planar optical components promise to manipulate incident fields at the wavelength scale to achieve unprecedented functionalities. This extraordinary flexibility arises from the extremely large numbers of tunable degrees of freedom characterizing the individual discrete scatterers. This thesis details two methods for the design of these optical elements, a forward method, and an inverse method. First, a forward design method is described for metasurfaces based on a silicon nitride nanopost platform. Results from experiments characterizing metasurface lenses, vortex beam generators, cubic phase plates, and Alvarez lenses are presented. These optical elements were all designed to operate in the visible frequencies, and fabricated using conventional top-down semiconductor lithography. Then, a general inverse design method is described for discrete spherical scatterer based optical elements. Simulation results for single layer and multilayer lenses for fabrication using a 3D printer are shown, and simulation and experimental results for a novel optical element producing a discrete helical focusing pattern is presented.

TABLE OF CONTENTS

LIST OF FIGURES

LIST OF TABLES

ACKNOWLEDGMENTS

The University of Washington, Seattle has been an incredible place for me to spend these five years in graduate school. Though there are many people here who have greatly contributed to my personal development, I reserve the greatest thanks for Professor Arka Majumdar, who is both an incredible advisor and great friend. During my time in his lab, he exposed me to a great deal of academic research, supported my sometimes questionable efforts, and gave me the freedom to pursue the projects I enjoyed. His unfaltering enthusiasm and insatiable curiosity for science and engineering is infectious and cultivated a positive, creative environment where I was able to develop greatly as a scientist and researcher. His personal investment, positive attitude, and care for his graduate students motivated me to push through failure, and also success. For all of this, I will always be grateful.

Numerous faculty here in Seattle have helped me develop throughout these years. I would like to thank specifically my thesis committee members, Professors Kai-Mei Fu, Silas Beane, Boris Spivak, and Joshua Vaughan. I am very grateful for all of your time, our conversations, and your advice. I would also like to acknowledge all of the staff, past and present I have had the pleasure of working at the Washington Nanofabrication Facility with including Dr. Darick Baker, Dr. Andrew Lingley, Shane Patrick, Duane Irish, Rick Bojko, Mark Morgan, and the others who maintained the facility. Without your help at the cleanroom, none of this would have ever been possible. I would also like to thank the collaborators I have had the pleasure of working with, Josh Hendrickson, Ricky Gibson, Evan Smith, and Rahul Trivedi. Thank you for your patience. Lastly, I would like to thank the developers and maintainers of CELES, Amos Egel and Lorenzo Pattelli who allowed me to contribute to the great software, and also introduced me to Mie theory, which became an integral part of my later research.

The NOISE lab, formerly the IQO lab has been a great part of my life throughout my time here in Seattle, and I thank them for tolerating my presence for the past five years. In particular I would like to thank Dr. Taylor Fryett, who not only introduced me to the cleanroom and the lab, but also tolerated all of the poor jokes I have made in these five years, and answered an endless amount of coding and photonics questions. I never would have been able to complete this without his help. I would like to thank Dr. Christopher Dodson, our first postdoc who taught me a great deal of optics, and gave me invaluable advice that I would lean on throughout my PhD. Those baseball and basketball conversations were a great way to destress from the torrent of physics homework and lab work. I am grateful towards Shane Colburn, the first graduate student to join me in the metasurface arm of the group. Thank you for getting RCWA to work, for propelling the metasurface research to new heights, and for all of the conversations we had throughout my time in the lab. Thank you Jiajiu Zheng for teaching me so much about integrated photonics, and managing the group meetings. Thank you Elyas Bayati for all of the energy and added positivity you bring to the group. Thank you Yueyang Chen for all of the conversations we had about basketball and research. I hope Houston wins a championship soon for you! I give my appreciation to James Whitehead for enduring my banter through undergraduate and actually joining us as a graduate student. Thank you for fabricating my structures! Of the first years, I have a sincere appreciation for Maksym Zhelyeznyakov for continuing the work that I began. I have greatly enjoyed the company of Chuchuan Hong, Dan Guo, Jacob Waelder, Chang-hua Liu, David Rosser, Luocheng Huang, Abhi Saxena, Roger Fang, Shreyas Shah, Albert Ryou, Zane Peycke, Shana Odem, Michael Choquer, and Peiping Xu.

I owe a tremendous debt to the professors and colleagues from the University of California, Santa Barbara. These people are too numerous to count, but in particular, I would like to thank Professor Dirk Bouwmeester, for inspiring me to continue in scientific research, and teaching me how to be a researcher. The two years I spent in your lab were incredible,

and I am still in awe of your patience, kindness, and scientific rigor. I would also like to thank Professor Harry Nelson, who was the man who inspired me to major in physics as an undergraduate. Thank you Nelson, for all of the enthusiasm and care you showed to an incoming undergraduate who was unprepared for a physics education. I would also like to thank Dr. Jenna Hagemeier for guiding me through undergraduate research in Dirk's lab. Thank you for your patience and kindness in dealing with a clueless undergraduate. I would like to thank Dr. Ajit Barve for your patience for me, and teaching me so much about III-V epitaxy and device design. Lastly, I would like to thank my Santa Barbara cturtles, Bert, Adam, Scott, Will, and Ramon.

My friends in Seattle are irreplacable, and I would like to thank Alex Peek, Robert Waite, Alek Zhang, Harrison Goldwyn, Claire West, Mike Wilensky, and Emily Rabe for their support. My family has always been a great support to me in my endeavors, and I would like to thank my dad, Cixiang Zhan, my mom, Xianai Meng, my sister, Lucy Zhan, and her newborn son, my cousin Chris. Last, but not least, I would like to thank my girlfriend Katy Johnson for listening to my problems, and supporting me through the home stretch.

Throughout my life I have been gifted with incredible friends and family. For all of this I believe I have become a better researcher, brother, son, friend, and human being. I hope that as this chapter of my life comes to a close, I will be able to count on all of you to support me through the next.

DEDICATION

To my friends and family: past, present, and future.

Chapter 1

INTRODUCTION

The human fascination with understanding and manipulating light dates back to early antiquity, with the polishing of obsidian to create mirrors possibly dating back to as early as 6000 BC in ancient Anatolia [2]. References to a lens or "burning stone", another fundamental optical element can be found on ancient Egyptian hieroglyphs from 800 BC [3]. The discovery and use of these ancient devices often preceded a concrete physical understanding of the relevant physics, which today are the concepts of refraction and reflection.

Much of the early development of geometric optics can be attributed to early Greek and Islamic scholars such as Euclid and Ibn al-Haytham. Euclid treated vision geometrically, and formalized the use of lines (or rays) and angles to describe properties of magnification. Ibn al-Haytham produced a theory of vision based on Euclid's rays, and physically associated these rays with light and color [4]. A theory of geometric optics mediated by minute particles was later formalized by Isaac Newton, and its failures to describe interference and diffraction were experimentally documented by Francesco Grimaldi, James Gregory, and Thomas Young. Christiaan Huygens and later Francois Arago and Augustin-Jean Fresnel theoretically described these phenomenon using a wave theory of light. Finally, when wave optics was unified with the theory of electromagnetism, a modern understanding of light or physical optics emerged.

Utilizing the results of the experimental and theoretical knowledge on the principles of optics, scientists and engineers developed impressive optical systems such as the microscope, telescope, and spectrometer to further research in other fields such as biology and astronomy. In addition, this research has enriched every day life by producing more practical gadgets

such as reading glasses, polarized sunglasses, and 3D television. Since our initial curiosity with luminosity, research in optics has allowed us to study length scales that are ludicrously large and surprisingly small. In astronomy, the use of adaptive optics has allowed ground based telescopes to correct for aberrations originating from atmospheric turblence to accurately locate stars [5]. In biology, numerous microscopy methods have been developed to obtain images at a higher resolution than allowed by the diffraction-limit [6]. This thesis focuses on extending this entire body of work using dielectric metasurfaces that allow for both miniaturization and increased functionality when compared to traditional refractive or diffractive optics.

1.1 Introductory Optics

While today's optical systems have impressive performance and functionality, they are still largely composed of elements morphologically identical to the lenses and mirrors of antiquity, or 'bulk' optics. While our prowess at polishing smooth surfaces has improved significantly compared to our ancestors, the function and form factor of these bulk optics is still intrisically tied to the geometry of its surface, and is ultimately constrained by Snell's law, or the law of reflection.

As an example, we consider normally incident monochromatic light on a plano-convex spherical lens. We can understand its function using two complementary approaches, ray or wave optics. Using ray optics, we can consider an incident bundle of rays, and use Snell's law to calculate the deflection of each ray as it transmits across the spherical interface. Based on these deflections, we can then calculate the trajectory of the ray and see that it focuses most of the rays at the focal point.

Using wave optics, we dispense with the notion of the incident light as a bundle of rays, and instead consider it to be a planar wavefront with some characteristic wavelength λ. As the wavefront propagates through the bulk of the optical element, it travels some optical path length $d_{OPL} = n_1 d$ where n_1 is the refractive index of the optical element, and d is the thickness, and accrues a spatially varying phase delay $\phi_{delay} = \frac{2\pi n_1 d}{\lambda}$. After the wavefront

exits the optical element, there is a spatially varying delay imprinted on the wavefront corresponding to the spherical surface. Using Huygen's principle, we can conceptualize our system as a planar surface with spherical point sources radiating with a spatially varying phase delay, and the far field output can be understood as the interference of these point sources.

In this manner, wave optics opens a larger design space by allowing us consider systems that do not correspond to a smooth geometric surface. Instead, we abstract our optical system to that of a planar surface imposing some spatially varying phase delay. This more general model of optical elements as wavefront shaping is an idealized version of a gradient metasurface, and its use is the basis of the first chapter of the thesis.

1.2 Metasurfaces Optics

As mentioned previously, the function of bulk optics is determined by the geometry of the surface. Metasurfaces, or metastructures as they are currently deemed, are typically systems composed of discrete electromagnetic scatterers arranged on a sub-wavelength two dimensional grid [1, 7]. These large grids of discrete electromagnetic scatterers have received renewed interest during the last decade [8–11] due to their unprecedented ability to control the propagation of light on a form factor with wavelength-scale thickness. Their unique flexibility arises from the large numbers of degrees of freedom that characterize the system, as each discrete scatterer on the lattice can be individually tuned to locally control the phase and amplitude of a scatterered wave. Metasurface optics, like many other fields has been researched under many different names throughout its history including, but not limited to zero-order diffraction gratings, sub-wavelength gratings, high contrast transmit arrays, metasurfaces, and metastructures. To this end, I have included a brief summary of the history of the field.

1.3 A Multi-Faceted History

In the optical regime, the study of metasurface optics began under the context of zeroth order, or sub-wavelength diffraction gratings in the early 1990s. These dielectric optical elements were generally arrays of one-dimensional structures or binary gratings with sub-wavelength period. Of particular interest was their ability to suppress all orders of diffraction except the zeroth order [12]. In these initial studies, the dimensions of the nanostructures were changed to produce a linear phase ramp to act as a beam deflector [12, 13]. The sub-wavelength binary gratings were modeled as a graded index grating, where increasing the duty cycle of the grating also increased the local refractive index. This modeling of the devices using effective medium theory (EMT) was qualitatively correct [14,15], though the periodicities of the structures were at the edge of the theory's valid length-scale [16]. It is also interesting to note that due to the fabrication difficulties at the time, in their manuscript, W. Stork et al. experimentally demonstrated the diffraction suppressing properties of sub-wavelength gratings with water waves, rather than optical waves [12].

The early results from the early 1990s were later extended to handle two-dimensional structures such as cyindrical pillars by the mid 1990s, and there were early optical demonstrations of reflective [17], and transmissive diffractive optical elements [14, 18–21]. In general, these devices were fabricated either using a relatively low-refractive-index material such as quartz [17–19], or a high-index material such as titanium oxide [14, 20, 21]. The higher-refractive index of titanium dioxide resulted in higher-performance optical elements, superior to those of conventional blazed gratings [20]. The realization that these binary elements could offer efficiencies higher than those of conventional optics was a relative surprise, as the EMT used at the time did not predict such high efficiencies. An immediate promising application that is still the subject of research today was the design of highly efficient compact high numerical aperture (NA) diffractive lens [20, 21]. Conventional blazed gratings used for diffractive optical element (DOE) design proved unsuitable for efficient high NA operation due to a shadowing effect [22]. Using rigorous coupled wave analysis (RCWA) [23], Lalanne et

al. were able to reconcile the efficiencies resulting from using high refractive index materials, and identified coherent waveguiding within the dielectric nanostructures as the cause [22,24]. When compared to conventional blazed gratings, these flat binary gratings did not exhibit a shadowing effect on neighboring gratings [22], thus efficient high NA diffractive lenses were possible.

In parallel to this body of work based on using binary sub-wavelength gratings as waveguides to accrue phase, the Panchatnaram-Berry (PB) phase [25, 26] was adapted to optical systems [27, 28]. Optical elements based on the PB phase encode phase information in the polarization of incident light. By locally manipulating the polarization of the incident field, they imprint a spatially varying phase that is purely geometric, and not explicitly dependent on an optical path length difference. Though fabrication difficulties limited these elements' operation to 10.6 μm [27, 28], the principle still holds for the visible and near-infrared wavelengths of interest today.

Thus, it is fair to say that by the early 2000s, the two dominant models for the operation of dielectric metasurfaces had been developed. Optical waveguiding through the dielectric structures had been studied by Lalanne et al [22,24], and the adaptation of PB phase to subwavelength gratings had been performed by Hasman et al [27,28]. This comprehensive body of research now serves as the foundation upon which this thesis and the field of metasurface optics builds.

The field has been more recently reinvorgated by contributions from another scientific community, namely that of metamaterials [29, 30] or designed three-dimensional arrays of electromagnetic scatterers, from which the term metasurface derives. The Capasso and Shalaev groups reduced the complexity of metamaterials to two dimensions, and were able to demonstrate anomalous refraction and a vortex beam plate using engineered plasmonic antennas [7, 11]. The use of metallic scatterers with their high refractive index contrast allowed these plasmonc antennas to be much thinner than the operating wavelength [7, 11]. The operating principles of these metallic antennas are understood as interference between the scattered fields from different plasmonic resonant modes. These highly compact arrays

of metallic scatterers have been used for devices such as lenses [31], axicons [32], holograms [33, 34]. However, due to the intrinsic ohmic losses of metallic resonators, efficient devices were limited to infrared wavelengths or in reflective configuration [1].

In the past decade, sub-wavelength gratings have been shown to be capable of mimicking existing optical elements such as lenses [1, 31, 35–43], beam deflectors [44, 45], axicons [32], freeform optics [46, 47], retroreflectors [48], holograms [33, 34] and polarization optics [49, 50], in addition to producing unprecendented functionalities such as multiplexed holograms [49, 51], achromatic operation [52–56], controlling the Brewster effect [57], integrated spectrometers [58], and new wave-front coding systems [59–61]. In addition to stand alone elements, metasurfaces have also been integrated into optical systems consisting of multiple elements in tandem demonstrating a camera system [62], retroreflector [48], and varifocal systems [63].

1.4 Thesis Outline

This thesis concerns itself with methods of designing and optimizing complex arrays of discrete scatterers, and experimental demonstrations of these methods. Specifically, it covers the forward and inverse design of discrete-scatterer-based optics with relatively low-refractive-index materials. It is organized in chronological order in order to provide the reader with a coherent understanding of the motivations and challenges behind the research. Chapters two and three focus on the use of the standard forward design method, and presents metasurface optics based on a silicon nitride platform. Chapters four and five focus on the development of an inverse design methodology based on spherical scatterers capable of simulating and optimizing large arrays of spherical scatterers. Finally, chapter six focuses on a generalization of the method presented in chapters four and five to scatterers of an ellipsoidal geometry.

- Chapter 2 focuses on the forward design methodology used to design metasurfaces composed of cylindrical silicon nitride nanoposts for operation in the visible wavelengwth regime. We use RCWA to compute the scattering properties of these scatterers, and

use them to implement a lens and vortex beam generator. The design method, and characterization of the optics is presented. During the research that culminated in this chapter, the contemporary metasuface community had not explored lower refractive index materials. In order to enable high efficiency operation, materials that are transparent at visible wavelengths, which generally have low refractive indices must be used. Previous demonstrations around the same time period had generally been based on silicon or noble metal platforms. It is important to note that as mentioned in the previous historical overview, during the late 1990s there was a large amount of work based on titanium oxide devices highly analogous to metasurfaces for visible wavelengths.

- Chapter 3 focuses on the forward design methodology applied towards freeform elements. While metasurfaces show promise in designing rotationally symmetric elements, they also excel in designing elements with asymmetric forms. We present dielectric metasurface element analogues of a cubic phase plate and the Alvarez lens. This work presented the first explicit demonstration of the compatibility of metasurface optics for adapting freeform optical systems. In particular, we demonstrated one of the first dynamic, compound metasurface optical systems in the Alvarez lens.

- Chapter 4 focuses on the inverse design methodology used to design discrete-scatterer-based optics composed of spherical polymer resist scatterers for near-infrared wavelengths. Generalized multi-sphere Mie theory (GMMT), or alternatively generalized Lorenz-Mie theory (GLMT), is used as the basis for implementing an adjoint gradient-based inverse-design method. Singlet and doublet lenses are simulated and their theoretical performance is characterized. The method is then validated using finite-difference time-domain method (FDTD) simulations. This project was primarily motivated by a fundamental issue of simulating large metasurface systems as the simulation of large metasurfaces were either accurate, but limited by memory scaling issues (FDTD), or fast, but abstracted away too much of the physics (phase profile). The

use of GMMT serves as a middle ground between full-wave electromagnetic solvers and the phase profile abstraction model. With an efficient forward-simulation method developed, we were able to develop an efficient inverse-design method.

- Chapter 5 focuses on an experimental demonstration of the methodology presented in Chapter 4. A discrete spherical scatterer based optic is demonstrated that is capable of focusing light into a discrete helical pattern along the optical axis. This optical element is fabricated using a Nanoscribe GT two photon lithography system. In this work, we sought to fully demonstrate the advantages that Chapter 4 claimed in the design of a large-scale metasurface with a non-trivial function that would be difficult to design using forward-design methods.

- Chapter 6 focuses on a work extending the inverse-design methodology of Chapter 4 to scatterers of ellipsoidal geometry using T-matrix theory. The derivation of the derivative scattering matrices for ellipsoidal particles, and a demonstration of the accuracy of the method is presented. The restriction to spherical scatterers is a fairly serious drawback to the method presented in Chapter 4 and demonstrated in Chapter 5. Fortunately, the T-matrix method or extended boundary condition method provides a straightforward extension to non-spherical scatterers that is also easily parallelizable, offering a truly scalable way to simulate large-scale metasurfaces.

- Chapter 7 is the conclusion and outlook, and covers some of the outstanding challenges facing metasurface optics from both a design and device perspective. In particular, it discusses high corrected metalenses, inverse design, volume optics, and dynamic metasurfaces.

Chapter 2

SILICON NITRIDE METASURFACE FORWARD DESIGN

In this chapter, we use the tried-and-true forward method that is central to metasurface optics design. While the method has been extended to implement many different functionalities, the basic idea remains the same. Using this method, we implement visible wavelength metasurface analogues of existing optical elements such as lenses and vortex beam generators. First, we introduce the idealization of a metasurface as a phase modulation plate. Then, we review the forward design process, including parameter search using rigorous coupled-wave analysis (RCWA), the phase to metasurface mapping method, and the characterization of these elements using small-scale simulations via the Lumerical implementation of the finite-difference time-domain (FDTD) method. Finally, we show the fabrication process and steps used, and characterize the performance of these optical elements experimentally. This chapter presents work that contributed to and composed reference [63].

2.1 Motivation

The miniaturization and functionality of current optical sensors is largely limited by the size of optical components. Conventional transmissive macroscopic optical elements primarily depend on the principle of refraction to control light propagation. These refractive elements rely upon their exact surface curvature and their spatial extent in order to achieve gradual phase accumulation. This places fundamental and practical limitations on their miniaturization and their available functionalities. The limitation on miniaturization is the trade off between the volume and weight of the optical package. For the case of a plano-convex lens, we can characterize the system size as the sum of the focal length and the length of the lens along its optical axis. To decrease the system size, we must decrease the radius of curvature

of the lens, but this in turn causes the weight of the optical package to increase, as more material is now required for the lens. The limitation on achievable functionalities is also based on the curvature. Implementing an arbitrary phase mask requires extremely accurate control of the surface profile of a lens that is currently not practical for mass production, or for small scale elements.

Metasurface optics are curvature agnostic, and readily accept any arbitrary phase profile. This flexibility allows metasurface optics to eliminate the trade off in miniaturization, as any optical element, independent of its focal length, will have negligibly different weights and physical sizes. In addition, metasurfaces are compatible with conventional top-down lithography techniques, allowing for production to be scaled up with current technologies. Specifically, we chose to produce analogues of conventional hyperbolic singlet lenses and vortex beam generators using metasurfaces based on silicon nitride for the visible spectrum. Previous demonstrations of high quality metasurface lenses were produced using noble metals [31,32,34], amorphous silicon [1,49], and titanium oxide [20], but the first two materials have significant absorption loss in the visible spectrum, and titanium oxide is complex metal oxide semiconductor (CMOS) incompatible. Demonstrations of silicon dioxide lenses [19], which are transparent at the visible frequencies had been reported, but they had low numerical apertures and resulted in large beam spots.

2.2 Idealized Model

Metasurface optics are a class of diffractive optics that operate by modulating the amplitude and/or phase of the incident wavefront. As our work is focused on high-efficiency optics, we focus on modulating only the phase and maintaining near-unity amplitudes. This simplification allows us to idealize a perfect metasurface as a two-dimensional phase plate. By modifying the spatial phase distribution of the phase plate, we can control the intensity pattern in the far field. The first step to converting a traditional optical element to a metasurface is to identify the phase profile associated with that specific function. Using wave optics, the phase profile for a hyperbolic lens in radial coordiantes for a given wavelength λ

and focal length f is given by:

$$\phi_{lens}(r,\theta) = \frac{2\pi}{\lambda}(\sqrt{r^2+f^2} - f), \tag{2.1}$$

where r is the radial coordinate. Then, a focusing vortex beam generator with the same parameters, and associated with a winding number l is given by:

$$\phi_{vortex}(r,\theta) = \frac{2\pi}{\lambda}(\sqrt{r^2+f^2} - f) + l\theta. \tag{2.2}$$

With these specified phase profiles, we can use the angular spectrum method [64] to compute the electric field distribution at a specific plane z_f produced by a plane wave with some wavelength λ incident on a phase distribution $\phi(r,\theta)$. The angular spectrum method decomposes any field into a basis of plane waves and allows us to propagate fields forward or backward through a homogeneous medium. Given some complex initial field $\mathbf{E}(x,y,z_0)$ defined at some plane z_0, we can express its Fourier dual as $\hat{\mathbf{E}}(k_x,k_y,z_0)$ using the Fourier transform:

$$\hat{\mathbf{E}}(k_x,k_y;z) = \frac{1}{4\pi^2}\iint_{-\infty}^{\infty}\mathbf{E}(x,y,z)e^{-i[k_x x+k_y y]}\,dx\,dy, \tag{2.3}$$

where both integrals are performed over all space, and similarly the inverse Fourier transform:

$$\mathbf{E}(x,y,z) = \iint_{-\infty}^{\infty}\hat{\mathbf{E}}(k_x,k_y;z)e^{i[k_x x+k_y y]}\,dk_x\,dk_y, \tag{2.4}$$

where now both integrals are performed over all k-space. The above is generally true for any $\mathbf{E}(x,y,z)$, but to continue we make the assumptions that the transverse plane containing the coordinates x and y consists of a homogeneous, isotropic, nonmagnetic, linear medium that is source free. We can then enforce that this field is a solution to the vector wave equation:

$$\nabla^2\mathbf{E} = \epsilon_r\mu_0\epsilon_0\frac{\partial^2\mathbf{E}}{\partial t^2}, \tag{2.5}$$

where μ_0 and ϵ_0 are the permeabilty and permittivity of free space, and ϵ_r is the relative permittivity of the material. Using the relative permttivity we can define a refractive index $n = \sqrt{\epsilon_r}$. Then a time harmonic field with time dependence $e^{-i\omega t}$ for some given angular frequency ω must satisfy the vector Helmholtz equation:

$$(\nabla^2 + k^2)\mathbf{E} = 0, \tag{2.6}$$

where we have defined $k = n\omega/c$ as the wave vector. Using the relation:

$$k^2 = k_x^2 + k_y^2 + k_z^2, \tag{2.7}$$

and inserting our Fourier representation (2.3) into the Helmholtz equation (2.6), we find a relation between two Fourier planes:

$$\hat{\mathbf{E}}(k_x, k_y; z) = \hat{\mathbf{E}}(k_x, k_y; 0)e^{\pm ik_z z}. \tag{2.8}$$

Finally, inserting the relation between different Fourier planes (2.8) into our real space definition (2.4), we arrive at the angular spectrum representation:

$$\mathbf{E}(x, y, z) = \iint_{-\infty}^{\infty} \hat{\mathbf{E}}(k_x, k_y; 0)e^{i[k_x x + k_y y \pm k_z z]}\, dk_x\, dk_y, \tag{2.9}$$

where the $\pm$ indicates we are allowed to propagate both in the forward and backward directions. Using this representation, we can quickly calculate the far field corresponding to a plane wave incident onto some arbitrary phase plate by defining $\mathbf{E}(x, y, 0) = e^{i\phi(x,y)}$. This ideal model of a metasurface serves as the reference to which we compare our full wave electromagnetic simulations.

2.3 Forward Design

With this idealized model, we can quickly check if the phase profiles we use correspond to the desired optical functions. After validating our phase profiles, we now describe the forward design procedure we use to implement them using our arrays of dielectric scatterers. This process includes selecting the appropriate material platform, performing electromagnetic simulations to determine the parameters of the scatterers needed to implement the phase profile, and finally validating the metasurface using a full-wave, electromagnetic solver.

2.3.1 Material Selection

The first step is to choose the material platform the metasurface will be fabricated on. The main goal for this work was to produce efficient metasurfaces operating in the visible wavelength regime. To do this, we used plasma-enhanced chemical vapor deposition (PECVD)

silicon nitride as it has a wide band gap E_g around 4.5 eV (depending on its silicon to nitride ratio), a refractive index of $n = 2$, and is CMOS compatible. In addition, its deposition and etching recipes were readily available in the Washington Nanofabrication Facility (WNF) cleanroom. The wide band gap ensures full transparency of the metasurface over the entire visible spectrum, and the high refractive index allows us more flexibility in parameter choice than silicon oxide ($n\widetilde{=}1.45$) [22]. It's CMOS compatibility allows for its processing to be scaled to existing commerical foundries. Our substrate was chosen to be a fused quartz or silica wafer.

2.3.2 Parameter Search

With our material selected, we need to find a suitable family of dielectric scatterers to implement our metasurface. Following the lead of a previous demonstration in amorphous silicon [1], we chose to use cylindrical pillars. The primary building block of a metasurface is a grating composed of scatterers arranged on a periodic lattice with period p, and thickness t as shown in Figure 2.1. When the period p of the lattice is sub-wavelength, all orders of diffraction higher than the zeroth become evanescent. The complex transmission amplitude of the scattered plane wave depends on the grating periodicity p, the scatterer dimensions (thickness t, and diameter d), and the refractive index n. In general, implementing a metasurface requires selecting the correct geometric and material parameters to achieve a full range of phase shifts from 0 to 2π, while maintaining a high transmission amplitude.

Using RCWA, we were able to find suitable sets of parameters to achieve the required phase range, while maintaining high transmission amplitudes. In these simulations, we calculate the complex amplitude coefficient by varying the diameter d of the posts with refractive index $n = 2$ for a fixed periodicity p, substrate thickness $t_{sub} = \lambda$, and substrate refractive index $n_{sub} = 1.45$. We found that by varying the thickness and periodicities of the posts, we were able to transition between a resonant regime where the simulated lattice exhibits guided-mode resonances, or a nonresonant regime where there exists no guided-mode resonances as shown in Figures 2.2j and k. In general, the nonresonant regimes had the attractive

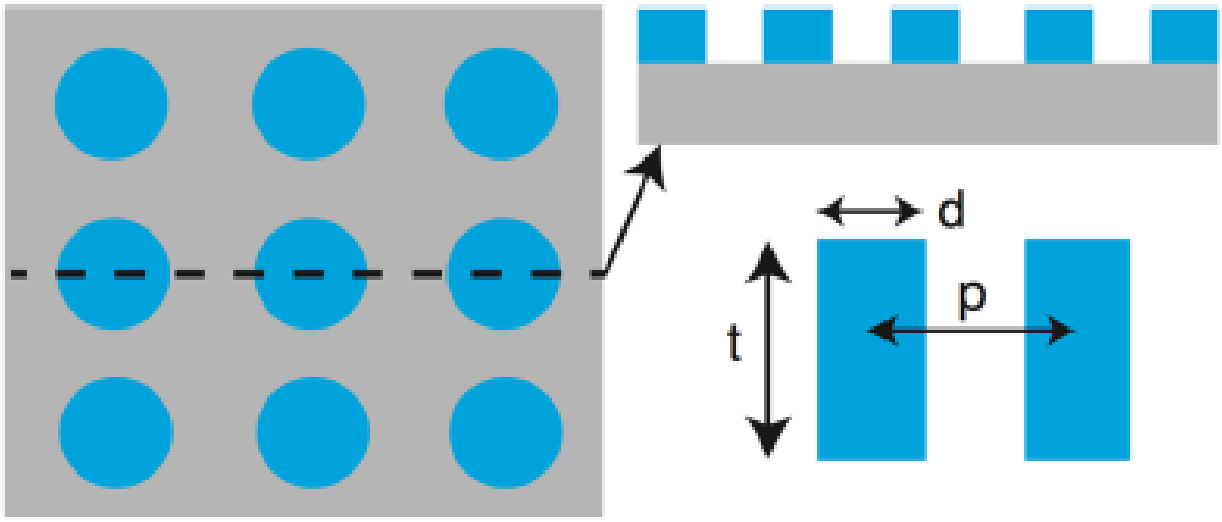

Figure 2.1: Typical unit cell showing the different views. The geometric parameters allowed to be changed are the thickness t, diameter d, and periodicity p.

properties of smoothly varying phase and high transmission amplitudes, but required high aspect ratios (t/d) that are difficult to reliably fabricate. Increasing the periodicity for a given thickness results in the appearance of more resonances where the phase and amplitude displayed sharp discontinuities. Increasing the thickness for a given periodicity results in sharper resonances that are easier to avoid, but this increases the aspect ratio of the pillars, and makes them harder to fabricate. These discontinuities make those specific ranges of duty cycles unattractive for high-performance metasurfaces, and when selecting parameters we ignored them.

On the basis of these simulations, we decided on a set of parameters $t = \lambda$ and $p = 0.7\lambda$ shown in Figure 2.2e to ensure a moderate aspect ratio for fabrication while maintaining full phase coverage and high transmission amplitudes. The parameters that displayed resonant behavior were removed during the parameter search.

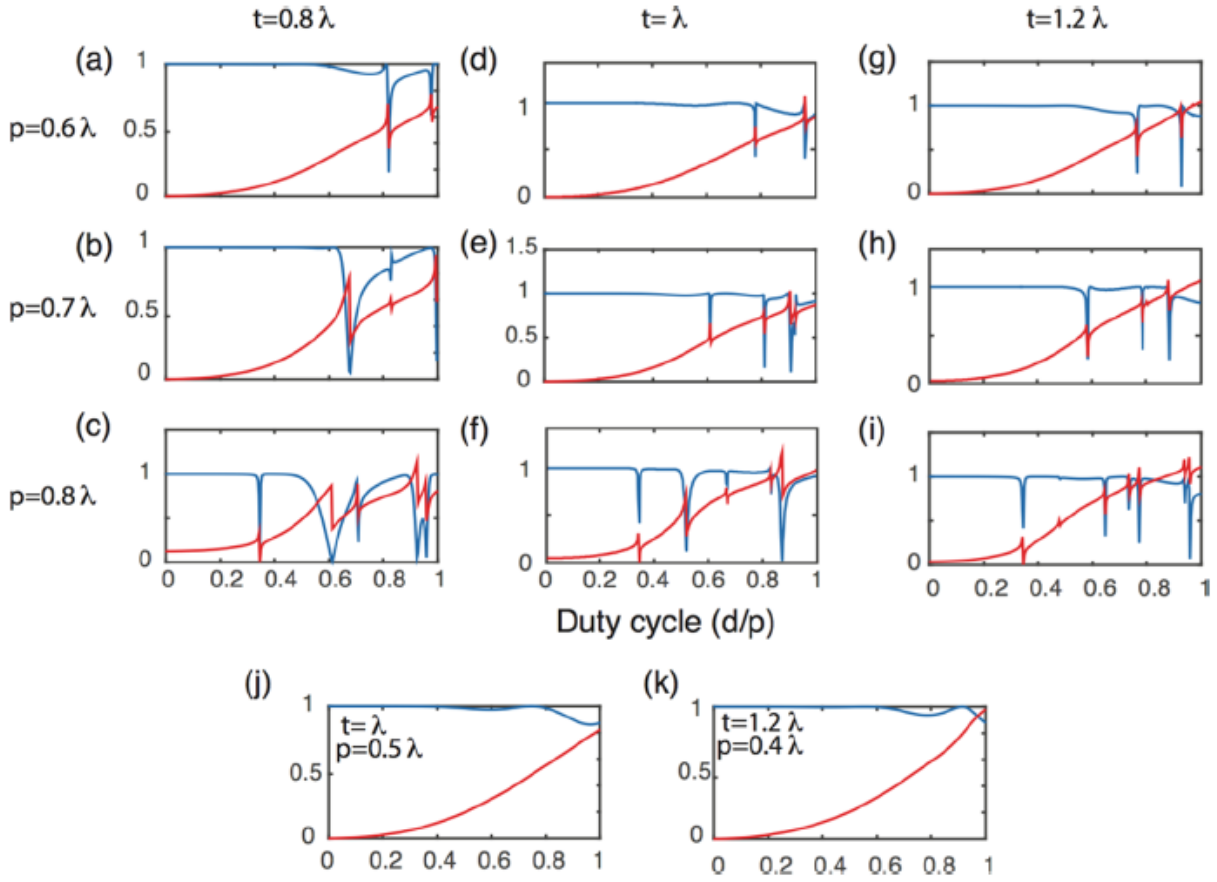

Figure 2.2: Amplitude and phase of the transmitted light through low-contrast metasurfaces with different duty cycles, periodicities, and thicknesses. Plotted are the phase delays (red) and transmission amplitudes (blue) associated with these gratings as a function of the duty cycles for varied periodicities and thicknesses. (a)-(i) represent parameters in the resonant regimes while (j) and (k) represent parameters in non-resonant regimes. In our paper, we decided to choose the parameters shown in (e).

2.3.3 Simulation

With the parameters in hand, we can now implement and simulate the phase profiles from equations (2.1) and (2.2) identified earlier. The parameter search gives us a lookup table that matches a specific phase to a specific pillar radius. By discretizing the phase profile onto a grid with our chosen periodicity, we can then choose a specific pillar radius that reproduces the desired phase. In our design we chose to further discretize the phase profile with six linear steps between 0 and 2π, corresponding to six different pillar diameters. In all of our devices, we ultimately chose a design wavelength of 633 nm, which corresponds to geometric parameters of $t = 633$ nm, $p = 443$ nm, and pillar diameters that vary between 192 to 440 nm.

We simulated multiple miniaturized metasurfaces using the FDTD method at their design operation wavelength 632 nm. As FDTD is a volume discretization method, its memory consumption scales quickly with increased device size. Due to this limitation, we were only able to simulate metasurfaces with diameters up to 30 μm, and focal lengths up to 40 μm. We characterized the effect of angular incidence on the lens performance in addition to the focal spot size and the focusing efficiency. As expected, for differing beam incidence angles, we found that increasing the angle of incidence resulted in a deflection of the focal spot in addition to decreasing the focusing efficiency as shown in Figure 2.3. The focal spot size and focusing efficiency were tested for varying numerical apertures (NA) and also for refractive indices of 2 and 3.5 corresponding to silicon nitride, and a fictional silicon-like material that is transparent in the visible. We found that for the specific parameters we chose, the focusing efficiency and spot size were not highly dependent on the refractive index. We can see from Figure 2.4 that both the high-index and low-index lenses fail to reach the diffraction-limited spot sizes for low focal lengths (high NA), but for longer focal lengths (low NA), they approach the diffraction limited value. The efficiencies plotted in figure 2.5 show that the efficiencies increase as the NA decreases, which is expected of the system, as high NA lenses must bend the light more obliquely and require faster phase variation to do so [22]. Both

the high-index and low-index lenses had similar performance for lower NA lenses, though the silicon like lens showed higher efficiencies for high-NA lenses. This was an encouraging result, as many other works had cited high refractive index as a central factor in the design and fabrication of high-performance metasurfaces [1, 22, 42].

2.3.4 Focal spot characterization

An important figure of merit to assess the quality of a lens is the spot size as it ultimately determines the resolution with which the lens can image. The smallest focal spot achievable by a perfect circular lens is defined by the first zero of the airy disk. This limit depends on both the geometry of the lens, and the wavelength of the light, and is given by:

$$\Delta x = 1.22\lambda \frac{f}{d}, \tag{2.10}$$

where Δx is the diffraction limited spot radius, λ is the wavelength of interest, f is the focal length of the lens, and d is the diameter of the lens. This limit depends only upon the incident wavelength and the geometric parameters of the lens, and is a valid approximation for lenses with focal lengths much larger than their diammeter. However, our low-focal-length lenses (50 and 100 μm) do not satisfy this requirement and require a different methodology for determining their focusing performance.

Instead we use a consistent criterion for characterizing the focusing performance of a lens with any combination of geometric parameters. An ideal lens with focal length f and radius a will produce in intensity profile given by the Airy disk:

$$I(\theta) = I_0 \left(\frac{2J_1(kasin\theta)}{kasin\theta} \right)^2, \tag{2.11}$$

where I_0 is the maximum intensity of the central peak, $J_1(x)$ is the first order Bessel function of the first kind, k is the free space wave vector of the incident light, a is the radius of the lens, and θ is the angular position as shown in figure 2.6a. We can then determine the diffraction-limited full-width at half-maximum (FWHM) for a lens with a focal length f and radius a by fitting the Airy disk using a Gaussian as shown in Figure 2.6b and c. We then

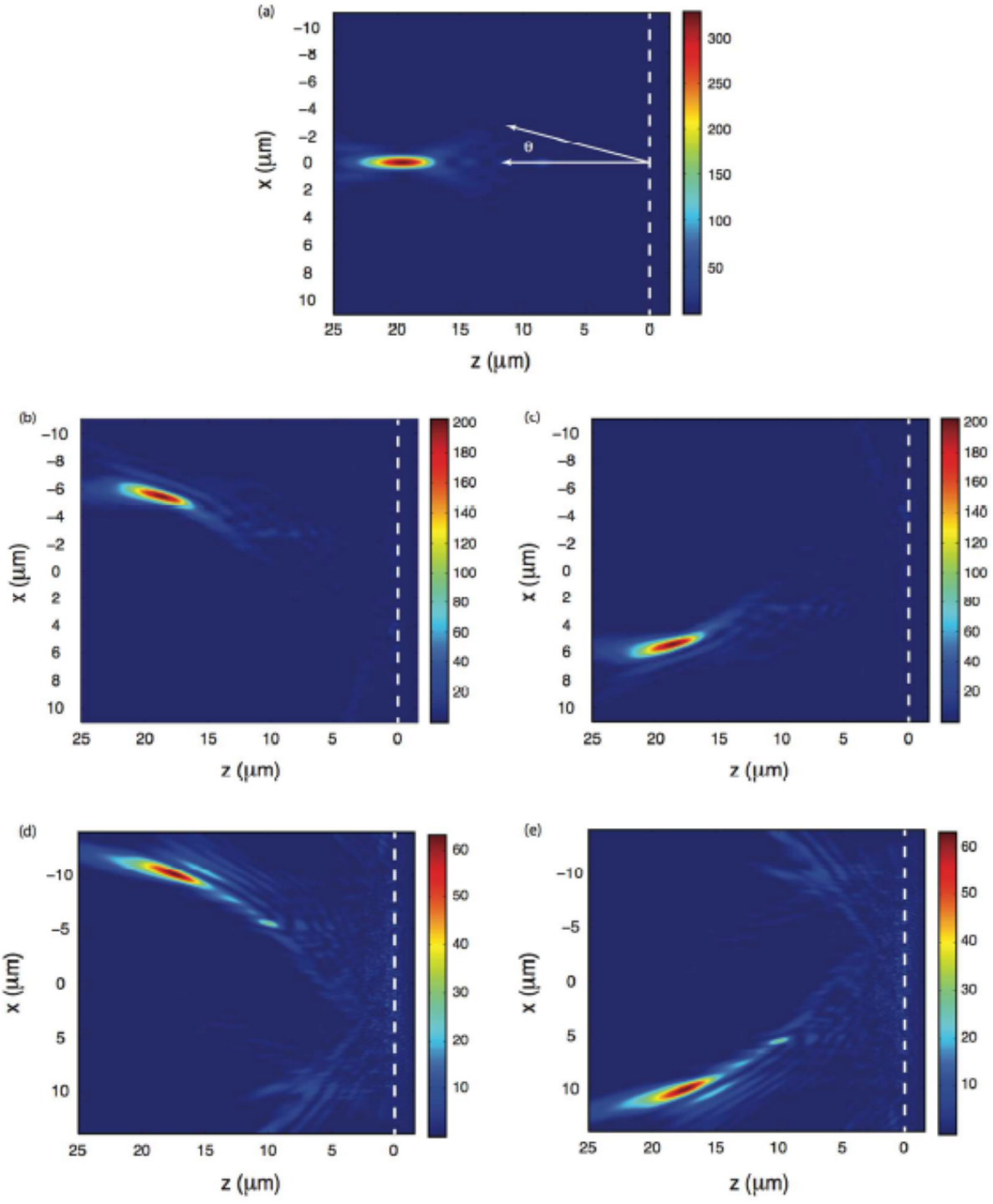

Figure 2.3: The response of a metasurface designed for focus at 20 μm with diameter 20 μm to both normally incident (a), and oblique incidences (b)-(e). Tested are 10 degree (b), (c), and 20 degree (d), (e) incidences.

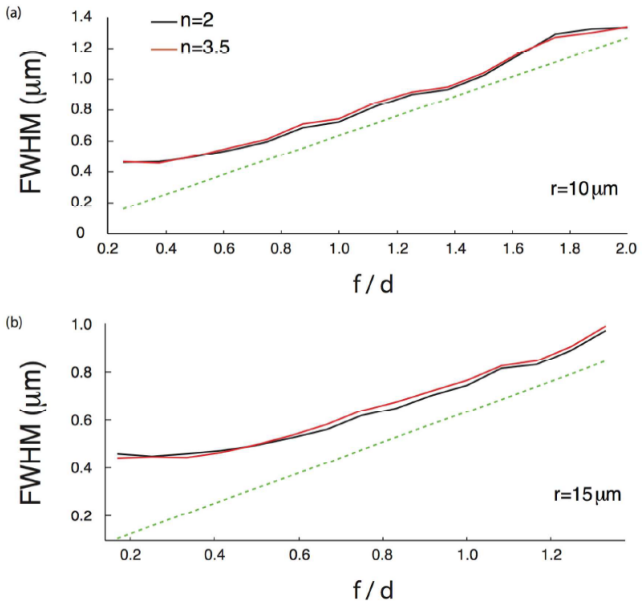

Figure 2.4: The spot sizes in FWHM plottted against the ratio of focal length to diameter. The red and black lines correspond to metasurfaces with indices of refraction $n = 2$ and $n = 3.5$ respectively. The dotted green line is the geometric diffraction limited spot size for an ideal lens. (a) and (b) show the dependence of the focal spots for a lens of diameter 20 μm and 30 μm respectively. The $n = 3.5$ set uses periodicity $p = 0.52\lambda$, with thickness $t = 0.61\lambda$, and pillar radii varying from 59 nm to 91 nm.

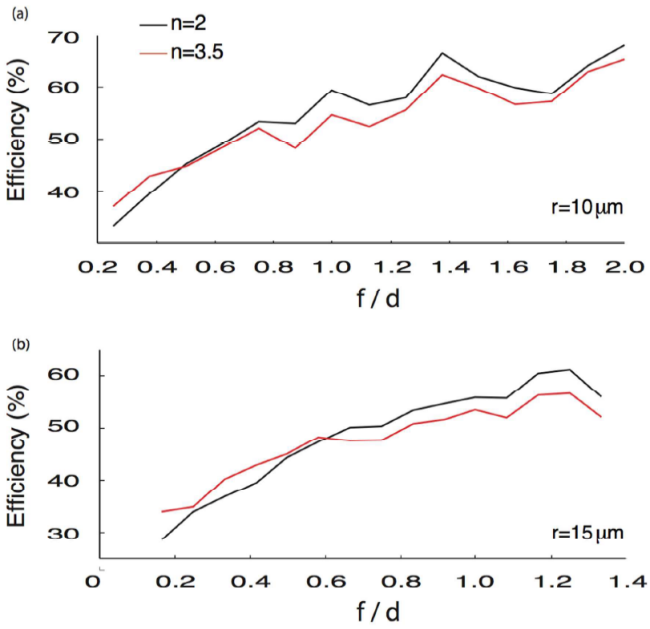

Figure 2.5: The focusing efficiencies plotted against the ratio of focal length to diameter. The red and black lines correspond to metasurfaces with indices of refraction $n = 2$ and $n = 3.5$ respectively. (a) and (b) show the dependence of the focal spots for a lens diameter of 20 μm and 30 μm respectively. Efficiencies are defined as in [1]. The $n = 3.5$ set uses periodicity $p = 0.52\lambda$, with thickness $t = 0.61\lambda$, and pillar radii varying from 59 nm to 91 nm.

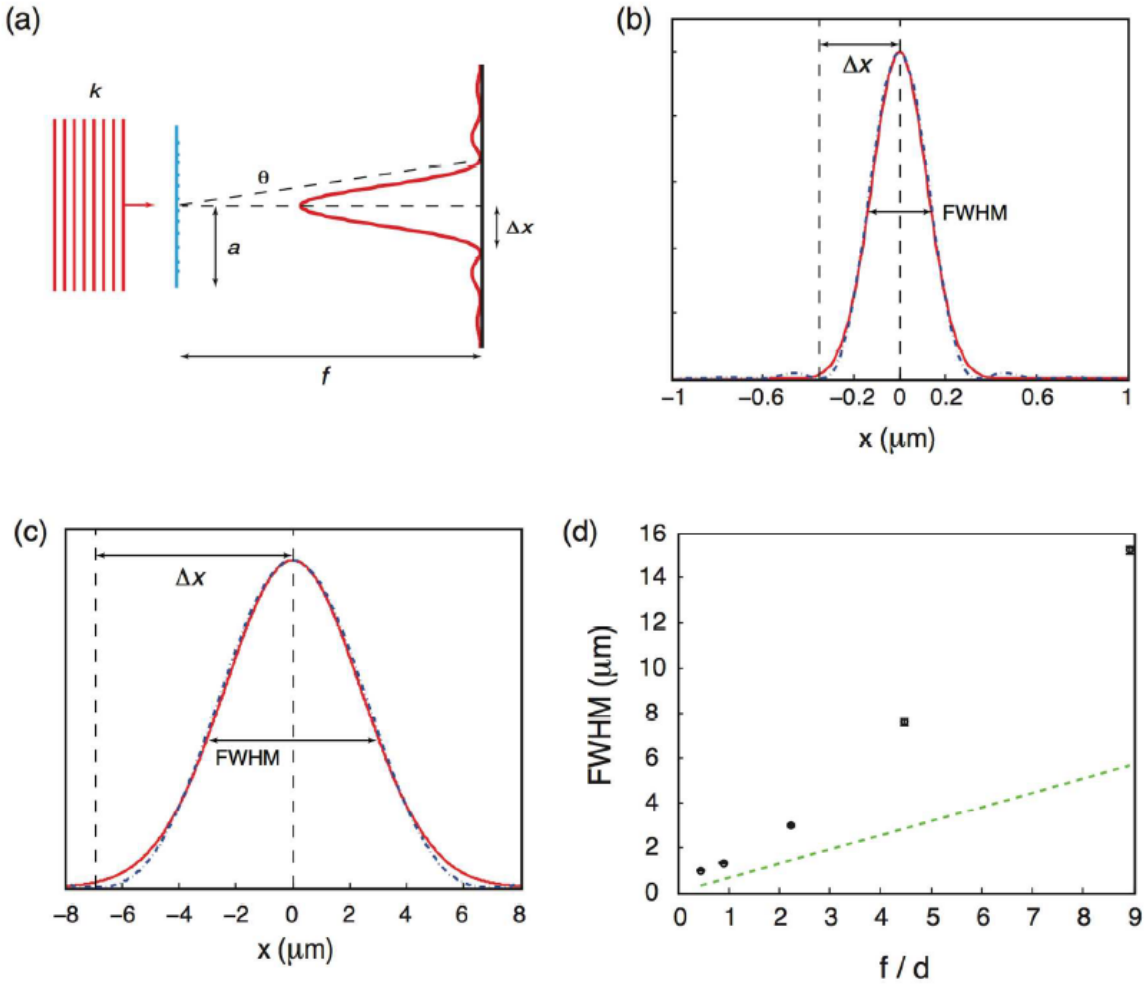

Figure 2.6: Fitting of an Airy disk with a Gaussian. (a) Schematic of the setup used for the calculation of the Airy disk profile. Examples of an Airy disk which represents the intensity profile of an ideal (b) 50 μm and (c) 1 mm lens. (d) is experimental data from a 250 μm metasurface lens showing showing deviation from the diffraction limit plotted in dashed green.

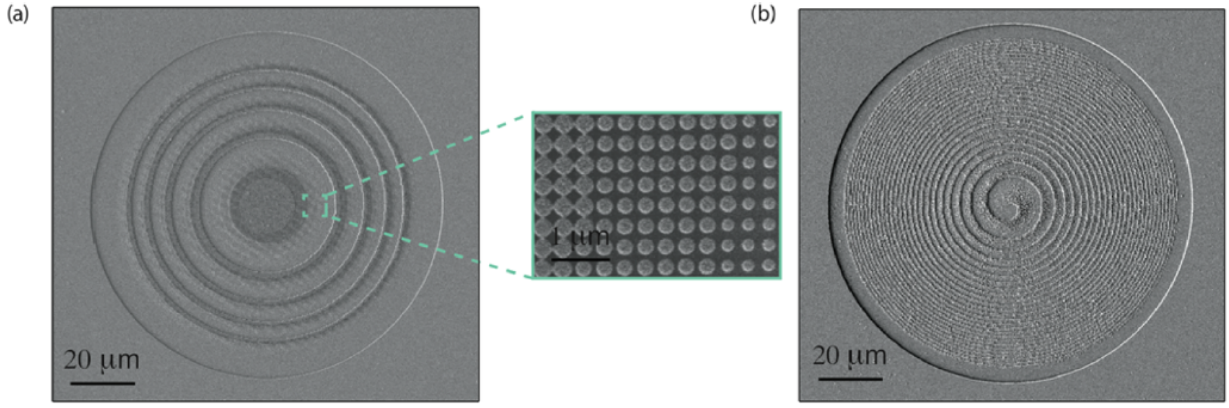

Figure 2.7: SEMs of (a) a 250 μm focal length lens with radius 56 μm, and (b) a vortex beam generator with $l = 2$, a 100 μm focal length, and radius 60 μm. Both are shown with the aluminum hard mask intact after completing a fluorine etch.

compare our experimentally measured FWHM against that of a perfect lens with the same geometric parameters as shown in Figure 2.6d.

2.4 Fabrication

We chose to fabricate a set of five lenses with focal lengths 50, 100, 250, 500, and 1000 μm all with diameter 112 μm, and a set of two vortex beam generators with $l = 1, 2$, focal length 100 μm, and diameter 120 μm. As our feature sizes are as small as 192 nm and below the diffraction limit of conventional and commonly available photolithography systems, we used electron beam lithography (EBL) to define our patterns. We note however that deep UV lithopgrahy is capable of producing these feature sizes. Two scanning electron micrographs (SEM)s of fabricated devices are shown in Figure 2.7 where (a) shows a lens with a focal length of 250 μm and (b) is a vortex lens with $l = 2$ and a focal length of 100 μm. All fabrication of the samples was performed at the WNF. The fabrication procedure is outlined in Appendix A.1.

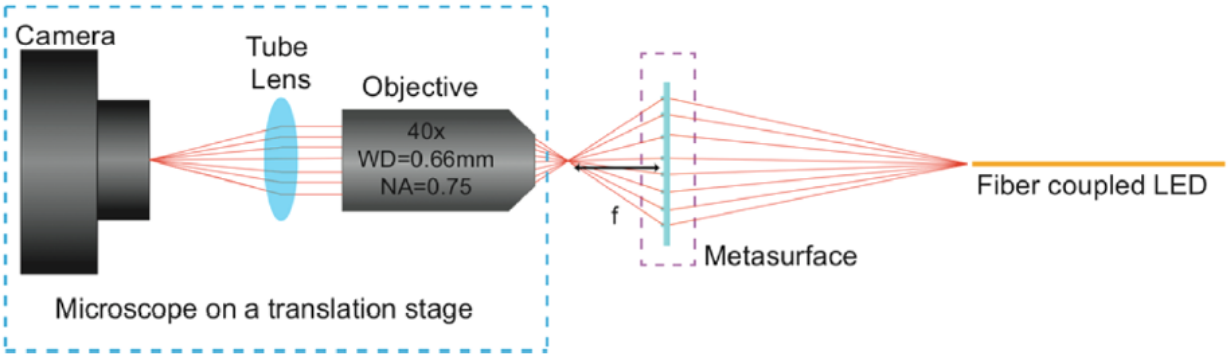

Figure 2.8: Translatable microscope used to measure intensity profiles of the metasurface lenses and vortex beams

2.5 Experimental Results

We tested the lenses and vortex beam generators with a homebuilt microscope consisting of a Nikon Plan Fluor 40x objective, a Thorlabs TTL-200 tube lens, and a Point Grey Chameleon camera. The specific setup is shown in figure 2.8 where our excitation source was a set of three LEDs centered around red (Thorlabs M625 F1, 625 nm), green (Thorlabs M530F1, 540 nm) and blue (Thorlabs M455F1, 455 nm). By translating the microscope and camera along the optical axis, we can move into and out of the focal plane and image the x-y plane intensity profile at varying z distances. This allows us to accurately characterize the optical elements as they focus and defocus. During characterization we can clearly see the beam radius change as we translate through the focus of the 250 μm focal length lens and the FWHM values obtained by a Gaussian fit are plotted in Figure 2.9a. Based on the intensity profile at the focal point in Figure 2.9b, we can clearly see the lens focusing at the design focal length. An example of the Gaussian fits used to characterize the intensity profiles are shown in Figure 2.9c.

We tested all five different focal length lenses with focal lengths of 50, 100, 250, 500, and 1000 μm, all with radus 56 μm. The measured FWHM of the focal spot sizes for all of the

lenses are plotted against the ratio of the focal length (f) to diameter (d) in Figure 2.10, where the dotted green line represents the FWHM of a diffraction-limited spot of a lens with the given geometric parameters. The deviation from the diffraction limit is attributed mostly to fabrication imperfectiions. In particular, we note that the 50 μm lens achieves a FWHM less than 1 μm and is close to diffraction-limited. The measurement of the focal lengths of these lenses also agrees well with our design parameters.

Another important figure of merit for a lens is the focusing efficiency. To measure this, we inserted a flip mirror before the camera to direct the beam to a power meter (Newport 1918-R). We then measure the incident power to the focus by using a pinhole in a confocal microscope to isolate a spot with radius 3 times the FWHM. The focusing efficiency was taken to be the ratio of the power incident into the focus to the power incident on the entire lens. The transmission efficiency was taken to be the ratio of the power incident on the detector through the lens to the power incident through the glass substrate. Both the transmission and focusing efficiencies increase as the ratio f/d increases as shown in Figure 2.10b. The focusing efficiency rises to a maximum of 40% for the 1 mm lens, and the transmission effiency rises to near 90% for the 500 μm lens. However, the high-NA metasurfaces generally had comparably lower transmission and focusing efficiencies. However, these transmission efficiencies are significantly higher than other metasurfaces in the visible frequency range. The focusing efficiencies are lower than we would have expected based on our initial simulations. We attribute this error largely to the fabrication error of our pillars as the final devices showed overetching of around 50 nm, which affects the produced phase profile.

We then investigated the chromatic behavior of the lens for red, green, and blue light. The wavelength dependence of the 250 μm focal length lens is shown in Figure 2.10c. The focal distances of the lens increases with decreasing wavelength, showing the characteristic diffractive optic chromatic aberration. The focal length increases from 0.26 mm at 625 nm to 0.35 mm at 455 nm. We also observe an increase in the size of the focal spot with decreasing wavelength, from a minimum of 3 μm at 625 nm to a maximum of 4 μm at 455 nm. We remark that the product of the experimentally measured focal length (f) and illumination

wavelength (λ) is roughly constant for our design as expected for diffractive optics.

Lastly, we characterized the fabricated focusing vortex beam generators, and imaged their intensity profiles as shown in Figures 2.11a-d. They were all fabricated for a design wavelength of 633 nm with focal lengths of 100 μm and radii of 60 μm. One plate was fabricated for angular momentum state $l = 1$ and the other for $l = 2$. The measured intensity profiles were taken with the same setup as the lenses using the 625 nm LED. The spiral intensiity profiles were taken at a point off the focal plane, and as expected, the $l = 1$ plate produced only one curl while the $l = 2$ plate produced two curls. Both spirals also wind along the same direction indicating that they are of the same parity. In order to image the characteristic donut profile, we translated the microscope into the focal plane of the vortex beam generators. Comparing the donut profiles, the higher angular momentum beam has a larger donut radius, which is consistent with the behavior of the higher order vortex beams. The efficiencies of the vortex beam generators are measured using the same confocal setup, but instead of isolating a spot size 3 times the FWHM, the pinhole is adjusted to isolate just the donut beam. For the focusing efficiency, we isolate the power concentrated into the donut field intensity profile at the focal plane using a pinhole. Both of the devices show transmission efficiencies of up to 80% and focusing efficiencies of up to 10%. These devices show higher transmission efficiencies and lower focusing efficiencies than that of a metasurface lens fabricated with a 100 μm focal length shown in Figure 2.10b, which had transmsission and focusing efficiencies of around 40% and 20% respectively. We attribute this to the fabrication of the vortex beam generator, as its phase profile results in a higher pillar radius gradient that is more difficult to realize in fabrication. In our case, this resulted in the overexposure and ultimately overetching of the pillars. We posit that the overetching would allow more incoming light to pass through undiffracted, increasing the transmission efficiency. However, this also decreases the focusing efficiency as less of the light is diffracted towards the donut profile.

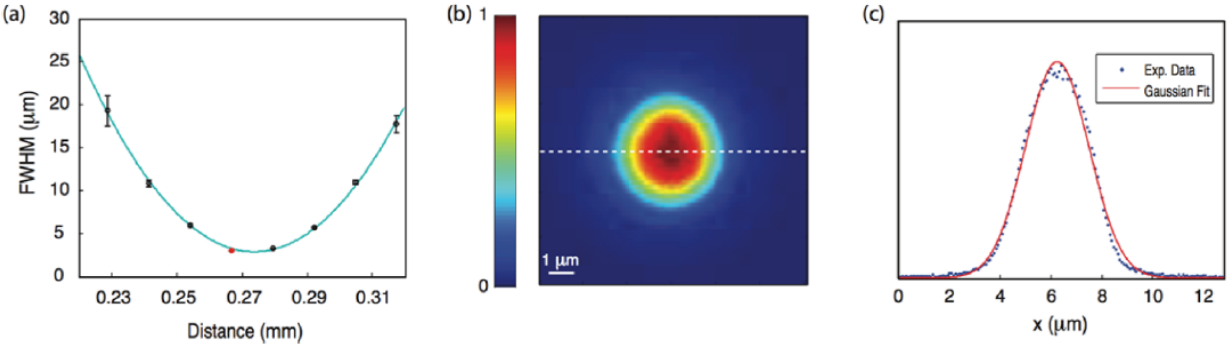

Figure 2.9: Characterization of a 250μm focal length lens with an LED centered at 625 nm. In (a) the FWHM is plotted as a function of the distance translated along the z direction. The error bars denote the 95% confidence interval for the Gaussian fits. The blue curve serves as an eye guide. (b) is a 2D intensity profile at the focal plane, the red dot in (a). (c) is a Gaussian funtion fit to the cross-section data taken at the dashed line in (b). The FWHM of the fit is extracted to estimate the beam size.

2.6 Conclusion

In this chapter, we demonstrated the suitability of silicon nitride for implementing both metasurface lenses and vortex beam generators. The use of low contrast materials such as silicon nitride extend the range of materials available for metasurface optics into those that are transparent at visible wavelengths. By using silicon nitride as our material, we can also leverage its compatibility with existing CMOS foundries for scalable fabrication. The wavelength-scale thickness and planar geometry of these optical elements allows the miniaturization of optical elements for integration onto optical fibers and other small-scale optical systems. In addition, the approach greating simplifes the design and fabrication process of complicated aspherical optical elements.

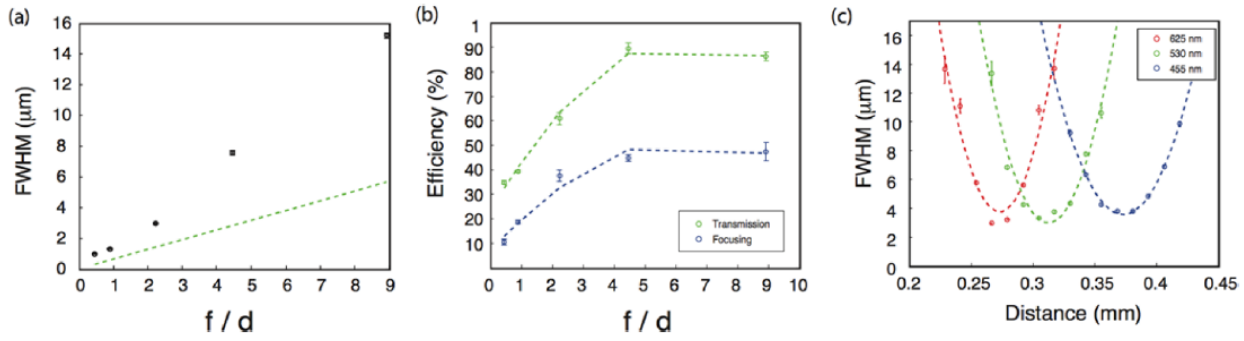

Figure 2.10: Performance of the metasurface lenses with different focal lengths plotted as a function of their focal length to diameter ratio f/d. (a) is the measured focal spot sizes for the fabricated lenses, and the dotted green line shows the diffraction-limited fwhm. (b) Shows the measured transmission and focusing efficiencies for all fabricated lenses. error bars are obtained from the standard deviation of three measurements on each device. (c) shows the chromatic dispersion of the 250 μm device. The red, green, and blue curves correspond to illumination with 625, 530, and 455 nm LEDs, respectively. Plotted curves are a guide to the eye, and error bars represent 95% confidence intervals for the Gaussian fits.

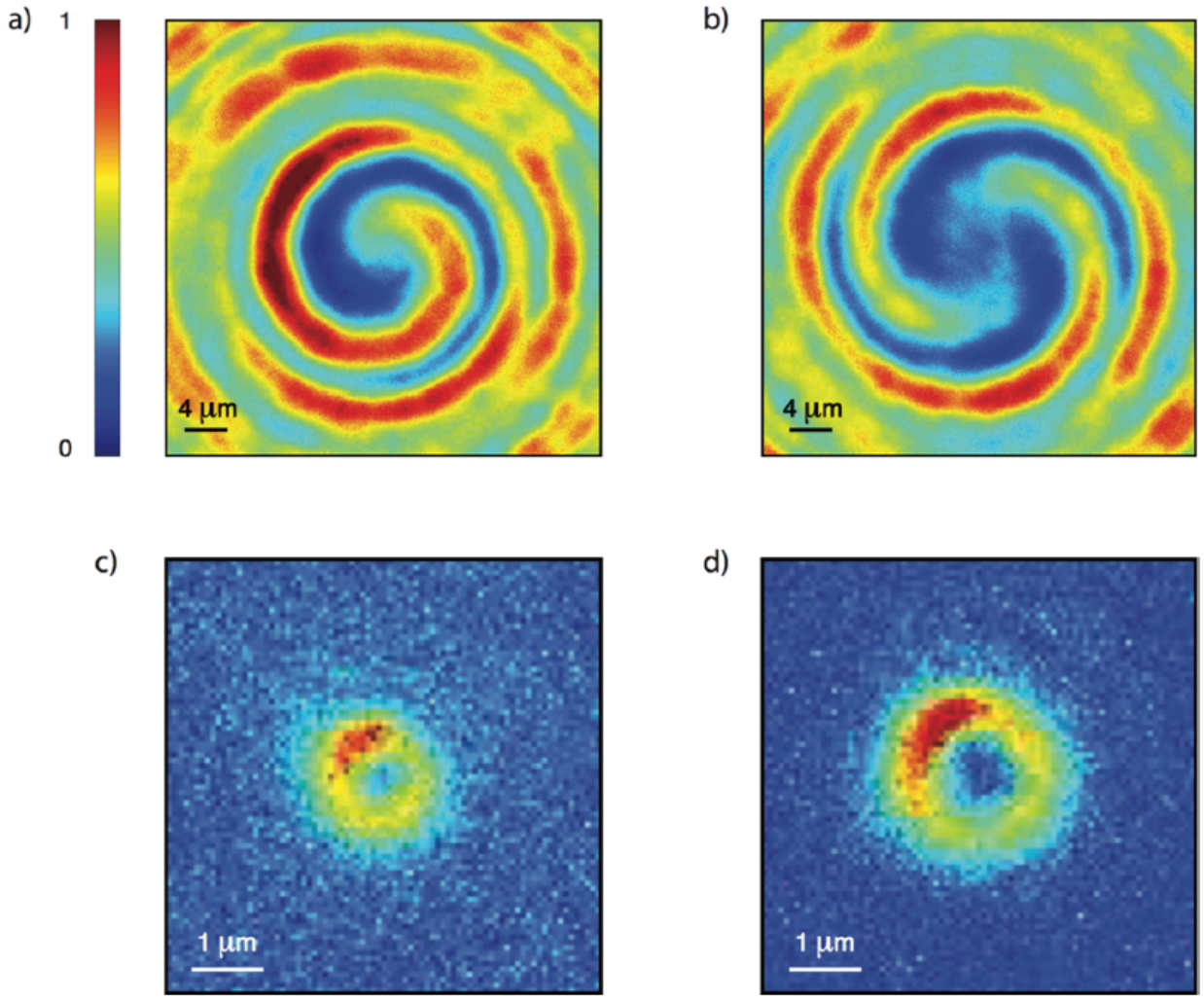

Figure 2.11: Focusing vortex beam generator field profiles. The intensity profiles are normalized to their maximums. Plotted are the (a) helical wavefront with one curl and (c) the characteristic donut distribution for the $l = 1$ vortex plate. (b) and (d) are the helical wavefront with two curls, and the bigger donut profile respectively, corresponding to the $l = 2$ plate. All figures share the same colorbar. (c) and (d) are taken at the focal plane (100 µm) of the focusing vortex beam generator.

Chapter 3

FREEFORM SILICON NITRIDE METASURFACES

In the previous section, we discussed the design, fabrication, and characterization of silicon nitride-based metasurface lenses and vortex beam generators. In those cases, the forward design technique allowed us to design lenses with different NAs at the same thickness. Metasurface optics can miniaturize lenses, but due to their rotational symmetry, lenses are easily fabricated using traditional methods such as diamond turning and polishing. In the case of freeform optics, metasurfaces can offer a pathway to both miniaturization and scalable fabrication.

In this chapter, we will present work in the adaptation of freeform optics to a metasurface platform. First we will discuss the motivation for freeform optics based on a cubic phase function. Then we present a procedure for converting a sag profile to a metasurface with simulation results of the cubic-phase plate and Alvarez lens. We characterize the simulation results characterizing the performance of a scaled down version of the Alvarez lens. Finally, we show experimental results for the cubic and Alvarez phase plates. We show the suitability of a cubic function for mitigating the known chromatic aberrations associated with a diffractive optical element, and also a large tunable-power Alvarez lens. In particular, our demonstration of cubic phase plate shows an extended depth of field of over 300 μm, and the Alvarez lens shows a change in optical power of 1600 diopters with only 100 μm of physical displacement. This chapter consists of work that was included in and the basis of Ref. [47].

3.1 Motivation

The function of an optical element is instrically tied to the geometry of its surface. The ease of manufacturing has often constrained mass produced optical elements to have rotational

invariance. The emerging field of freeform optics leverages more complex curvatures to enable novel functionalities and simplified optical systems [65]. These freeform geometries have been shown to be useful for correcting aberrations [66], off-axis [67] and on-axis [68] imaging, expanding field of view [68] and increasing depth of field [69]. Recent interest in this field has been driven by potential applications in near-eye displays as well as compact optical systems for medical, aerospace, and mobile devices where stringent restrictions exist limiting the form factor of the optical package. The surfaces we will concentrate on are based on the cubic profile, where the surface of the optical element is defined by a cubic function. These elements have been known to exhibit extended depth of focus [69], and in tandem they form a compound optical element with adjustable power called the Alvarez lens [70–73]. The extended depth of focus can be used to mitigate the intrinsic diffractive chromatic aberrations

Unlike conventional optics, metasurface optics design is curvature agnostic, and readily accepts both conventional spherical curvatures as well as complex freeform surfaces with no additional design difficulties. Moreover, well-developed semiconductor nanofabrication technology can be readily employed to fabricate these wavelength-scale thickness devices. In this work we demonstrate that freeform surfaces are an excellent candidate for adaptation using metasurfaces. This compatibility allows us to demonstrate a high-performance wavefront coded device and highly tunable optical systems.

3.2 Freeform Phase Profiles

An arbitrary freeform element is some phase profile $\phi(x, y)$, but generally, the element is specified as a height map $z(x, y)$, also known as the sag profile. This map describes the curvature of the optical element and is readily converted into a phase profile for a specific illuminating wavelength λ as:

$$\phi(x, y) = \frac{2\pi n}{\lambda} z(x, y), \tag{3.1}$$

where n is the refractive index of the optic. To do numerical simulations with this idealized phase plate model, we can use the angular spectrum propagation method described in Section

(2.2). In general, $z(x, y)$ is some smooth function, meaning $\phi(x, y)$ will also be a smooth function. In order to map this phase profile onto a metasurface, we discretize it in terms of the grating periodicity we use for the metasurface, and choose six phase values linearly spaced between 0 and 2π.

3.2.1 Cubic-phase plate

Cubic-phase elements have been used in the context of wave-front coding as part of an extended depth of focus system [69]. Systems exhibiting depth of focus are characterized by a point spread function (PSF) that is independent of varying degrees of defocus for an extended length along the optical axis. This means that for a range of displacements along the optical axis, the optical element produces the same or a similar intensity pattern. A PSF is a characterization of an optical system's response to a point source and characterizes its imperfections. The PSF of a lens for example, changes drastically as it is defocused, however the PSF of a cubic-phase plate does not. These systems can be characterized by a phase function:

$$\phi_{cubic}(x, y) = \frac{A_{cubic}}{L^3}\left(x^3 + y^3\right), \tag{3.2}$$

where x and y are spatial coordinates, L is the size of the device, and A_{cubic} is a constant characterizing the strength of the cubic-phase plate. Higher values of A_{cubic} result in larger regions where the PSF remains constant, at the cost of lower image quality [69]. For our experiments we choose a value of $A_{cubic} = 14\pi$, and $L = 150\mu m$.

3.2.2 Alvarez lens

The Alvarez lens is a compound optical element consisting of two cubic phase plates, with one obeying the phase profile:

$$\phi_{alv}(x, y) = \frac{2\pi}{\lambda} A_{alv}\left(\frac{1}{3}x^3 + xy^2\right) \tag{3.3}$$

and the other obeying its inverse such that $\phi_{alv}(x, y) + \phi_{inv}(x, y) = 0$. λ is the operating wavelength of the device and A_{alv} is a constant that determines the power and tuning range

of the Alvarez lens. If the two elements are perfectly aligned, the Alvarez lens does not focus light and can be interpreted to have an infinite focal length or zero optical power. Laterally displacing the elements relative to each other along the x-axis allows us to focus at finite distances. Morever, by controlling the lateral displacement along the x-axis we can change the focal length continuously. Large values of A_{alv} increase the range of tunable focal lengths at the expense of image quality. For our Alvarez design, we chose a value of $A_{alv} = 1.17 \times 10^7$ m^{-2}, with an square aperture of side length 150 μm.

By adding the two phase profiles together with some finite displacement d, we can see how the focal length depends on lateral displacement along the x-axis. First we begin with the sum of the two plates where one is displaced along the positive direction and another along the negative direction:

$$\phi_{total}(x, y) = \phi_{alv}(x + d, y) + \phi_{inv}(x - d, y), \tag{3.4}$$

which is explicitly:

$$\phi_{total}(x, y) = \frac{2\pi}{\lambda} A_{alv} \left[\frac{1}{3}(x + d)^3 + (x + d)y^2 - \frac{1}{3}(x - d)^3 - (x - d)y^2 \right]. \tag{3.5}$$

Adding these two functions together, we obtain:

$$\phi_{total}(x, y) = \frac{2\pi}{\lambda} A_{alv} \left[2d(x^2 + y^2) + \frac{2}{3}d^3 \right]. \tag{3.6}$$

Finally, neglecting the overall phase in equation (3.6) and identifying the first term as a spherical lens, we can define the focal length f of the device with respect to displacement as the expression:

$$f(d) = \frac{1}{4A_{alv}d}, \tag{3.7}$$

or alternatively the optical power P defined as:

$$P(d) = \frac{1}{f(d)} = 4A_{alv}d, \tag{3.8}$$

where we can conveniently see that the change in optical power has a linear dependence on the displacement along the x-axis. The theoretical focal length ranges are illustrated in

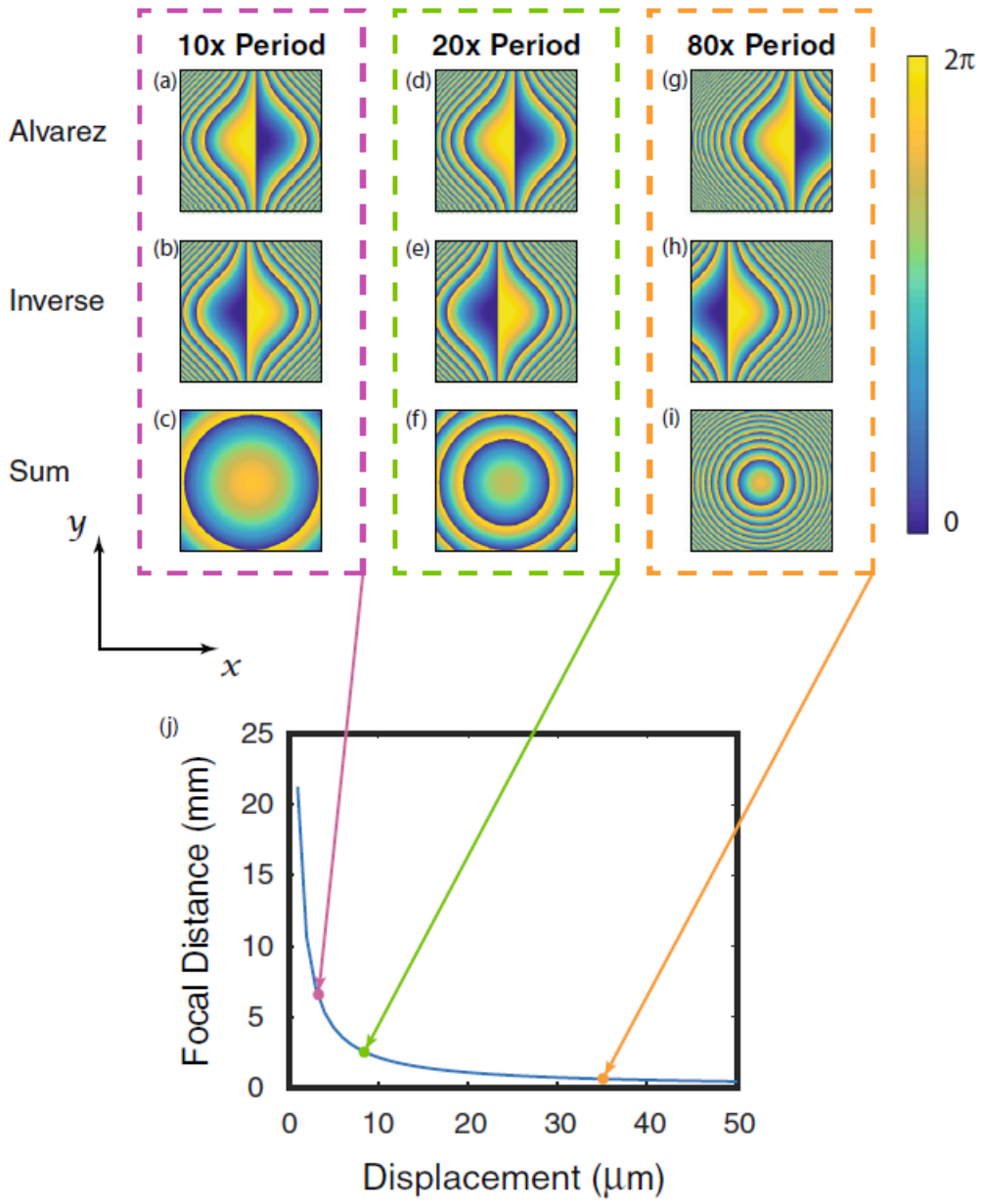

Figure 3.1: Example of how the Alvarez lens phase profile changes for three given displacements of 10x (a)-(c), 20x (d)-(f), and 80x (g)-(i) the metasurface sampling periodicity. The figure shows how the displacment of the two phase plates gives rise to a converging spherical lens in the limit of zero phase plate separation. For large separation we see a short focal length lens, and for small displacements we see a long focal length lens. (j) shows a continuous plot of equation (3.7) showing the total tunable focal length range

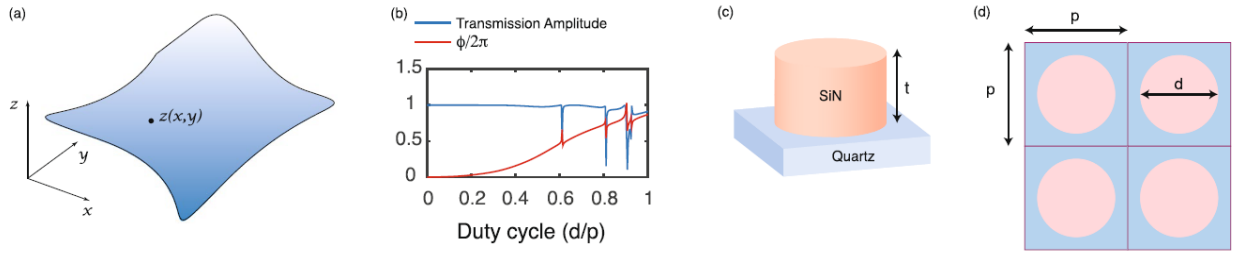

Figure 3.2: Phase profile conversion process beginning with (a) some arbitrary sag profile $z(x, y)$, converted into a radius map using parameters shown in (b) where red is transmission amplitude, and blue is noramlized phase. (c) and (d) a side and top-down view of the simulated unit cell with a silicon nitride pillar on a quartz substrate defining the thickness t, diameter d, and periodicity p.

3.1 where the effect of displacements on the total phase profile is explicitly shown for three displacements corresponding to 10x, 20x, and 80x the metasurface periodicity of 443 nm.

Importantly, this tunable-power element displaces perpindicular to the optical axis rather than parallel to it. While it is simple to create a tunable focus system by displacing two lens along their shared optical axis, this approach requires extra space along the optical axis that is often unavailable.

3.3 Simulation

As in the previous section, we first simulated scaled-down versions of the final devices in Lumerical FDTD to confirm their operation. To do this, we followed a similar procedure to convert the phase profiles from equations (3.2) and (3.3) into maps of dielectric pillars. We also used the same set of geometric parameters, which were cylindrical pillars of thickness $t = 632$ nm on a square lattice with periodicity $p = 0.7\lambda = 443$ nm. These parameters are reiterated in Figure 3.2c

We first simulate a miniaturized version of the design Alvarez lens with $A_{alv} = 6.67 \times 10^9$ m^{-2} with each plate having total length 10 μm to test the if the cascaded metasurfaces would

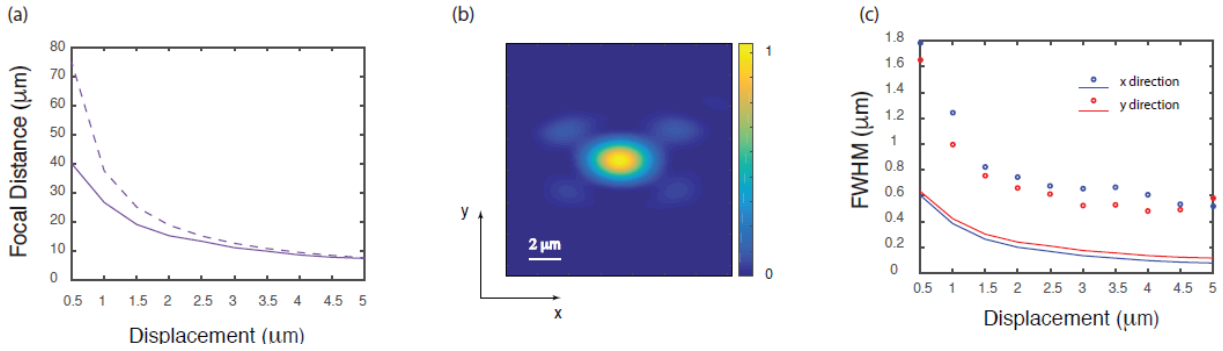

Figure 3.3: Simulated results of a miniaturized Alvarez lens pair with $A_{alv} = 6.67 \times 10^9$ m^{-2} using FDTD. (a) shows the simulated (solid) vs theoretical (dashed) focal lengths achieved, (b) is an example of a focal spot at a displacement of 0.5 μm, and (c) the simulated FWHM (dots) and theoretical FWHM of a diffraction limited spot (line) along the x and y directions. The x direction diffraction limited FWHM is larger because the lens increases in size as the two plates are displaced.

perform the function of an Alvarez lens. The A_{alv} value is increased from our design value for an actual device so we can resolve the changes in focal lengths with a small FDTD simulation region. The initial results are shown in Figure 3.3 showing the focal length ranges, a focal spot size, and the spot size. These plates are separated by a distance of 1.5 μm for the simulations where separation is kept constant.

We then simulate the response of this miniaturized system to different incident wavelengths, and different axial separations between the two metasurface plates. Chromatic aberrations are ubiquitous to metasurface optics, and we would like to characterize how the Alvarez lenses are affected as there are two different plates to account for. In addition, in any physical system, the Alvarez plates must be separated by some physical distance to mitigate the possibility of damage to the metasurface plates.

We test the response of the Alvarez lens to seven different wavelengths in the visible range between 400 nm and 700 nm in Figures 3.4 and 3.5. We see that the lens displays strong

chromatic aberrations as expected for diffractive optics, and only forms a distinct focal spot for wavelengths of 550 nm and above. We can see that for wavelengths lower than 550 nm there are extended focal spots in the x-z plane and the device fails to form distinct focal spots. However, along the y-z plane we see the standard chromatic aberration associated with diffractive optics. We then test the response of the system to different separations as shown in Figure 3.6. In simulation the axial separation has a large effect on the focal spot along both the x-z and y-z planes. For separations that are large enough in Figure 3.6c and d, we can see that the beam produced by the first plate clips the edge of the second plate causing decreases in focal spot intensity in addition to an aberrated focal spot in the $x - z$ plane. This is due to the displacement of the plates along the x direction while along the y direction, the lens shape remains the same.

3.4 Fabrication

We fabricated the metasurfaces using the same fabrication flow as that described in Chapter 2, and is presented in Appendix A.1. Scanning electron micrographs (SEM) of the fabrication results for one of the plates constituting an Alvarez lens and the cubic-phase plate are shown in Figures 3.7a and b respectively. The fabrication in this work has improved significantly compared to that of previous attempts. However, there is still some overetching of the pillars that results in smaller pillar diameters than the design.

3.5 Experimental Results

We tested the Alvarez lens and the cubic-phase plates with homebuilt microscopes consisting of a Nikon Plan Fluor 40x objective, a Thorlabs TTL-200 tube lens, and a Point Grey Chameleon, with a setup analogous to that of Section (2.5).

3.5.1 Cubic-phase plate

For the cubic-phase plate, we our experiment is primarily interested in capturing the point spread function (PSF) of the cubic element for different values of defocus. The device

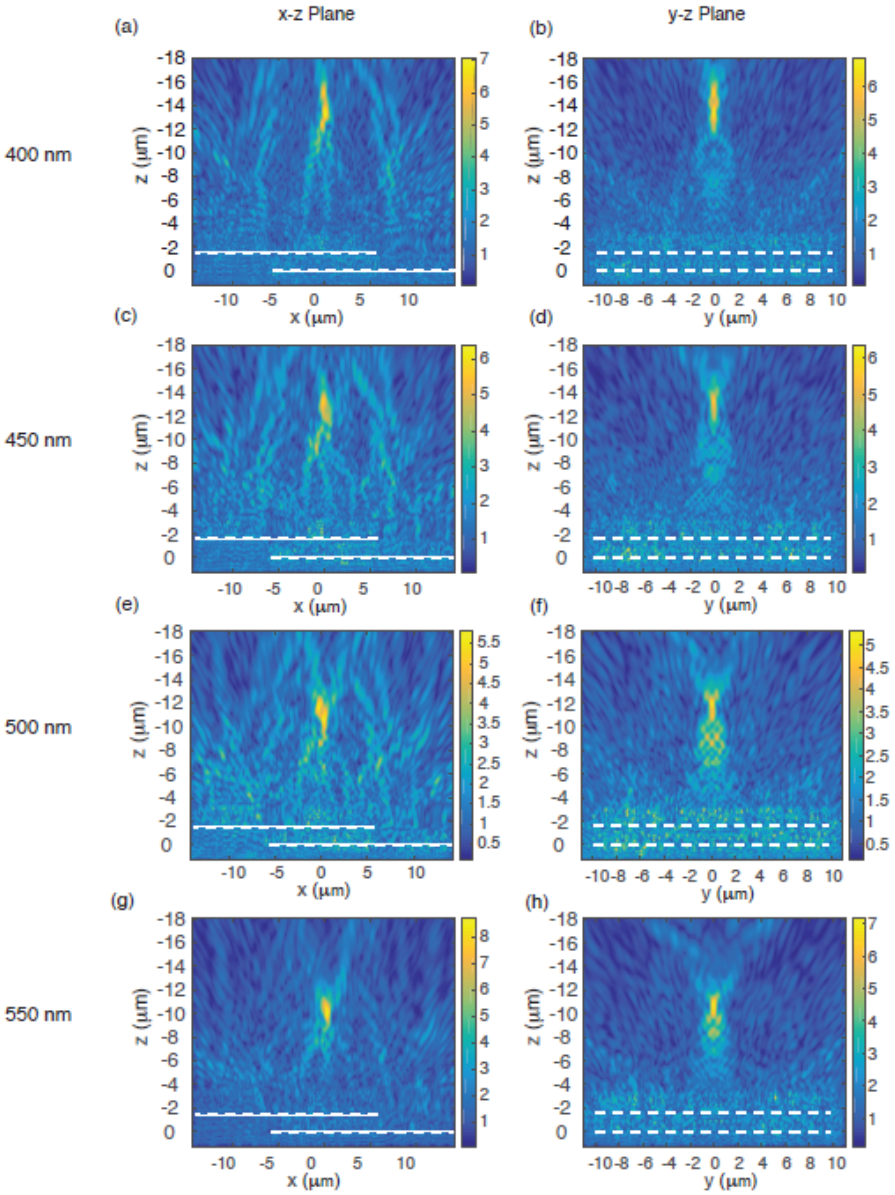

Figure 3.4: Behavior of the Alvarez lens under chromatic illumination. Plotted are the electric field intensity profiles on the x-z and y-z planes centered along the optical axis for illumination wavelengths covering the visible spectrum ($400 - 550$ nm) in steps of 50 nm. The lens begins to form a distinct focal spot for 550 nm in both the x-z and y-z planes. The white dashed lines indicate the locations of the two metasurfaces comprising the Alvarez lens.

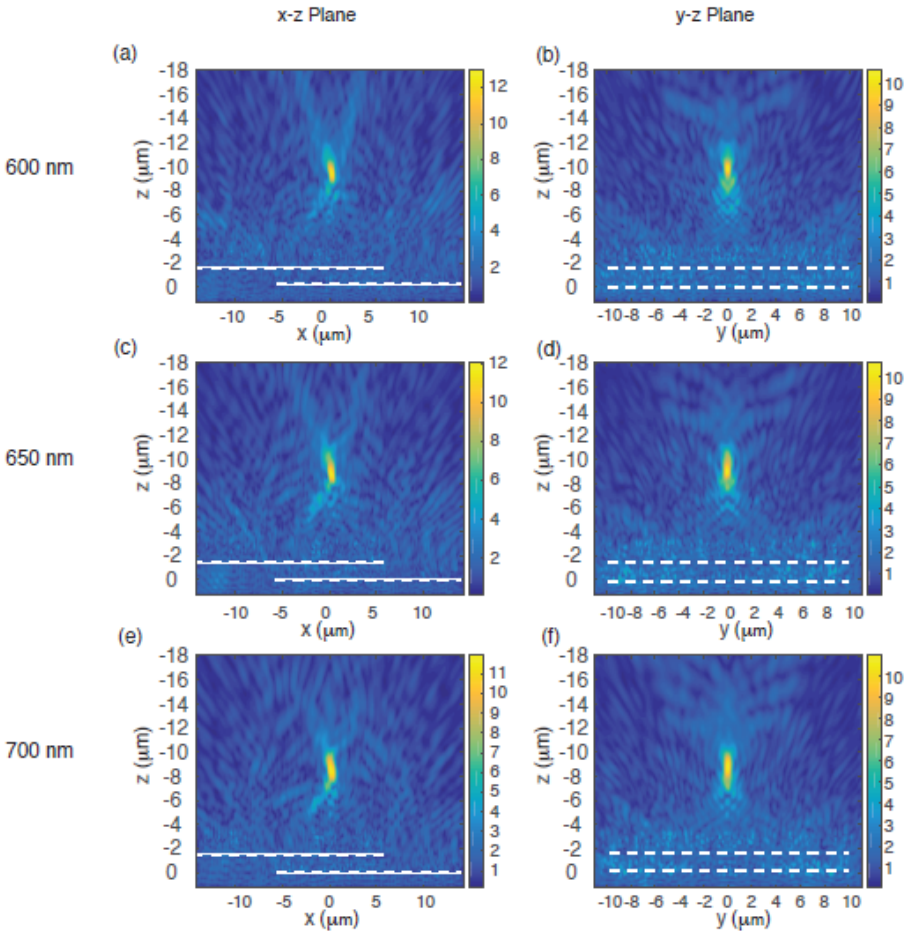

Figure 3.5: Behavior of the Alvarez lens under chromatic illumination. Plotted are the electric field intensity profiles on the x-z and y-z planes centered along the optical axis for illumination wavelengths covering the visible spectrum ($600 - 700$ nm) in steps of 50 nm.

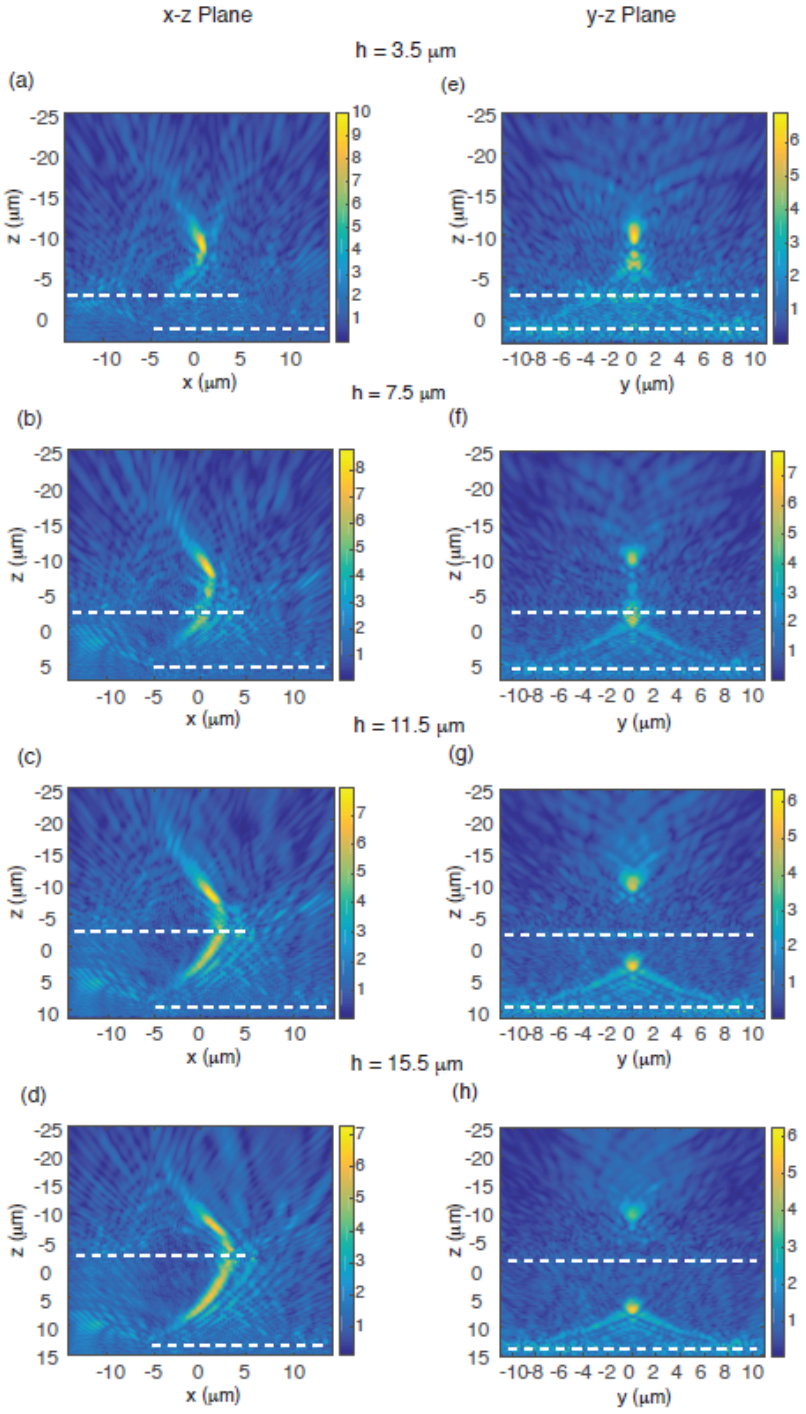

Figure 3.6: Simulated Alvarez lens performance for different separations along the optical axis, As the displacement increases, the x-z plane focal spot deforms, elongating, and also decreasing in intensity (a)-(d). However the focal length remains near 10 μm. In the y-z plane,the focal spot remains near 10 μm and retains its shape, but decreases rapidly in intensity (e)-(h). The design has an in plane displacement along x of 4 μm. The axial

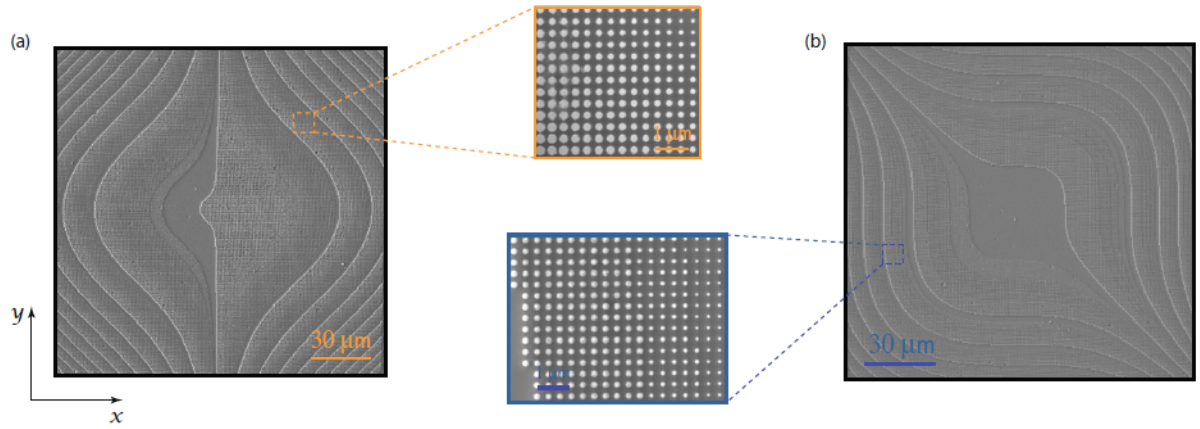

Figure 3.7: SEMs of the fabrication results for one of the (a) Alvarez phase plates, and the (b) cubic-phase plate. The orange and blue boxes are zooms of the pillars. Overetching of the cubic-phase plate is noticeable.

is mounted on a glass slide with the metasurface side facing the microscope. Coherent illumination is provided using either a red helium-neon laser, or a green solid state laser at 632 nm and 532 nm respectively incident on a 5 µm pinhole. We note that the phase plates are designed to function with incoherent illumination [69], but the power of our LEDs was not high enough to measure the PSF. Thus, intensity profiles using high power laser illumination sources were captured using the microscope and a CCD camera mounted on the translation stage as shown in Figure 3.8.

As we translate the microscope along the z axis, we image the different PSFs along the optical axis, and we can characterize its afocal behavior with respect to defocus along the z axis. The PSFs generated by the cubic phase plate are shown with respect to different values of defocus in Figure 3.9. We can see that indeed, the PSF of the element changes slowly with respect to displacements of over a range of 300 µm, confirming the depth-invariant behavior of the cubic-phase plate when compared to the PSFs generated by the lens as shown in Figure 3.10. The lens PSFs as shown in Figure 3.10 change wildly over a small defocus range of 100 µm. In addition to the PSF, we also computed the modulation transfer function (MTF) as

shown in Figure 3.11 for the cubic phase plate, and Figure 3.12 for the lens. The MTF is defined as:

$$MTF(k_x, k_y) = FT(PSF(x, y)). \tag{3.9}$$

Again, we can see that for the cubic-phase plate, the MTFs change slowly across the ranges of defocus while the lens MTF change wildly over a similar range.

In addition, we can also compare the PSFs and MTFs of the different elements at different wavelengths. The large chromatic aberrations are a central problem to metasurface optics, as shown in the previous chapter. We can understand the process of image formation by an optical system as a convolution between the original image, and the PSF of the optical system. This way, we can recognize that one pathway towards minimizing chromatic aberration is ensuring that the PSF (or MTF) of the optical system is the same at the focal plane for the wavelengths of interest [74]. From Figures 3.9 and 3.11, we can see that for red and green illumination, the PSFs and MTFs are the similar for the same values of defocus. However, based on Figures 3.10 and 3.9, we can see that the PSFs and MTFs for a quadratic lens with a focal length of 500 μm designed for operation at 632 nm vary widely at each value of defocus for red and green illumination wavelengths. This means we can use the cubic element's extended depth of focus to find a value of defocus where the PSF is the same for our wavelengths of interest. We note that this may truly enable broadband white light imaging, as the PSF would be the same for a continuous bandwidth of wavelengths at a specific value of defocus.

3.5.2 Alvarez lens

For the Alvarez lens, our experiment is primarily concerned with characterizing the range of focal lengths that it is capable of tuning over. We characterize the quality of the focus, and the actual focal length of the lens with respect to the in-plane displacement along the x-axis. The Alvarez lenses are mounted such that the two metasurfaces are facing each other to minimize the axial separation between the two plates as shown in Figure 3.13. The

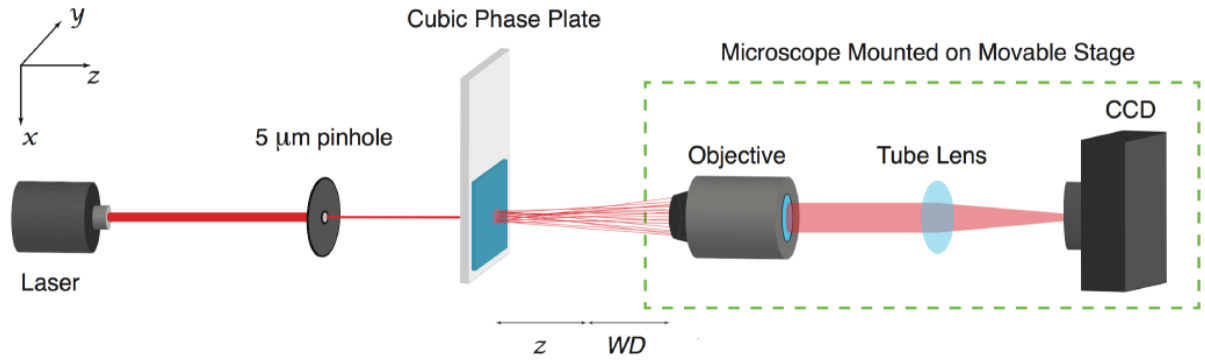

Figure 3.8: Layout of the setup used to characterize the cubic-phase element.

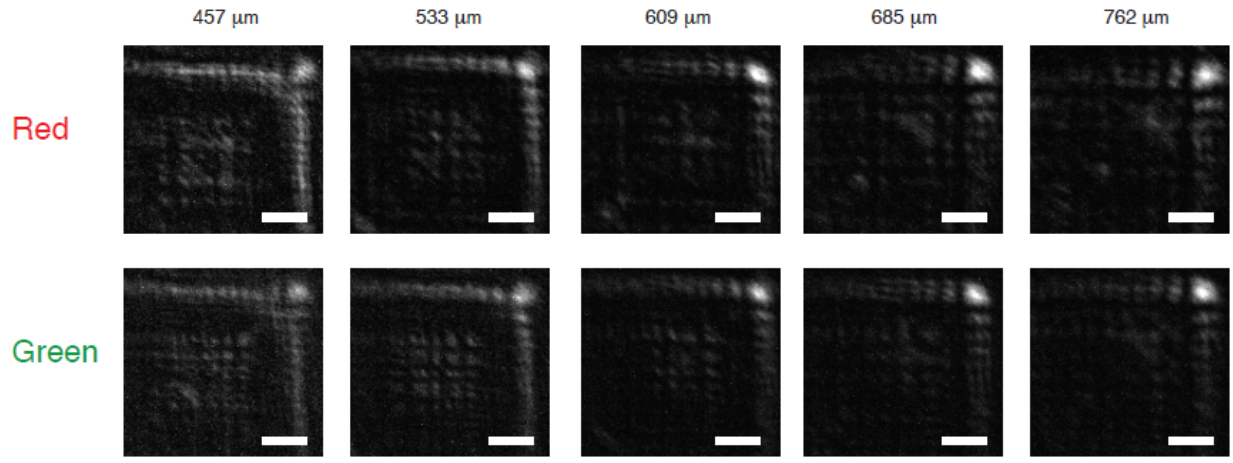

Figure 3.9: Dependence of the cubic-phase plate metasurface PSF upon defocus along the optical axis. Top and bottom rows are the PSFs of the cubic element under coherent illumination by red and green light respectively. The scale bar is 18 µm and the differences in intensities of the images are due to the difference in incident intensities of the red and green lasers exiting the pinhole.

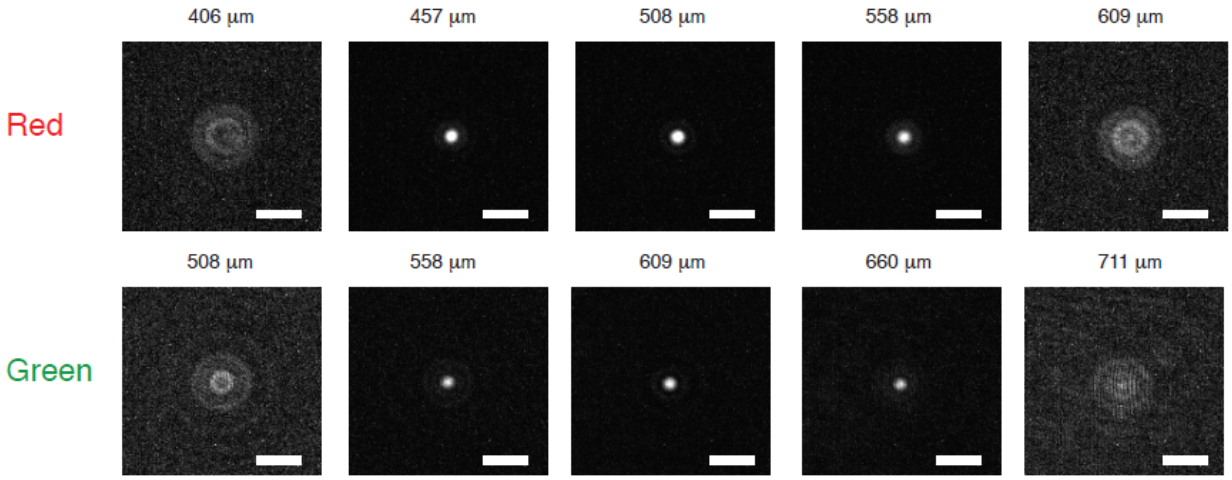

Figure 3.10: Dependence of the lens metasurface PSF upon defocus along the optical axis. Top and bottom rows are the PSFs of the lens element under coherent illumination by red and green light respectively. The scale bar is 18 μm and the differences in intensities of the images are due to the difference in incident intensities of the red and green lasers exiting the pinhole.

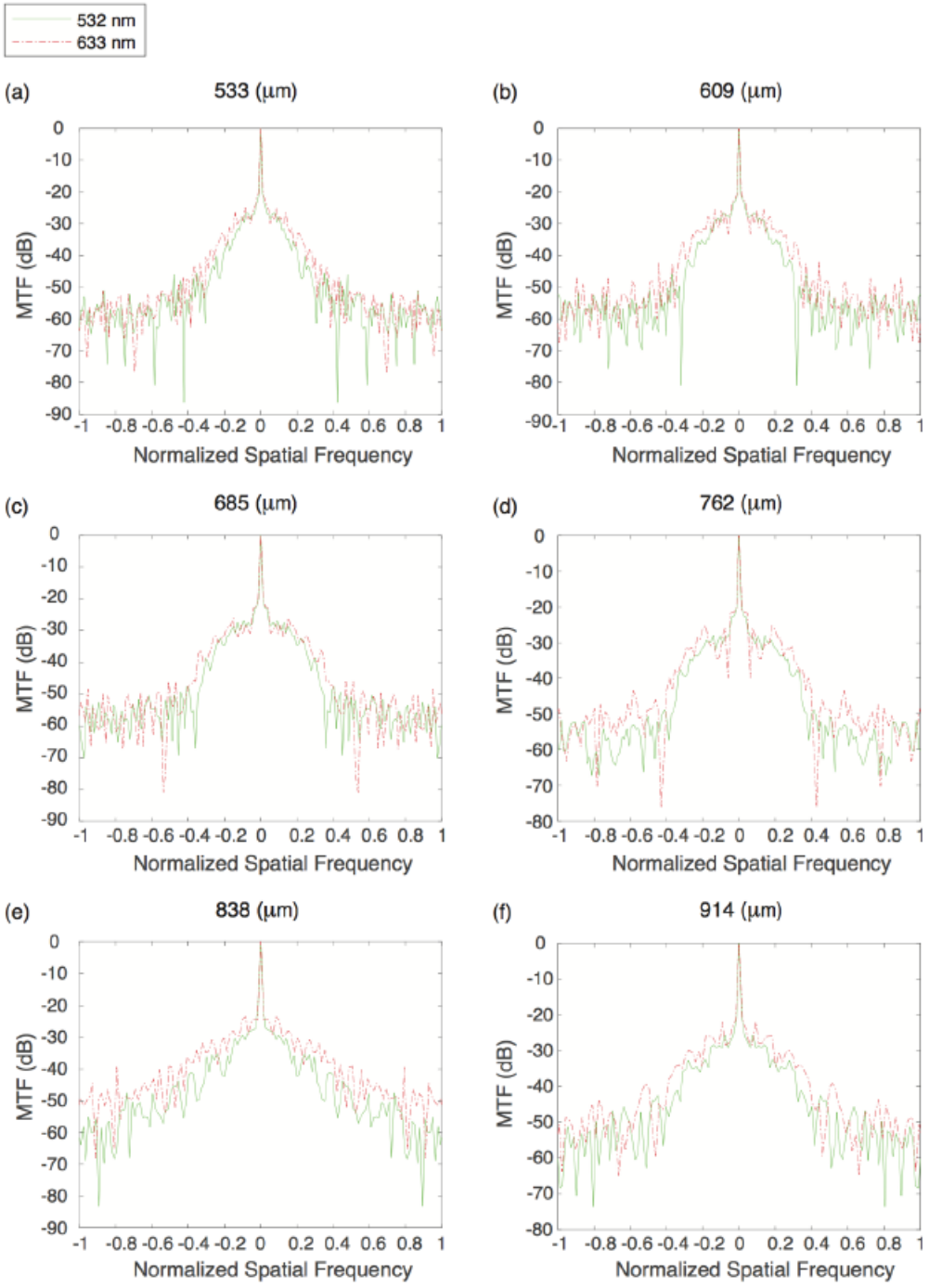

Figure 3.11: MTF of the cubic-phase element. (a)-(f) show 1D slices of the MTF of the cubic element for a range of over 300 μm plotted against normalized spatial frequency for both red and green illumination. The MTFs for green (532 nm) and red (632 nm) are shown in solid and dotted lines repectively.

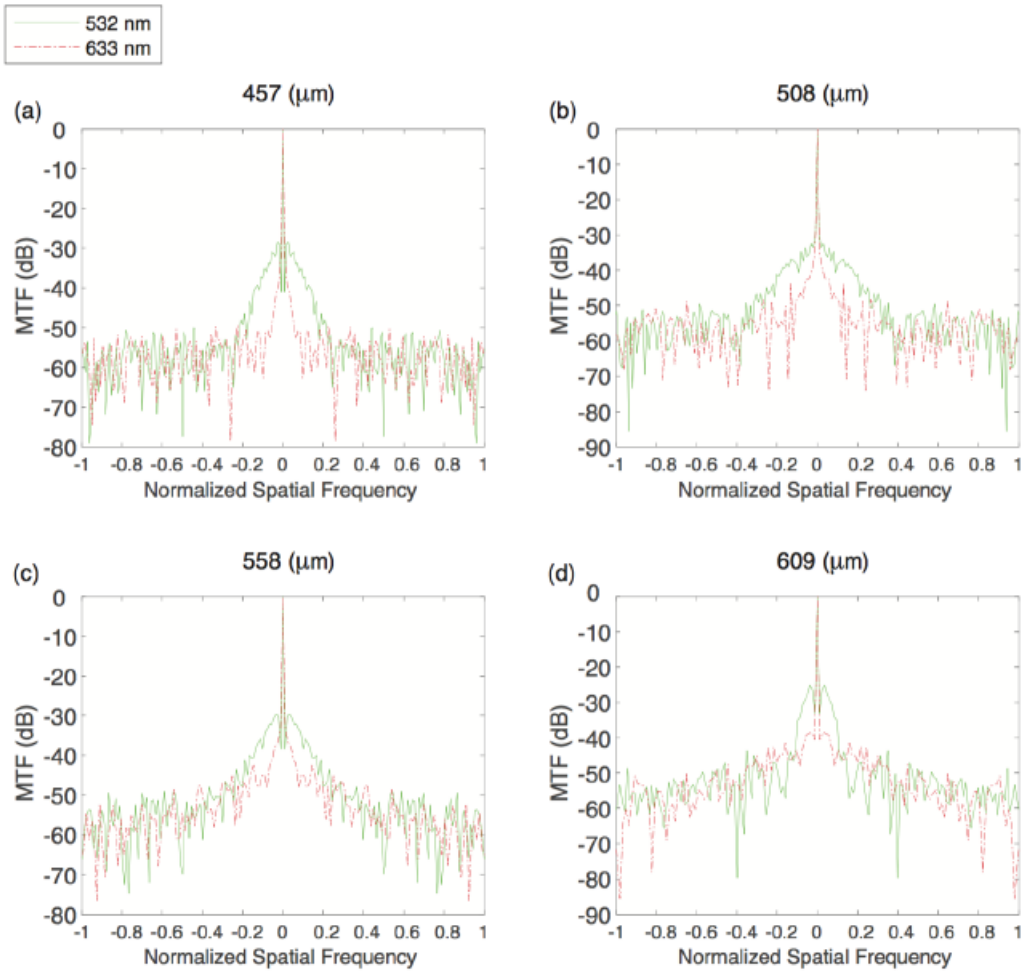

Figure 3.12: MTF of the 500 μm focal length quadratic metasurface lens. (a)-(d) show 1D slices of the MTF of the quadratic element for a range of 150 μm plotted against normalized spatial frequency for both red and green illumination. The MTFs for green (532 nm) and red(632 nm) are shown in solid and dotted lines repectively.

metasurface closer to the objective is mounted on a thinner glass coverslip with thickness $0.18mm$ in order to allow imaging for short focal lengths.

We experimentally measure the focal lengths for in-plane displacements d of each metasurface from 2 to 50 μm and we find that the focal length changes from a minimum of 0.5 mm to a maximum of 3 mm as seen in Figure 3.14a. A displacement d is constituted by displacing one metasurface a distance d, and the other a distance $-d$ along the x-axis, culminating in a total displacement of $2d$. This experiment indicates that with a physical displacement of 100 μm, the focal length changes by 2.5 mm, corresponding to a change in optical power by about 1600 diopters. While the experimentally measured focal length is significantly smaller than the simple theoretical predictions made in Figure 3.1, this is still a significant change in focal length by a mechanically actuated metasurface-based optical system. In addition, we emphasize that the lens achieves most of its focal tuning range at a small range of physical displacements, in that we can tune the focal length by 2 mm using only 60 μm of physical displacement. We performed a simple fit of the form:

$$f(d) = \frac{1}{4A_{fit}(d+B)} \tag{3.10}$$

to generate the red line shown in Figure 3.14a. The best fitting parameters are $A_{fit} = 7.97\times10^6$ m^{-2}, similar to our design value of 1.17×10^7 m^{-2}, while $B = 7.6$ μm. The parameter B represents a degree of misalignment, which is one of the major sources of the discrepancy between the experimental and measured achievable focal lengths. In addition, there is also an effect of the discretized phase profile as seen in the FDTD simulations performed on the metasurface shown in Figure 3.3a.

Another important quantity to assess the quality of a lens is its spot size, which we characterize by calculating the FWHM of a Gaussian fit to a 1D slice of the intensity data. The FWHM shows a similar dependence on lateral displacement as the focal length, and the largest focal length of 3 mm has the largest FWHM of about 20 μm, while the smallest focal length of about 0.5 mm has the smallest FWHM of 5 μm as shown in Figure 3.14b. In general, the FWHM with respect to displacement follows a similar trend as the focal length

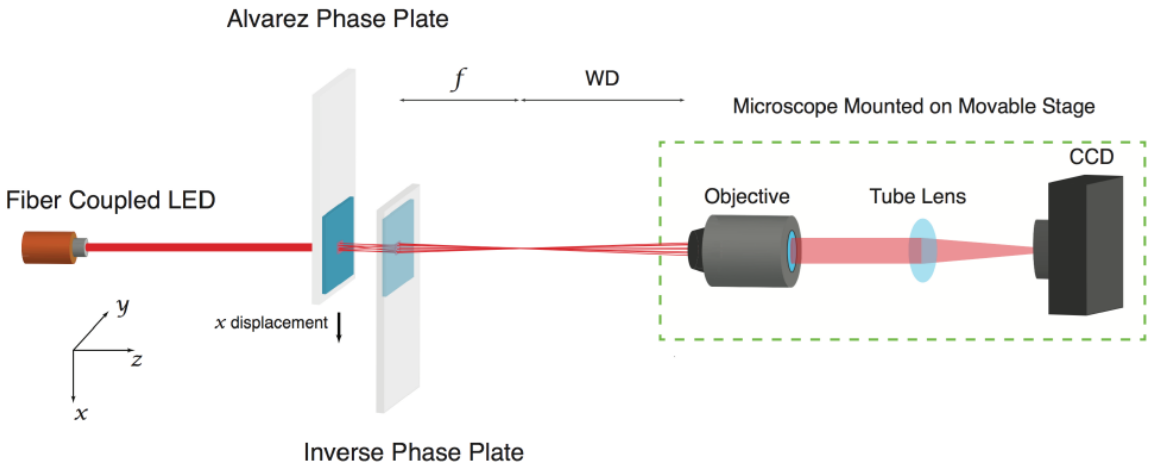

Figure 3.13: Layout of the setup used to characterize the Alvarez lens elements.

with respect to displacement. We find that our measured FWHM is generally larger than that of a diffraction-limited spot. We also characterize the behavior of the focal spot as the microscope moves into and out of the focal plane as shown in Figure 3.14c and d along the x and y axes respectively. Mirroring our previous simulation results shown in Figure 3.3c, we find that the focal spot is wider along the axis of displacement (x) than it is along the perpindicular axis (y).

Finally, we characterized the response of the Alvarez lens to axial separation in terms of its affect on the focal length and on the FWHM as shown in Figure 3.15. The separation was achieved by keeping the metasurface closest to the objective stationary while the metasurface near the illumination source was translated backwards to increase the separation. The effect on the focal spot size was not deterministic, showing no real trend. We see that the separation has a real impact on the focal length of the Alvarez lens, but not enough to account for the large discrepancy between the theoretical and experimental focal length changes.

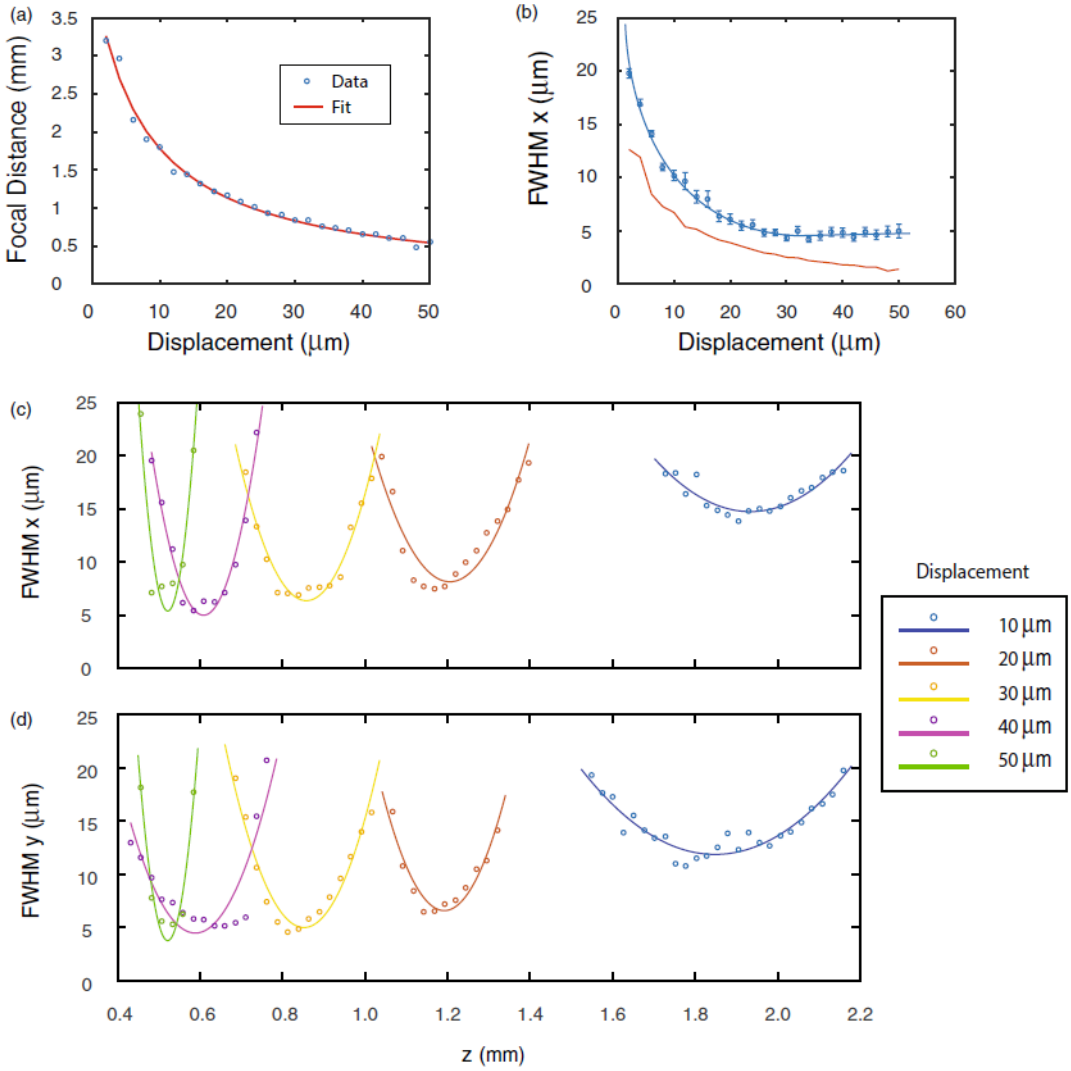

Figure 3.14: Alvarez lens performance characterization. (a) Measured focal distances of the Alvarez lens pair plotted against x displacement. The red line is a theoretical fit to the focal length data. (b) FWHM measured along the x-axis plotted against x displacement. The measured data are shown as blue points while the blue line serves as an eye guide. The red line represents the diffraction-limited FWHM. Error bars represent a 95% confidence interval of a Gaussian fit. Both (a) and (b) were taken with displacement step sizes of 2 µm. (c) and (d) are the behavior of the FWHM for five displacements along the x-axis measured along the (c) x and (d) y axes respectively. FWHM data are plotted as points, and the lines are eye guides.

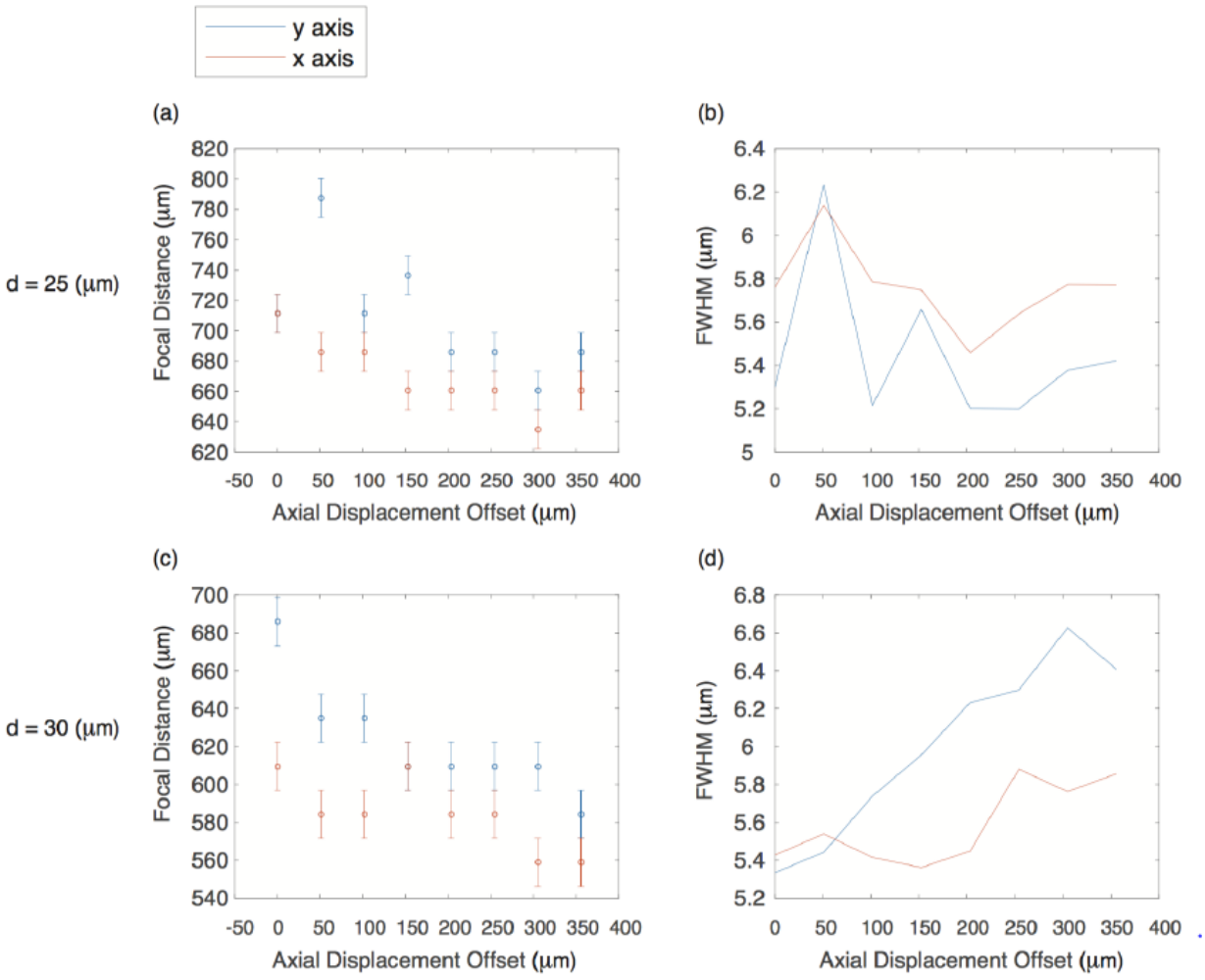

Figure 3.15: Alvarez lens performance for changes in separation between the two plates along the optical axis. (a), (c) focal distances for an Alvarez lens with 25 and 30 μm of transverse displacement d, respectively. As the displacement increases, both setups displayed a decrease in the focal length. The axial displacement is not absolute and can be interpretted as an offset of some finite distance. (b), (d) show the effect of the axial separation on the FWHM for the same displacements as in (a) and (c). Data in red and blue represent data taken along the x and y axes respectively. Error bars represent the mechanical error associated with the translation stage micrometer.

3.6 Conclusion

We have fabricated and demonstrated the performance of a metasurface-based cubic and Alvarez lens in silicon nitride. This work extends the scope of the work performed in the previous chapter into the field of freeform optics. We believe that this metasurface platform is near ideal for both adapting existing freeform optical elements, and also realizing new classes of arbitrary, spatial phase profiles. This platform also has the unprecedented ability to integrate freeform optics at the micron scale, leading to ultra-miniaturized optical systems. Using these freeform optics, we demonstrated a highly tunable Alvarez lens, in addition to demonstrating a cubic-phase element capable of mitagating the severe chromatic aberrations intrinsic to diffractive optical elements.

Chapter 4

INVERSE DESIGN BASED ON GENERALIZED LORENZ-MIE THEORY

In this chapter, we introduce a different approach to the design of discrete-scatterer-array-based optics. The presented gradient-based inverse-design method is based on generalized Lorenz-Mie theory (GLMT) and is capable optimizing large arrays of wavelength-scale spheres towards a given function. We present a general overview of the types of inverse-design methods, and give a specific treatment of gradient-based methods using the adjoint-state method. Then we present the basic mathematical structure of the matrix formulation of the GLMT forward and adjoint problems. Finally, we present some simulation results for singlet and doublet lenses and characterize them using FDTD simulations. This chapter parallels the work done in reference [75]

4.1 Motivation

Previously, we had been using a forward-design method where we identify a phase profile corresponding to an optical function, and implement it with a specific set of scatterers. This tried and true method has led to many successes in the field of metasurface optics, but has two major limitations. First, while it is suitable for optical functions with a well-defined phase profile, it is difficult in general to find a phase profile that corresponds to an arbitrary optical function. Thus forward design methods can only explore a small subset of the whole gamut of optical elements that can be built by controlling the electromagnetic waves at the single scatterer level. Even if forward design is used to produce a working device, the models generally used to produce these elements work with an idealization of a metasurface that does not utilize the full complexity of the single scatterer devices. In these systems the

sheer number of available design variables precludes the possibility of efficiently optimizing individual scatterers using a forward-design method. Both of these limitations can be avoided by using an inverse-design method. In addition, as demonstrated in the Chapters 1 and 2, the lack of memory efficient simulation methods for larger metasurfaces poses a significant limitation on their development and characterization.

4.2 Overview of Inverse Design

Inverse-design methods are methods where simulation data are interpreted and then used to produce another improved device in an automated process. In contrast to conventional forward-design methods where the design is more intuition based, inverse-design methods are data based [76–79]. Generally, an inverse-design method begins with the specification of a desired functionality, and the encapsulation of that functionality in a figure of merit (FOM). This FOM is defined as a function of modifiable variables characterizing the device, which can include the scatterer dimensions, spacing, and refractive index. Having such an FOM allows us to formulate the design process as a general optimization problem.

Inverse-design methods have a rich history in other fields, and in the context of computational electromagnetics, they have been applied to phase profile design [33, 34], single scatterer design [80], beam steering [80], and achromatic metasurface optics [81]. These methods can be classified into two major groups, local and global methods. Global methods such as genetic and particle swarm optimizations make no assumptions about the system to be optimized, allowing them to be broadly applicable in a wide variety of applications. In particular, these methods can be powerful when computing the gradient of the FOM is costly or impractical in the cases of non-differentiable, discontinuous, or discrete functions. These methods have found success in the computational electromagnetics community for both optimizing existing devices [82], and also generating new structures [83]. However, while these methods are extremely generalizable, they do not take advantage of underlying physical principles to accelerate convergence to an optimum. In contrast, gradient-based methods are more specialized, and utilize these underlying physical principles to accelerate

convergence [84–87]. While the previously mentioned methods are considered global optimization methods, gradient-based methods can only use local information, and are thus considered local methods. For general nonconvex problems considered in this thesis, local methods are guaranteed to converge to a local optimum rather than the global optimum. The following will focus specifically on gradient-based methods that calculate the gradient using the adjoint-state method.

4.2.1 The Adjoint-State Method for Optimization

The simplest way of computing a gradient is to independently vary a single parameter and monitor the change in the response of the system. This can be done for a system with N different modifiable parameters N times to compute the full gradient. However, it is obvious that for large N, this process becomes untenable as for a single step in the optimization process, we need to solve $N+1$ systems of equations, one for the initial state, and N for the modifiable parameters. The adjoint-state method is a specific tool for efficiently calculating the gradient of a system with many variables and was first used in the geophysical modeling community for solving inverse problems [88,89]. Instead of solving $N+1$ systems of equations, the adjoint method allows the entire gradient to be computed by solving only two systems of equations: one for the initial state, and one for the gradient. This powerful realization allows gradient-based methods to be suited for large scale optimizations.

It was first used for the sensitivity analysis for the systems geophysicists were interested in. In the context of optimization, it was first applied in the aerospace community [85] to generate structural elements. For computational electromagnetics, the first adjoint methods were used in the microwave regime [90], though in recent years, it has seen success in both the integrated photonics community [87, 91–95], and metasurface community [80, 96–99]. As the method is important to the following discussion, we will present an overview of the method.

The goal of our optimization problem is to optimize some figure of merit $F(\mathbf{x})$ which is an explicit function of some observables $\mathbf{x}$. Often times we do not have direct access to the observables $\mathbf{x}$, but can control them through another set of parameters $\mathbf{p}$. In this case,

our parameters $\mathbf{p}$ give rise to the observables $\mathbf{x}$ through some set of equations that defines what we call the forward problem. We can represent a linear forward problem as a matrix equation:

$$A(\mathbf{p})\mathbf{x}(\mathbf{p}) = f(\mathbf{p}), \tag{4.1}$$

where A is some matrix representing the system to be optimized, $\mathbf{x}(\mathbf{p})$ are our observables as a function of the modifiable parameters, and f is some applied drive our system responds to. Our optimization problem can now be seen as the optimization of $F(\mathbf{x}(\mathbf{p}))$ with respect to our parameters $\mathbf{p}$, so we need to find the gradient with respect to those parameters:

$$\nabla F(\mathbf{x}(\mathbf{p})) = \left[\frac{\partial F(\mathbf{x}(p_1))}{\partial p_1}, \frac{\partial F(\mathbf{x}(p_2))}{\partial p_2}, \frac{\partial F(\mathbf{x}(p_3))}{\partial p_3}, ... \frac{\partial F(\mathbf{x}(p_N))}{\partial p_N}\right], \tag{4.2}$$

where N is the total number of parameters varied. Now for a specific parameter p_i and assuming only real values, we find:

$$\frac{\partial F(\mathbf{x}(p_i))}{\partial p_i} = \frac{\partial F}{\partial \mathbf{x}}\frac{\partial \mathbf{x}}{\partial p_i}. \tag{4.3}$$

As our figure of merit is defined as an explicit function of $\mathbf{x}$, the first term in (4.3) is easy to calculate analytically by design. However, the second term in (4.3) is generally not as straightforward. We can begin by taking a derivative of (4.1) with respect to p_i, and we can find:

$$\frac{\partial}{\partial p_i}(A\mathbf{x}) = A\frac{\partial \mathbf{x}}{\partial p_i} + \frac{\partial A}{\partial p_i}\mathbf{x} = \frac{\partial f}{\partial p_i}. \tag{4.4}$$

If we are interested in brute forcing the derivatives one by one, we can do it using:

$$A\frac{\partial \mathbf{x}}{\partial p_i} = \frac{\partial f}{\partial p_i} - \frac{\partial A}{\partial p_i}\mathbf{x}. \tag{4.5}$$

This way we can solve (4.5) N times to get the required partial derivatives to complete our gradient. Alternatively, we can write:

$$\frac{\partial \mathbf{x}}{\partial p_i} = A^{-1}\left(\frac{\partial f}{\partial p_i} - \frac{\partial A}{\partial p_i}\mathbf{x}\right). \tag{4.6}$$

By inverting the A, we can simply get each partial derivative from matrix multiplications. Both of these techniques are suitable for small numbers of parameters or small matrices, but become untenable for large systems. This realization motivates the adjoint approach.

If, instead of proceeding with the above two methods, we insert (4.6) into (4.3), we find:

$$\frac{\partial F(\mathbf{x}(p_i))}{\partial p_i} = \frac{\partial F}{\partial \mathbf{x}} A^{-1} \left(\frac{\partial f}{\partial p_i} - \frac{\partial A}{\partial p_i} \mathbf{x} \right). \tag{4.7}$$

At first (4.7) appears to be a step backward as the equation has become more complex, and we are still required to compute an inverse. However, we can define a new 'adjoint' set of equations using:

$$\frac{\partial F}{\partial \mathbf{x}} A^{-1} = \lambda^T, \tag{4.8}$$

which becomes:

$$A^T \lambda = \left(\frac{\partial F}{\partial \mathbf{x}} \right)^T, \tag{4.9}$$

where λ is now a set of adjoint variables. The important quality to note is here, λ is completely independent of any parameters p_i. So when we insert (4.8) into (4.7), we find:

$$\frac{\partial F(\mathbf{x}(p_i))}{\partial p_i} = \lambda^T \left(\frac{\partial f}{\partial p_i} - \frac{\partial A}{\partial p_i} \mathbf{x} \right), \tag{4.10}$$

where the quantity $\frac{\partial A}{\partial p_i}$ contains the information of how the physical system itself is changed by changing the design parameters $\mathbf{p}$. In the following section regarding GLMT, this will be seen as the change in the matrices representing the individual particles themselves. This is the primary result of the adjoint-state method, and from Equations (4.9) and (4.10), we can see that we only need to solve the adjoint set of equations a single time to arrive at our adjoint variables. These adjoint variables can be computed a single time using Equation (4.9), and in order to compute the full gradient (4.2), we only need to perform N matrix multiplications and solve a single system of equations, instead of solving N systems of equations.

4.3 Why Generalized Lorenz-Mie Theory

While gradient-based optimization methods have been reported and used with great success in computational electromagnetics [87], in the metasurface community, their application had been limited to two dimensional devices [84,98,100], or a smaller, single unit cell in a periodic design [80]. While these devices have shown impressive functionalities, they are not suited

for the design of large extended devices. This limitation is mostly due to their approach of either meshing their design space [80, 98, 100] due to the use of a finite-difference method as the basis of the optimization method, or a current incompatibility with three dimensional designs [84].

In particular, finite-difference methods are popular due to their ease of implementation and general applicability. However, these methods scale poorly with increased system size, as their accuracy and speed both largely depend on the fineness of the mesh. A finer mesh allows for more accurate results, but also increases the number of grid points, meaning that the memory requirement will be higher and the speed lower. A general heuristic for a mesh capable of producing accurate results is $\lambda/(10n)$ where λ is the wavelength of interest, and n is the refractive index of the medium. In the case of a volume, this requires the unit of discretization to be a cube of dimension $\left(\frac{\lambda}{10n}\right)^3$. For even a small device requiring simulation region $100\lambda \times 100\lambda \times 10\lambda$, this would require an unfeasible amount of mesh points, on the order of a billion.

To circumvent these issues, we decided to use GLMT. Rather than working with finite-difference methods that require the discretization of space into small volumes, GLMT is analytical theory that describes the scattering of a plane wave from an ensemble of spheres [101, 102]. This formalism has been shown to be capable of simulating large ensembles of spheres numbering up to 100,000 [103] on a modest workstation computer, so it is suitable for use in a large-scale optimization problem. In addition, the analytical theory allows for the easy computation of the gradient, as we are guaranteed smooth, differentiable functions in the regions of interest. By using GLMT, we gain the ability to simulate and optimize large arrays of dielectric scatterers that had not been considered before. To achieve this benefit however, we lose the inherent flexibility of the finite-difference methods that allow for near arbitrary changes in scatterer geometry, so long as the mesh can support it. We deliberately limit ourselves to spherical scatterers knowing their limitations, and we study their behavior in large arrays. In the following, we will cover the forward problem largely using the notation of [103], and then the inverse problem, which is my contribution to this body of literature.

4.4 Forward Problem

In order for any inverse method to be implemented, first there must be the forward method. In the style of [102, 103] we will begin with the scattering from a single sphere, and then generalize our formalism to that of multiple spheres. As we are dealing with spherical geometries, we begin with a spherical coordinate system (r, θ, ϕ). For a more detailed coverage of GLMT theory, references [101, 102] are recommended.

In the following, we consider a single or ensemble of spheres characterized by their central positions $\mathbf{r}_i$, radii $\mathbf{R}_i$, and complex refractive index n_i, where the index $i = 1, 2, 3, ...N$ runs over a system of N spheres. These spheres are located in a homogeneous, isotropic, nonmagnetic background with refractive index n_0. The spheres are also homogeneous, isotropic, and nonmagnetic. All spheres are excited by a monochromatic incident field $\mathbf{E}_{in}$ with angular frequency ω and a time harmonic dependence is implicitly understood.

4.4.1 Scattering by a single sphere

For a single sphere, we have the well-studied Mie solution, where we can write the total field as the sum of the incoming and scattered field:

$$\mathbf{E}(\mathbf{r}) = \mathbf{E}^i_{in}(\mathbf{r}) + \mathbf{E}^i_{scat}(\mathbf{r}) \tag{4.11}$$

understanding in this case with one sphere, $i = 1$, and with:

$$\mathbf{E}^i_{in}(\mathbf{r}) = \sum_{i,n} a^i_{in,n} \mathbf{\Psi}^{(1)}_n(\mathbf{r} - \mathbf{r}_i) \tag{4.12}$$

$$\mathbf{E}^i_{scat}(\mathbf{r}) = \sum_{i,n} b^i_n \mathbf{\Psi}^{(3)}_n(\mathbf{r} - \mathbf{r}_i) \tag{4.13}$$

The incoming and scattered fields are represented in terms of regular ($\Psi^{(1)}$) and outgoing ($\Psi^{(3)}$) spherical vector wave functions (SVWF) respectively and are given by:

$$\mathbf{\Psi}^{(\nu)}_{1lm}(\mathbf{r}) = \frac{e^{im\phi}}{\sqrt{2l(l+1)}} b_l(kr) \big[im\pi_{lm}(\theta)\hat{\theta} - \tau_{lm}(\theta)\hat{\phi} \big]. \tag{4.14}$$

$$\begin{aligned}\mathbf{\Psi}^{(\nu)}_{2lm}(\mathbf{r}) =& \frac{e^{im\phi}}{\sqrt{2l(l+1)}}\Bigg\{ l(l+1)\frac{b_l(kr)}{kr}P_l^{|m|}(cos\theta)\hat{r} \\ &+ \frac{1}{kr}\frac{\partial(krb_l(kr))}{\partial(kr)}\left[\tau_{lm}(\theta)\hat{\theta} + im\pi_{lm}(\theta)\hat{\phi}\right]\Bigg\},\end{aligned} \tag{4.15}$$

where $P_l^{|m|}$ is the associated Legendre polynomial, j_l is the spherical Bessel function of the first kind, b_l is either the spherical bessel function of the first kind ($\nu = 1$) or spherical Hankel function of the first kind ($\nu = 2$), and $\pi_{lm}(\theta)$ and $\tau_{lm}(\theta)$ are given by:

$$\pi_{lm}(\theta) = \frac{P_l^m(cos\theta)}{sin\theta}, \tag{4.16}$$

and

$$\tau_{lm}(\theta) = \frac{\partial P_l^m(cos\theta)}{\partial\theta}. \tag{4.17}$$

These form a complete basis and a_n^i (b_n^i) are the coefficients of the incoming and (scattered) fields, while i indexes over each sphere, and n is a multindex that includes the polarizations $p = 1, 2$, the orbital indices $l = 1, 2, ...$, and azimuthal indices $m = -l, ...0, ...l$. The spherical scatterer couples the incoming to the scattered field, and we can characterize this coupling using the Mie coefficients. The Mie coefficients are obtained by enforcing boundary conditions at the surface of the sphere, and are given by:

$$Q^i_{1,l} = \frac{j_l(kR_i)\partial_{k_iR_i}(k_iR_ij_l(k_iR_i)) - j_l(k_iR_i)\partial_{kR_i}(kR_ij_l(kR_i))}{j_l(k_iR_i)\partial_{kR_i}(kR_ih_l(kR_i)) - h_l(kR_i)\partial_{k_iR_i}(k_iR_ij_l(k_iR_i))} \tag{4.18}$$

$$Q^i_{2,l} = \frac{k^2j_l(kR_i)\partial_{k_iR_i}(k_iR_ij_l(k_iR_i)) - k_i^2j_l(k_iR_i)\partial_{kR_i}(kR_ij_l(kR_i))}{k_i^2j_l(k_iR_i)\partial_{kR_i}(kR_ih_l(kR_i)) - k^2h_l(kR_i)\partial_{k_iR_i}(k_iR_ij_l(k_iR_i))} \tag{4.19}$$

where j_l and h_l are the spherical Bessel function of the first kind, and spherical Hankel function of the first kind, respectively. k is the wave number of light, defined as $k = \omega/c$, and k_i is the wave number of light inside the sphere, defined as $k_i = n_ik$. For spheres, these coefficients are independent of the azimuthal index m and depend only on the polarization p and orbital index l.

Equations (4.14) and (4.15) are for the different possible polarizations of incident light, and these coefficients can be collected into a diagonal matrix called the T-matrix of the form:

$$T^{i,i'}_{n,n'} = Q^i_{p,l}\delta_{p,p'}\delta_{m,m'}\delta_{l,l'}\delta_{i,i'} \tag{4.20}$$

The T-matrix of a sphere encapsulates all of its scattering properties that depend on its geometric or material properties, and depends only on these geometric properties and the refractive indices of the scatterer itself and the medium. For spherical scatterers, it is important to note that the T-matrix is diagonal in our basis. The T-matrix relates the incoming field to the scattered field:

$$b_n^i = \sum_{n',i'} T_{n,n'}^{i,i'} a_{n'}^{i'} \tag{4.21}$$

This equation completely describes the scattering of a monochromatic plane wave from a single spherical scatterer, but the problem becomes more complicated for larger ensembles of spheres.

4.4.2 Scattering by an ensemble of spheres

In the previous Section (4.4.1), we derived the scattering properties of a single sphere, which will come in handy now that we attempt to treat multiple spheres. The main difficulty in the handling of systems of multiple spheres is now not only is there an initial incident wave onto a specific sphere, but also contributions from the scattered waves of the other spheres that compose the ensemble. Mathematically, this can be represented as:

$$\mathbf{E}_{in,total}^i(\mathbf{r}) = \mathbf{E}_{in}^i(\mathbf{r}) + \sum_{i' \neq i} \mathbf{E}_{scat}^{i'}(\mathbf{r}) \tag{4.22}$$

Where now $\mathbf{E}_{in,total}^i$ represents the incident wave onto sphere i of the ensemble, and has contributions from the scattered field of all other spheres composing the ensemble. This means we must be able to transform the wave scattered from some sphere i' into the incident wave for the other spheres in the ensemble.

To accomplish this we must describe the scattered field ($\Psi_n^{(3)}$) using the same basis vector functions as the incoming field ($\Psi_n^{(1)}$), but referring to a different coordinate system. This is accomplished by expanding one basis set in terms of the basis set of another basis set using an addition theorem [102, 104, 105]. These transformations can be compiled into a coupling matrix W. We can then define a new set of incoming coefficients for each sphere in the

ensemble:

$$a_n^i = a_{in,n}^i + \sum_{i' \neq i} \sum_{n'} W_{n,n'}^{i,i'} b_{n'}^{i'}, \tag{4.23}$$

where $W_{n,n'}^{i,i'}$ represents an element of the coupling matrix that changes the representation of scattered fields. Now, we can see that the coefficients representing the incident fields (a_n^i) on a single sphere are not only a function of the initial coefficients ($a_{in,n}^i$), but also the contributions of scattered field coefficients from other spheres ($b_{n'}^{i'}$). The coupling matrix element is given by:

$$W_{n,n'}^{i,i'} = A_{n,n'}(\mathbf{r}_i - \mathbf{r}_{i'}), \tag{4.24}$$

with:

$$\mathbf{\Psi}_n^{(3)}(\mathbf{r} + \mathbf{d}) = \sum_{n'} A_{n,n'}(\mathbf{d}) \mathbf{\Psi}_{n'}^{(1)}(\mathbf{r}) for |\mathbf{r}| < |\mathbf{d}|, \tag{4.25}$$

and explicitly:

$$A_{mlpm'l'p'}(\mathbf{d}) = \delta_{pp'} A_{mlm'l'}(\mathbf{d}) + (1 - \delta_{pp'}) B_{mlm'l'}(\mathbf{d}) \tag{4.26}$$

and $A_{mlm'l'}$ and $B_{mlm'l'}$ are then given by:

$$A_{mlm'l'}(\mathbf{d}) = e^{i(m-m')\phi_d} \sum_{p=|l-l'|}^{l+l'} a_5(l, m|l', m'|p) h_p^{(1)}(kd) P_p^{|m-m'|}(cos\theta_d), \tag{4.27}$$

$$B_{mlm'l'}(\mathbf{d}) = e^{i(m-m')\phi_d} \sum_{p=|l-l'|}^{l+l'} b_5(l, m|l', m'|p) h_p^{(1)}(kd) P_p^{|m-m'|}(cos\theta_d), \tag{4.28}$$

and finally,

$$\begin{aligned} a_5(l, m|l', m'|p) =& i^{|m-m'|-|m|-|m'|+l'-l+p}(-1)^{m-m'} \\ & \times (l(l+1) + l'(l'+1) - p(p+1))\sqrt{2p+1} \\ & \times \sqrt{\frac{(2l+1)(2l'+1)}{2l(l+1)l'(l'+1)}} \begin{pmatrix} l & l' & p \\ m & -m' & m'-m \end{pmatrix} \begin{pmatrix} l & l' & p \\ 0 & 0 & 0 \end{pmatrix} \end{aligned} \tag{4.29}$$

$$\begin{aligned} b_5(l, m|l', m'|p) =& i^{|m-m'|-|m|-|m'|+l'-l+p}(-1)^{m-m'} \\ & \times \sqrt{(l+l'+1+p)(l+l'+1-p)(p+l-l')(p-l+l')(2p+1)} \\ & \times \sqrt{\frac{(2l+1)(2l'+1)}{2l(l+1)l'(l'+1)}} \begin{pmatrix} l & l' & p \\ m & -m' & m'-m \end{pmatrix} \begin{pmatrix} l & l' & p \\ 0 & 0 & 0 \end{pmatrix} \end{aligned} \tag{4.30}$$

where (d, θ_d, ϕ_d) represent $\mathbf{d}$ in spherical coordinates. If we now substitute equation (4.21) into (4.23), we find:

$$b_n^i = \sum_{n',i'} T_{n,n'}^{i,i'} a_{in,n'}^{i'} + \sum_{n',i'} T_{n,n'}^{i,i'} \sum_{i'' \neq i'} \sum_{n''} W_{n',n''}^{i',i''} b_{n''}^{i''} \tag{4.31}$$

We note here that the T matrix here is now an ensemble T-matrix with all of the individual particle T-matrices aligned on the diagonal. For a system of spheres, this corresponds to a diagonal matrix. We then move the scattered field coefficients to the same side and find:

$$\sum_{i',n'} M_{n,n'}^{i,i'} b_{n'}^{i'} = \sum_{n',i'} T_{n,n'}^{i,i'} a_{in,n'}^{i'} \tag{4.32}$$

where we have defined:

$$M_{n,n'}^{i,i'} = \delta_{n,n'} \delta_{i,i'} - \sum_{i'',n''} T_{n,n''}^{i,i''} W_{n'',n'}^{i'',i'} \tag{4.33}$$

as the system matrix. We can see now that the scattering from an ensemble of spheres can be posed as the solution to a system of linear equations. This problem constitutes the forward problem we are interested in solving, and has been implemented in a freely available software package called CELES [103].

There are a few attractive properties about this system. The first being that all of the matrix components can be easily analytically computed using mathematical functions. This means that this method does not require storing large finite difference matrices, or meshes. In addition, there is a natural separation between the material and geometric properties of the scatterers themselves in the ensemble T-matrix (T) while their relative locations are determine the coupling matrix (W). We will only be concerned about the geometric and material properties of the scatterers themselves, and not their relative positions, which will stay constant.

Next, we will describe how the formulate an adjoint problem in the context of GMMT to give a concrete example of the procedure laid out in Section (4.2.1).

4.5 Adjoint Problem

To define the adjoint problem, we must first concern ourselves with defining an FOM and making sure that we can express this FOM as a function of the parameters of interest. In this paper, we are primarily concerned with finding an optimal distribution of sphere radii that produce some desired intensity in the far field. We first describe how to define a figure of merit as a function of the sphere radii. Then, we use this figure of merit to formulate the full adjoint system of equations to be solved in order to obtain the full gradient.

4.5.1 Figure of merit design

There are many different suitable choices for a figure of merit, but for this first demonstration, we begin with a simple choice: the intensity at a single point in space or $I(\mathbf{r}_0)$ where $\mathbf{r}_0$ is the point of interest. There are a chain of variables that are involved in computing an intensity, and we can explicitly write them as:

$$FOM(\mathbf{R}) = I(\mathbf{r}_0; R_j) = |\mathbf{E}(\mathbf{r}_0; R_j)|^2 = |\sum_{i,n} b_n^i(R_j)\mathbf{\Psi}_n^{(3)}(\mathbf{r}_0 - \mathbf{r}_i)|^2 \tag{4.34}$$

where the explicit dependences on the sphere radii R_j have been shown. Now we know that in order to be able to arrive at an expression for the gradient, we must determine how the scattering coefficients of the sphere array (b_n^i) change with the sphere radii (R_j).

4.5.2 Computing the gradient

As before, we begin by applying a gradient operator onto our figure of merit as in Equation (4.2).

$$\nabla_{\mathbf{R}} FOM(\mathbf{R}) = \left[\frac{\partial FOM}{\partial R_1}, \frac{\partial FOM}{\partial R_2}, \frac{\partial FOM}{\partial R_3}, ... \frac{\partial FOM}{\partial R_N}\right] \tag{4.35}$$

where $\nabla_{\mathbf{R}}$ is the gradient with respect to the particle radii $\mathbf{R}$, and each of the terms inside the bracket is an individual term. As we are differentiating a real number FOM with respect to another real number R_j, we should expect all of these individual terms to be real as well.

However, unlike in the previous case, when we use the chain rule naively in this situation as:

$$\frac{\partial FOM}{\partial R_j} = \frac{\partial FOM}{\partial b_n^i}\frac{\partial b_n^i}{\partial R_j} \tag{4.36}$$

we arrive at a complex value in general. To remedy this we employ the Wirtinger derivatives, which in essence allow us to treat a variable α and its complex conjugate α^* as independent variables. This way, we can remedy equation (4.3) as:

$$\frac{\partial FOM}{\partial R_j} = \frac{\partial FOM}{\partial b_n^i}\frac{\partial b_n^i}{\partial R_j} + \frac{\partial FOM}{\partial \left(b_n^i\right)^*}\frac{\partial \left(b_n^i\right)^*}{\partial R_j} = 2\,\mathrm{Re}\left\{\frac{\partial FOM}{\partial b_n^i}\frac{\partial b_n^i}{\partial R_j}\right\} \tag{4.37}$$

where we take the real part in the final step. We can then find the analytical derivative of the FOM with respect to our scattering coefficients:

$$\frac{\partial FOM}{\partial b_n^i} = \mathbf{E}^*(\mathbf{r}_0)\cdot\mathbf{\Psi}_n^{(3)}(\mathbf{r}_0-\mathbf{r}_i) \tag{4.38}$$

Where * denotes the complex conjugate of a variable. Now following the procedure outlined in Section 4.3, we first take a derivative of Equation (4.32) with respect to a particle radius R_i (now omitting the summations, and understanding that repeated indices are summed over):

$$\frac{\partial b_{n'}^{i'}}{\partial R_j} = \left(M_{n,n'}^{i,i'}\right)^{-1}\left(\frac{\partial T_{n,n'}^{i,i'}}{\partial R_j}a_{in,n'}^{i'} + \frac{\partial T_{n,n''}^{i,i''}}{\partial R_j}W_{n'',n'}^{i'',i'}b_{n'}^{i'}\right) \tag{4.39}$$

Taking this derivative, we see that there is a new term that we must consider, the partial derivative of the T-matrix with respect to the parameter we are modifying. In this specific case, it is easily handled by taking derivatives of the Mie coefficients from equations (4.14) and (4.15), as shown in [106, 107] resulting in a diagonal derivative matrix. We will describe the formulation of the T-matrix derivative of a general particle in the next chapter. As before, we can insert equation (4.39) into equation (4.37) to arrive at:

$$\frac{\partial FOM}{\partial R_j} = 2\,\mathrm{Re}\left\{\frac{\partial FOM}{\partial b_{n'}^{i'}}\left(M_{n,n'}^{i,i'}\right)^{-T}\left(\frac{\partial T_{n,n'}^{i,i'}}{\partial R_j}a_{in,n'}^{i'} + \frac{\partial T_{n,n''}^{i,i''}}{\partial R_j}W_{n'',n'}^{i'',i'}b_{n'}^{i'}\right)\right\} \tag{4.40}$$

and we can define our 'adjoint' coefficients (λ_n^i) in a system of coupled equations analogously to equation (4.9):

$$\left(M_{n,n'}^{i,i'}\right)^{T}\lambda_n^i = \left(\frac{\partial FOM}{\partial b_{n'}^{i'}}\right) \tag{4.41}$$

These adjoint coefficients are dual to the scattering coefficients we computed in the forward problem. If we understand the scattering coefficients as the current system's response to an incident plane wave, we can understand the adjoint coefficients as the response of the current system to the wave that satisfies our FOM. We can then solve the adjoint system of equations and arrive at an expression of our gradient:

$$\frac{\partial FOM}{\partial R_j} = 2\,\mathrm{Re}\left\{ \left(\lambda_n^i\right)^T \left(\frac{\partial T_{n,n'}^{i,i'}}{\partial R_j} a_{in,n'}^{i'} + \frac{\partial T_{n,n''}^{i,i''}}{\partial R_j} W_{n'',n'}^{i'',i'} b_{n'}^{i'} \right) \right\} \tag{4.42}$$

As before we see that λ_n^i is independent of R_j, the parameters we are optimizing over. This means that we only need to compute the adjoint coefficients once per iteration of the inverse-design algorithm.

4.6 Gradient-based Optimization Loop

The gradient we computed in the previous section provides us with the direction in which we move our array of spheres to approach a local optimum as our FOM is not shown to be a convex function of our variables. Gradient-based optimization is an iterative process where a given initial condition is updated according to the direction given by the gradient. Each iteration of the algorithm consists of two sub-problems; first we must solve the forward problem to compute the FOM, and then we solve the adjoint problem to compute the gradient. We continue to iterate the system until the FOM or gradient reaches a set condition where we determine the optimization to have converged. The above code is implemented in MATLAB, where the forward problem is solved using CELES [103], and the adjoint problem solver is our own code added in. The code takes advantage of a CUDA accelerated matrix-vector multiplication which is the slowest part of the process.

We verify our simulation process by testing the FOM in Equation (4.34). By maximizing the FOM, we are maximizing the intensity at a single point in space in the far field of the optical element. This can be thought of as a lens, and is an easy function to check.

4.7 Results

In this section we present the simulation results of obtained using the gradient optimization procedure. First, we use the gradient optimization to arrive at an array of spheres that satisfies our FOM, then we simulate the structure using Lumerical's FDTD program to crosscheck our result between a finite difference method and also the analytic GLMT solution. First we present the general optimization numerics, and then we present specific results.

4.7.1 Optimization setup

The radii of the array of spheres are continually updated using gradient descent with a fixed step size. The optimization routine runs to a fixed number of iterations, in our case chosen to be 200. We designed two sets of optical elements, each consisting of a singlet (one layer of spheres) and a doublet (two layers of spheres) analog. One set of elements is designed with a sub-wavelength periodicity, the other with a super-wavelength periodicity.

All of the elements are designed to maximize the intensity at a point 50 μm away from the center of the device. The spheres have a constant refractive index of 1.52 corresponding to that of the highest resolution resist available for the Photonic Professional Nanoscribe GT. The devices are taken to lie in the x-y plane with the optical axis along z. Our excitation is a monochromatic plane wave polarized along the y axis at normal incidence (propagating along the z axis) at wavelength $\lambda = 1550$ nm. For all optimizations, we assume that the spheres are suspended in a vacuum ($n = 1$), with no substrate.

Both the forward and adjoint systems of equations are solved using biconjugate gradient stabilized (BiCGSTAB) with a block-diagonal preconditioner. For such large systems of equations, iterative solvers are much more memory efficient and faster than direct solvers such as lower-upper substitution.

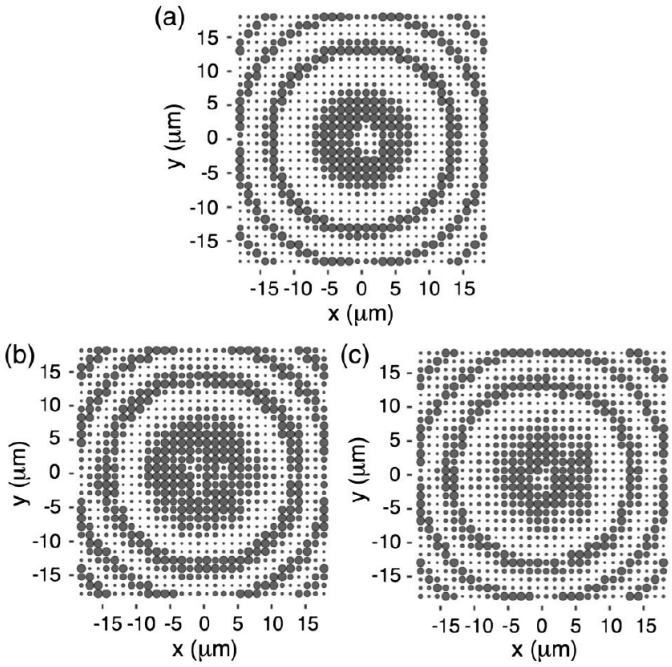

Figure 4.1: Final radius distribution of the sub-wavelength elements with periodicity 1240 nm, which is less than the operating wavelength of 1550 nm. Radii are allowed to range within 150 to 600 nm. The sub-wavelength singlet is shown in (a), while the bottom (illumination facing) and top (image facing) layers of the doublet are shown in (b) and (c) respectively.

4.7.2 Sub-wavelength devices

Now we present two optical elements designed with a sub-wavelength periodicity. Scatterer-based elements with sub-wavelength periodicity are termed metasurfaces, and are of great interest due to their ability to control the propagation of diffractive orders. For both the singlet and doublet elements we being with a square grid of periodicity 1240 nm populated with identical spheres with radius 300 nm. We allow these spheres to vary continuously between 150 and 600 nm. For GLMT, these geometric and material properties correspond to a multipole cut-off of $l = 3$. For further discussion on the dependence of multipole cut off on the sphere parameters we refer to the expansion order cutoff section.

For the singlet lens we begin with a single layer of 30×30 spheres with a final dimension of 36 μm ×36 μm ×1.2 μm. The final radius distribution is shown in Figure 4.1a. We can see that the result is mostly circularly symmetric, as expected for a lens. There is so asymmetry near the origin of the lens. For the doublet lens, we begin with two layers of 30×30 spheres with a final dimension of 36 μm ×36 μm ×2.4 μm. The final radius distributions of the bottom (illumination facing) and top (image facing) surfaces are shown in Figure 4.1b and Figure 4.1c respectively. Again the design is mostly circularly symmetric, as expected based on our figure of merit, but there is also noticeable asymmetry towards the middle of the lens.

We attribute this to our algorithm running for a fixed number of iterations instead of full convergence to a local optimum. Our gradient-based method only guarantees convergence to a local optimum, and we manually terminate the algorithm when we achieve the desired performance as described by the FOM. We note that the maximum number of iterations was a parameter we were able to tune along with the step size during our optimization process.

From our simulations in FDTD, we verify a clear focal spot at 50 μm in the x-z plane in Figure 4.2a. In addition, we characterized the performance under chromatic illumination and see that the focal length changes linearly with the wavelength in this small bandwidth as shown in Figure 4.2b. We note that this is consistent with diffractive optical devices as the product of our focal length and operating wavelengths $f\lambda$ are constant [56]. Lastly we characterize the focal spot size produced (characterized by FWHM), and plot its dependence on illumination wavelength as shown in Figure 4.2c. We can see that the FWHM along the x and y directions behave differently, and produce an asymmetric focal spot. We attribute this choice to our FOM, which does not constrain the optimization routine to a symmetric focal spot.

To demonstrate the suitability of the algorithm for designing fully three-dimensional arrays of scatterers, we also demonstrate a doublet design with two layers of spheres. We simulate the radius distribution in FDTD and again observe a clear focal spot at the design location of 50 μm in both the x-z and y-z planes as shown in Figure 4.3a. We do the same set of characterizations as the singlet case, and we find that the chromatic focal shift is

almost the same as that of the singlet as shown in Figure 4.3b. However, we see a noticeable improvement in the focal spot size compared to that of the singlet in Figure 4.3c. The focal spot is noticeably smaller across the entire bandwidth, and again, the focal spot size is asymmetric.

4.7.3 Super-wavelength devices

We also designed a set of two devices with a super-wavelength periodicity. In contrast to the sub-wavelength devices, these are not considered metasurfaces as they have a periodicity that exceeds the wavelength of the incident light. As such they represent elements that are more easily fabricated with available techniques. For both elements we begin with identical spheres with radius 700 nm on a square grid with periodicity 2050 nm. We allow the spheres' radii to vary continuously between 150 and 1000 nm, making our multipole cutoff $l = 4$.

For the singlet lens we begin with a 30×30 layer of spheres with final dimensions of 60 μm $\times$60 μm $\times$2 μm. The final radii values are shown in Figure 4.4a. For the doublet lens we begin with two 30×30 layers of spheres, separated by a center-to-center distance of 4 μm. This results in final dimensions of 60 μm $\times$60 μm $\times$8 μm. The bottom (illumination-facing) and top (image-facing) layers are shown in Figures 4.4b and c, respectively.

From our simulation, we find a clear focal spot at a distance of 45 μm away from the lens in the x-z and y-z planes under 1548 nm illumination as shown in Figure 4.5. This result is not consistent with the design focal length at 1550 nm, and we attribute this discrepancy to the difference in mesh sizes of our design space between the super-wavelength and sub-wavelength devices when validated in FDTD. As the super-wavelength devices are appreciably larger than the sub-wavelength devices, we were unable to mesh the super-wavelength devices to the same accuracy. Again, this device's focal length displays a linear dependence on wavelength in this bandwidth shown in Figure 4.5b. Lastly we calculate the FWHM at the focal length of 45 μm, and find spot sizes on the order of the diffraction-limited FWHM with no spot sizes smaller.

Then, as for the sub-wavelength devices, we also check the performance of the super-

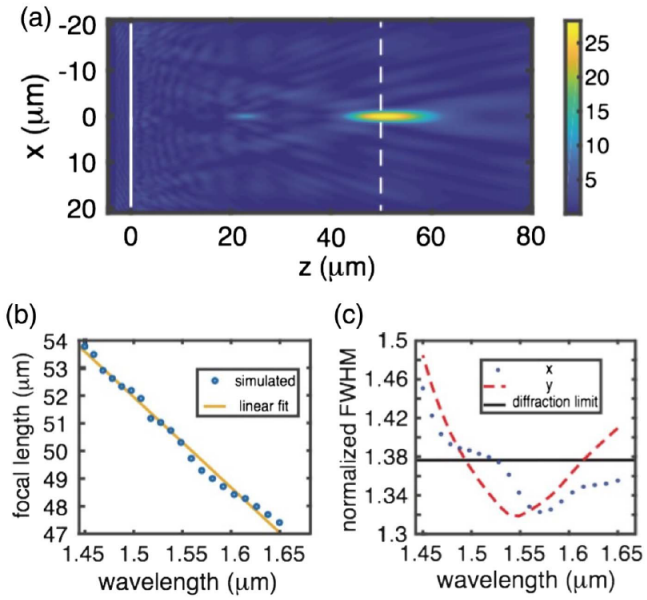

Figure 4.2: Performance of the sub-wavelength singlet as simulated using FDTD. (a) Intensity of the x-z plane under illumination at 1548 nm showing a clear focal spot at 50 μm. The data used to compute the FWHM is taken from the white dashed line, and the layers of sphere are located at the solid white line. (b) is the dependence of the focal length on incident wavelength, showing a linear dependence within this bandwidth. The focal length shifts 7 μm over this bandwidth. (c) is the calculated normalized FWHM of the singlet from the data taken from the white-dashed line in (a). The FWHM is obtained by fitting the intensity peak to a Gaussian. The blue dotted and red dashed lines represent fits based on data taken along the x and y axes respectively. The black line is the diffraction limit for an ideal lens with the same geometric parameters as the design. All normalized FWHM data points are obtained by dividing the FWHM data by their respectively wavelengths.

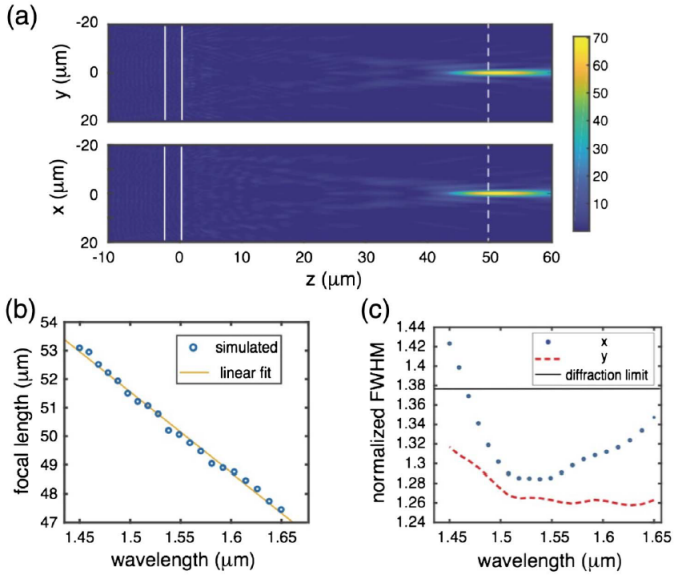

Figure 4.3: Performance of the sub-wavelength doublet as simulated using FDTD. (a) Intensity of the x-z and y-z planes under illumination at 1548 nm showing a clear focal spot at 50 μm. The data used to compute the FWHM is taken from the white dashed line, and the layers of spheres are located at the solid white line. (b) is the the dependence of the focal length on incident wavelength, showing a linear dependence within this bandwidth. The focal length shifts 7 μm over this bandwidth. (c) is the calculated normalized FWHM of the doublet from the data taken from the white dashed line in (a). The FWHM is obtained by fitting the intensity peak to a Gaussian. The blue dotted and red dashed lines represent fits based on data taken along the x and y axes respectively. The black line is the diffraction limit for an ideal singlet lens with the same geometric parameters as the design. All normalized FWHM data points are obtained by dividing the FWHM data by their respective wavelengths.

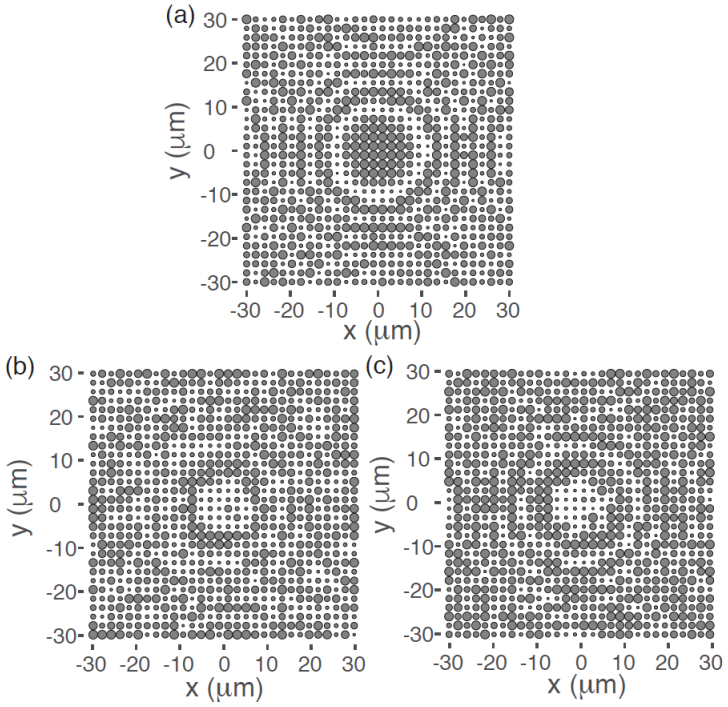

Figure 4.4: Final radius distribution of the super-wavelength elements with periodicity 2050 nm. Radii are allowed to range from 150 to 1000 nm. (a) is the super-wavelength singlet. (b) and (C) are the bottom (illumination-facing) and top (image-facing) layers of the doublet respectively.

wavelength doublet. The simulation shows a clear focal spot at 45 μm in both the x-z and y-z planes as shown in Figure 4.6a. Again, this is not the design focal length, and we attribute this difference again to the discretization of the mesh. Figure 4.6b shows the same linear dependence on incident wavelength as the previous devices. The focal spots achieved by the doublet in Figure 4.6c were generally larger than those of the singlet. We would expect the addition of the second layer of spheres to improve the performance of the device, and do not know why the doublet does not result in better focusing performance. The doublet also produces a more asymmetric focal spot as shown by the differences in the FWHM along the x and y directions.

4.7.4 Substrate effects

In any feasible experimental demonstration of these presented elements, it is likely that the spheres will be sitting on some substrate. We attempt to quantify the effect of a likely experimental configuration of the sub-wavelength doublet in FDTD by adding two 800 nm spacer layers, one between the top and bottom layers, and one below the bottom layer. Both of these spacer layers have the same refractive index as the spheres as shown in Figure 4.7, and then the entire structure is mounted on a quartz substrate with $n = 1.45$. Lastly the spheres are displaced such that instead of their center points aligning, they sit flat on the substrate with their bottoms aligned.

The simulation results of this new device configuration are presented in Figure 4.8. Similarly to the device with no substrate or extra layers, the device still focuses at 50 μm, but the focal spot intensity shows a noticeable decrease in Figure 4.8a. The same linear dependence on illumination wavelength is observed as in the previous demonstrations. The spot sizes of the lens with added substrate are also larger than those of the ideal case as in Figure 4.8c, but the device still shows high performance. We see that the displacement of spheres and the addition of extra dielectric layers (substrate and spacer layers) has a noticeable effect on the performance of the device, but the overall behavior is still qualitatively similar.

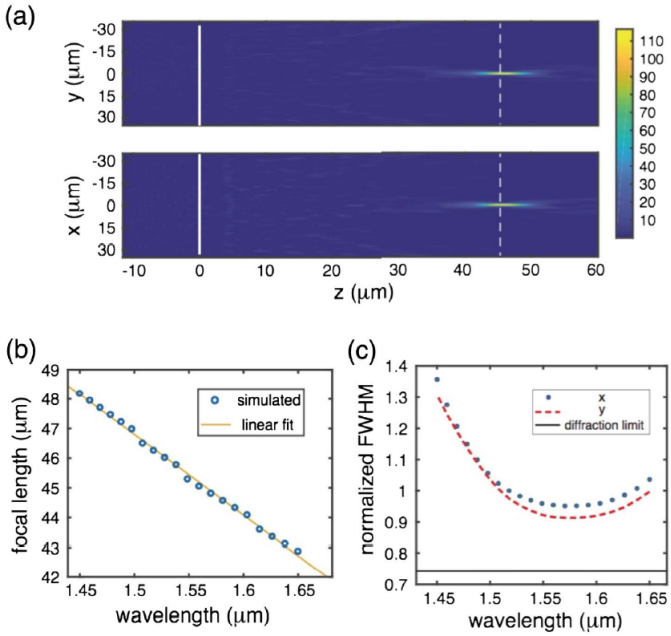

Figure 4.5: Performance of the super-wavelength singlet in FDTD. (a) is the intensity of the x-z and y-z planes showing clear focusing at 45 μm under illumination by 1548 nm light. Data used to compute the FWHM is taken from the white dashed line, and the layer of spheres is located at the solid white line. (b) shows the dependence of the focal length on illumination wavelength showing a clear linear relationship in this bandwidth. (c) Calculated FWHM using data from the white dashed line in (a). The FWHM is obtained by fitting the intensity peak to a Gaussian. Blue dotted and red dashed lines represent fits taken from data taken along the x and y axes respectively. The black line is the diffraction limit for an ideal lens with the same geometric parameters as the design. All normalized FWHM data points are obtained by dividing the FWHM data by their respective wavelengths.

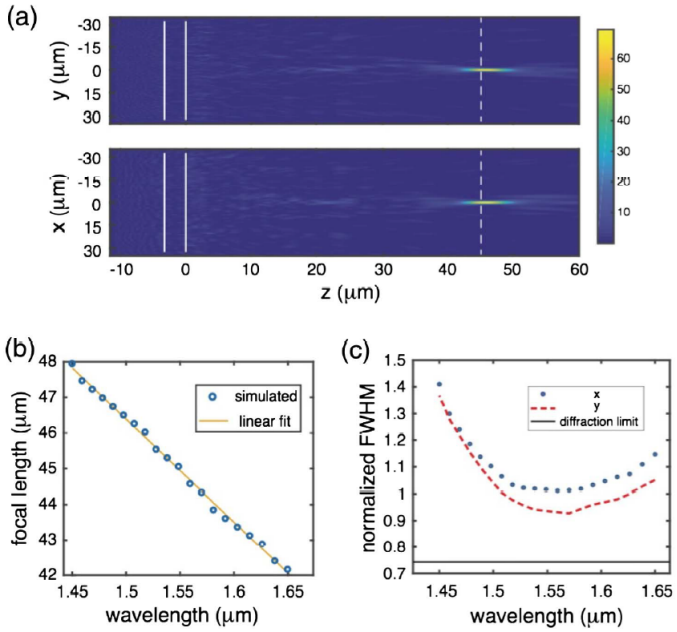

Figure 4.6: Performance of the super-wavelength doublet in FDTD. (a) is the intensity of the x-z and y-z planes showing clear focusing at 45 μm under illumination by 1548 nm light. Data used to compute the FWHM is taken from the white dashed line, and the layers of spheres are located at the solid white line. (b) shows the dependence of the focal length on illumination wavelength showing a clear linear relationship in this bandwidth. (c) Calculated FWHM using data from the white dashed line in (a). The FWHM is obtained by fitting the intensity peak to a Gaussian. Blue dotted and red dashed lines represent fits taken from data taken along the x and y axes respectively. The black line is the diffraction limit for an ideal lens with the same geometric parameters as the design. All normalized FWHM data points are obtained by dividing the FWHM data by their respective wavelengths.

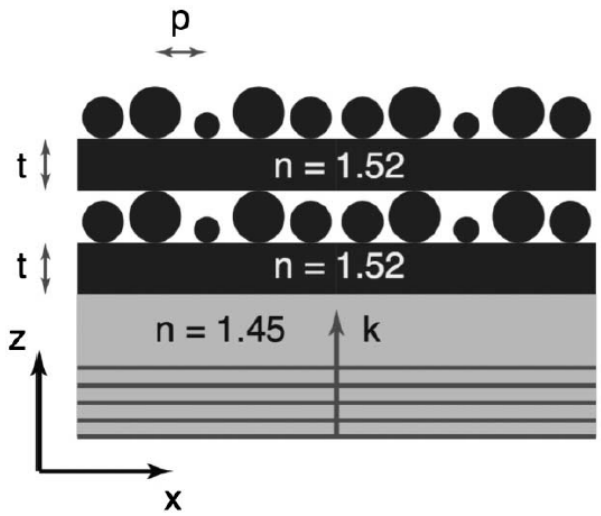

Figure 4.7: Substrate schematic diagram showing the sub-wavelength doublet with the spacer layers and substrate added. The thickness (t) of the spacer layers is 800 nm, periodicity (p) is 1240 nm, and the light with wave vector k is incident from below through a quartz substrate with index $n = 1.45$.

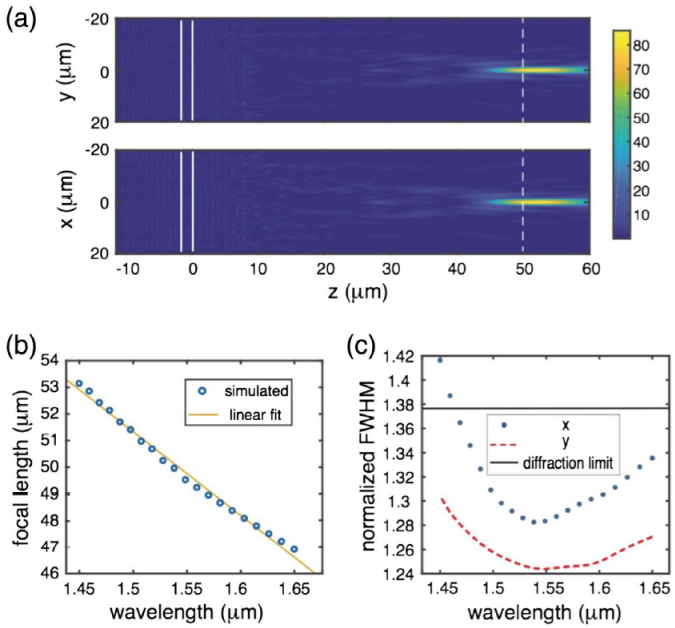

Figure 4.8: Performance of the sub-wavelength doublet with added dielectric layers as simulated using FDTD. (a) Intensity of the x-z and y-z planes under illumination at 1548 nm showing a clear focal spot at 50 μm. The data used to compute the FWHM is taken from the white dashed line, and the layers of spheres are located at the solid white line. (b) is the the dependence of the focal length on incident wavelength, showing a linear dependence within this bandwidth. The focal length shifts 7 μm over this bandwidth. (c) is the calculated normalized FWHM of the doublet from the data taken from the white dashed line in (a). The FWHM is obtained by fitting the intensity peak to a Gaussian. The blue dotted and red dashed lines represent fits based on data taken along the x and y axes respectively. The black line is the diffraction limit for an ideal singlet lens with the same geometric parameters as the design. All normalized FWHM data points are obtained by dividing the FWHM data by their respective wavelengths.

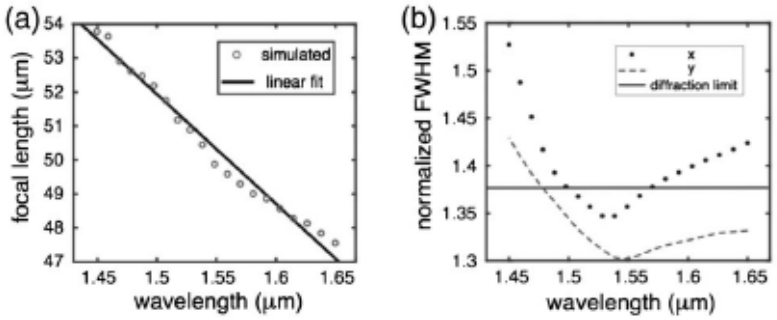

Figure 4.9: Performance of the sub-wavelength singlet under illumination by an x polarized plane wave. (a) Focal length dependence on wavelength, and (b) spot size (FWHM) dependence on wavelength calculated at 50 μm. Solid black line is the calculated diffraction limited FWHM, black dotted (dashed grey) line is the FWHM along the x (y) direction. All normalized FWHM data points are obtained by dividing the FWHM data by their respective wavelengths.

4.7.5 Polarization dependence

During the optimization process, we assume the incidence of a single linearly polarized plane wave along the y axis. We neglect to optimize for the orthogonal polarization. In order to check the performance for the orthogonal polarization, we simulate the performance of the sub-wavelength singlet under illumination by this orthogonal polarization. As shown in Figure 4.9, the design still focuses to a similar focal length, and has a similar spot size. We again plot the spot size and chromatic behavior of the focal length and see little change in the performance of the device.

4.8 Expansion Order Cutoff

The iteration time of the inverse design method depends on both the particle number and the expansion order. Larger numbers of particles or expansion orders increase the iteration time and memory requirement by both increasing the number of stored variables, and the

dimension of the system of equations to be solved. As we are interested in simulating large arrays of particles, it is important to find a reasonable cutoff expansion to balance the speed of the iteration and the accuracy of the result.

The valid cutoff expansion order is ultimately determined by the scattering properties of individual spheres described by their Mie coefficients. These scattering properties are determined by the geometric and material properties of the sphere in addition to the wavelength of input light. Figure 4.10 displays the absolute value of the calculated Mie coefficients for our spheres with radii ranging between 150 to 1500 nm and a refractive index of $n = 1.52$ under illumination by a 1550 nm input plane wave polarized along the y axis. We see that the spheres in the sub-wavelength regime only scatter up to $l = 3$, and the super-wavelength spheres only scatter up to $l = 4$, justifying our cutoff.

From the Mie coefficients, we can find the optical response of particles of varying radii. It is clear that the use of larger spheres requires larger expansion orders, increasing computation time. However, larger expansion orders also correspond to being able to control higher-order spherical waves.

4.9 Machine Specifications and Software

The forward simulation is a version of the freely available CELES software [103]. The inverse simulation is a custom written extension to CELES. The specification of the hardware and software used in this paper are as follows:

- 2x Intel E5-2620
- NVIDIA Tesla K40 12GB
- 64 GB DDR3
- CentOS 7
- Matlab 2017a

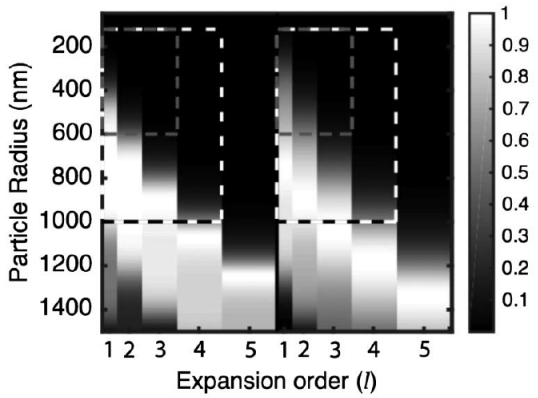

Figure 4.10: Absolute value of Mie coefficients under illumination by 1550 nm light. Light (dark) dashed boxes indicate the range of parameters used for the devices designed for sub-wavelength (super-wavelength) devices. The Mie coefficients for isotropic uniform spheres have no dependence on the azimuthal number m, so all coefficients of a given orbital number l are equivalent. The two sets of data on the left and right correspond to two different polarizations.

- CUDA 8.0

The implementation is available in a zipped file at: `https://github.com/azhan137/inverse_design`

4.10 Conclusion

We described and presented an inverse-design method using adjoint optimization and GLMT. We then demonstrated the suitability of this method for designing fully three-dimensional single and multi-layer optics by presenting the performance of two sets of singlet and doublet lenses. The power of this method is in the efficient and accurate simulation of large ensembles of discrete scatterers made possible by the use of GLMT. While methods such as FDTD are accurate, they suffer from memory-scaling limitations. Conversely, on the other hand, methods where the device is modeled as an ideal phase profile are efficient, but do not accurately capture the physics of the complex system of coupled scatterers. While we have chosen to present results in the infrared regime, the method makes no assumptions about the wavelength of light and is well-suited for calculating scattering from any distribution of wavelength-scale spherical scatterers. This work constitutes a significant step forward in the use of inverse-design techniques to design scatterer-array-based optical elements.

Chapter 5

EXPERIMENTAL DEMONSTRATION OF INVERSE DESIGN BASED ON GENERALIZED LORENZ-MIE THEORY

In this chapter we present an experimental demonstration of the inverse-design method presented in Chapter 4. The device is based on wavelength-scale spheres and is fabricated using the Nanoscribe GT two-photon lithography system. The device that is designed and characterized is an element that demonstrates both of the strengths of the GLMT based inverse-design method. First, it is a large-area device with an area of 144 μm ×144 μm, making it the largest inverse-designed, discrete-scatterer-array-based optic, and it also has a non-trivial optical function that would be difficult to engineer using forward-design methods. The device focuses an incident plane wave at 1550 nm with linear polarization into a set of discrete focal spots that wind in a helical pattern about the optical axis. This depth-variant PSF that changes predictably for a range of defocus values can allow an imaging system to discriminate between objects at different depths.

5.1 Motivation

We have already described and numerically tested an inverse-design method based on GLMT to implement a given optical function defined by an FOM using an array of spherical scatterers. While this method has been validated in simulation, we also want to verify that it is able to produce devices that are capable of being fabricated and tested in the real world. Additionally, in the literature, there had been no results where a large distribution of scatterers on a two-dimensional plane were optimized to produce a fully three-dimensional intensity profile in the far field. Lastly, no previous inverse-design methods were capable of handling a large array of wavelength-scale scatterers.

5.2 Optimization Method

The inverse-design method used in this chapter is the same as the method described in Chapter 4.. The general formalisms remain the same and the same forward and adjoint problems are solved. However, in Chapter 4 the FOM was specified to only be the maximization of the intensity at a single point in space. In this chapter, we are interested in the optimization of the intensity at multiple points in a three-dimensional space, and we specify a new FOM to encapsulate this new function.

5.2.1 Figure of merit

To capture the desired result of having multiple points, we decide to use a sum of squares FOM based on the desired intensity profile:

$$FOM(\mathbf{R}) = \sum_j (I_0(\mathbf{r}_j) - I_k(\mathbf{r}_j, \mathbf{R}))^2 \tag{5.1}$$

where I_0 is the desired intensity profile, I_k is the iterate intensity profile for iteration k of the optimization process, $\mathbf{R}$ is the set of radii we are optimizing over, and $\mathbf{r}_j$ are the spatial locations of the points of the image we are interested in. For this demonstration, we define I_0 as 22 different points, 8 which constitute the desired image points where the intensity is chosen to be a nonzero value (25), and 14 which serve as regularization points where the intensity is chosen to be zero. These regularization points are chosen to be zero at the locations of the previous and next focal spots of a given transverse plane along the optical axis. A graphical layout of the FOM is shown in Figure 5.1a.

Specifically, each focal spot is located in a distinct transverse focal plane, separated along the optical axis by 28 μm (57 μm) and is arranged on a circle of radius 12 μm (20 μm) for the 1.55 μm (3 μm) device.

To solve the adjoint system of equations, we need to find the derivative of this figure of merit with respect to the scattered field coefficients b_n^i:

$$\frac{\partial FOM}{\partial b_n^i} = -2 \sum_j (I_0(\mathbf{r}_j) - I_k(\mathbf{r}_j)) \mathbf{E}^*(\mathbf{r}_j) \cdot \mathbf{\Psi}_n^{(3)}(\mathbf{r}_j - \mathbf{r}_i). \tag{5.2}$$

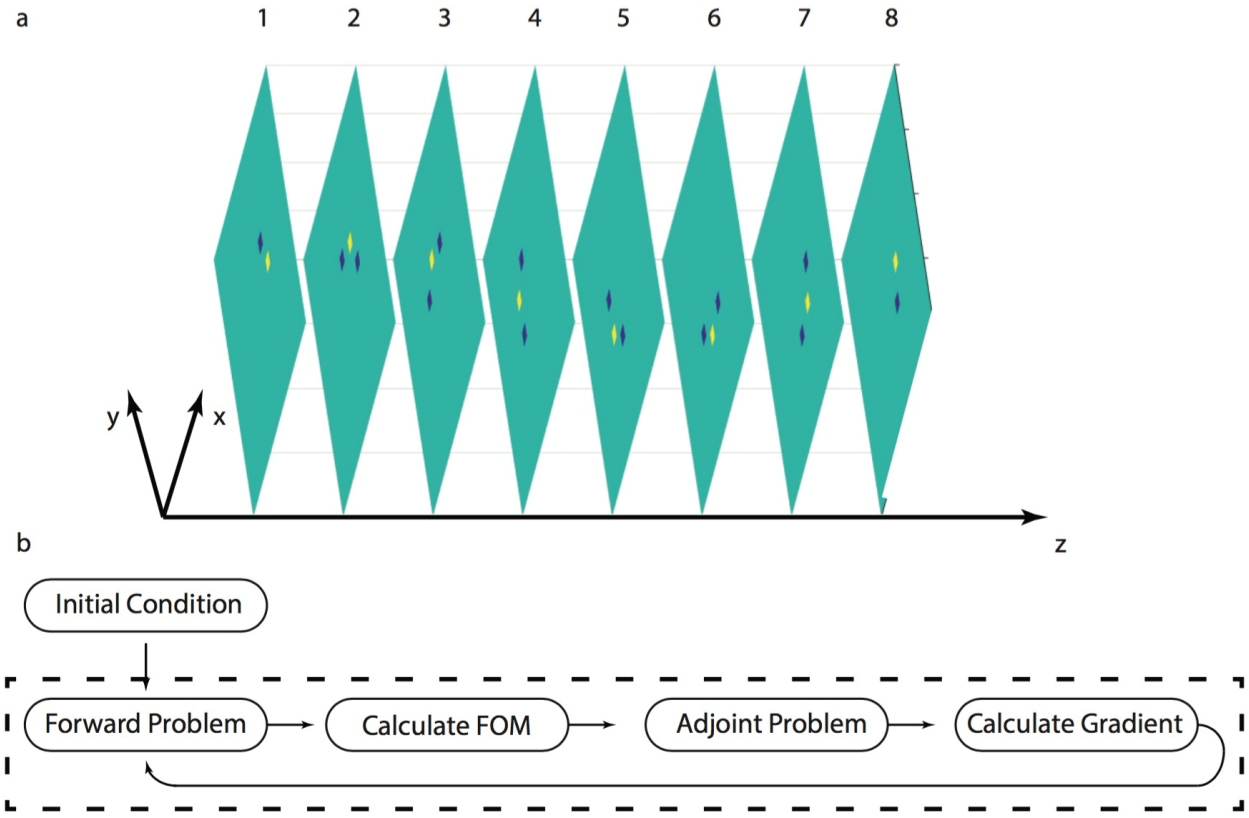

Figure 5.1: Figure showing the optimization scheme with (a) as the specification of the discrete helix figure of merit. The yellow points denote locations where the helix is specified with non-zero intensity, and blue points are locations where the helix is regularized with zero intensity. The helix is produced on 8 transverse planes along the optical (z) axis. (b) is the optimization flow for the progression of the algorithm. The steps in the dashed box constitute a single iteration.

5.2.2 Gradient update

In the Chapter 4, we used a normalized gradient descent with a fixed step size, and a fixed iteration number. While this approach led to reasonable results for a relatively simple FOM, namely that of maximizing intensity at a single point, it did not converge reliably for a more complex FOM. To remedy this, we used L-BFGS-B, a well known and standard gradient update technique that includes an adaptive step size using both a trust region method and a memory register. Using L-BFGS-B, our method converged much more reliably to a device with satisfactory performance. Besides the change in the gradient update, the underlying method remains the same and the same forward and adjoint problems are solved as shown in Figure 5.1b.

5.2.3 Optimization numerics

In addition to the choice of the gradient update, we must choose numerics with which to run the simulation. The numerical values for the initial condition, maximum expansion number, and numerical accuracy are shown in Table 5.1. The numerical accuracy is residual that represents the precision to which we solve our linear system of equations.

As GLMT expands the initial and scattered fields in an infinite basis of SVWFs, we need to introduce a suitable cutoff for the angular momentum expansion l_{max} determined by the dimension and refractive index of the scatterer relative to the incident wavelength. This number determines the maximum number of expansion modes n_{max} required to accurately characterize a scatterer and is given by:

$$n_{max} = 2l_{max}p(l_{max} + 2), \tag{5.3}$$

where p specifies the polarization. In general, the scatterers with larger physical dimensions and refractive index contrasts require higher expansion orders to accurately characterize. In this chapter, the 1.55 μm device (3 μm) device required a cutoff of $l_{max} = 4$ ($l_{max} = 3$). These parameters are visualized in Figure 5.2.

Table 5.1: Optimization numerics

Wavelength	1.55 μm	3 μm
Initial radius	700 nm	1200 nm
Total spheres	3600	4900
Min, Max radius	$250, 1200$ nm	$250, 1400$ nm
l_{max}, n_{max}	$4, 48$	$3, 30$
Periodicity	2.42 μm	2.9 μm
Device width	144 μm	200 μm
Initial, Final FOM	$2800, 0.095$	$4900, 1.9$
Numerical accuracy	1×10^{-3}	1×10^{-3}

As before, the forward and adjoint systems of equations are solved by a BiCGSTAB iterative solver with a blockdiagonal preconditioner.

5.3 Results

The optimization method converged to an asymmetric distribution of spheres shown in Figure 5.4a. This distribution of spheres is clearly unintuitive, and does not correspond to an ordered distribution. To test our device, we used two separate microscopes for the two wavelengths. The 1.55 μm device is presented in Section 5.3, and the 3 μm device is presented later in Section 5.5. In simulation, we see eight clear and distinct focal spots with high contrast relative to their background that are located where we specified them in the design as shown in Figure 5.3. The simulation results confirm the satisfaction of our figure of merit, and the performance of the device to the designed specifications.

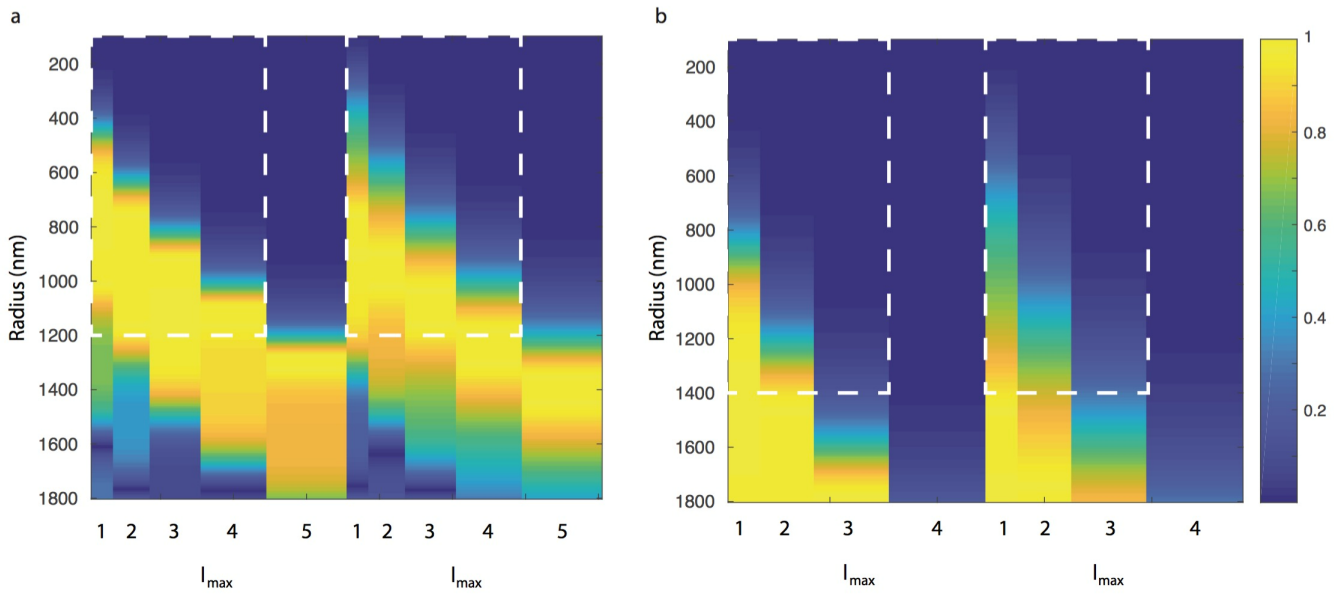

Figure 5.2: Absolute value of the Mie coefficients for the sphere radii used in the device designed for (a) 1.55 μm, and (b) 3 μm. Dashed white boxes show the cutoffs.

5.3.1 Fabrication

In order to fabricate the spherical scatterers with reasonable fidelity, we used the Nanoscribe GT two-photon lithography system at the Washington Nanofabrication Facility. The Nanoscribe has been shown to be capable of fabricating high quality refractive optics with curved surfaces [108, 109] with its voxel size of 200 nm ×200 nm ×700 nm along x, y, and z make it a reasonable choice for use in fabricating the spheres we are interested in. The spheres are fabricated using the 63× objective and the IP Dip resist with $n = 1.47$ for the highest possible resolution. The fabrication is described in Appendix A.2.

The final fabrication of the 1.55 μm device is shown in Figures 5.4b-d. We can see that the final distribution is reasonably accurate when compared to the design, and the two insets with a top-down and angled view show the single scatterers. The scatterers are not perfectly spherical, but the dimensions are reasonably consistent with the design. The fabrication

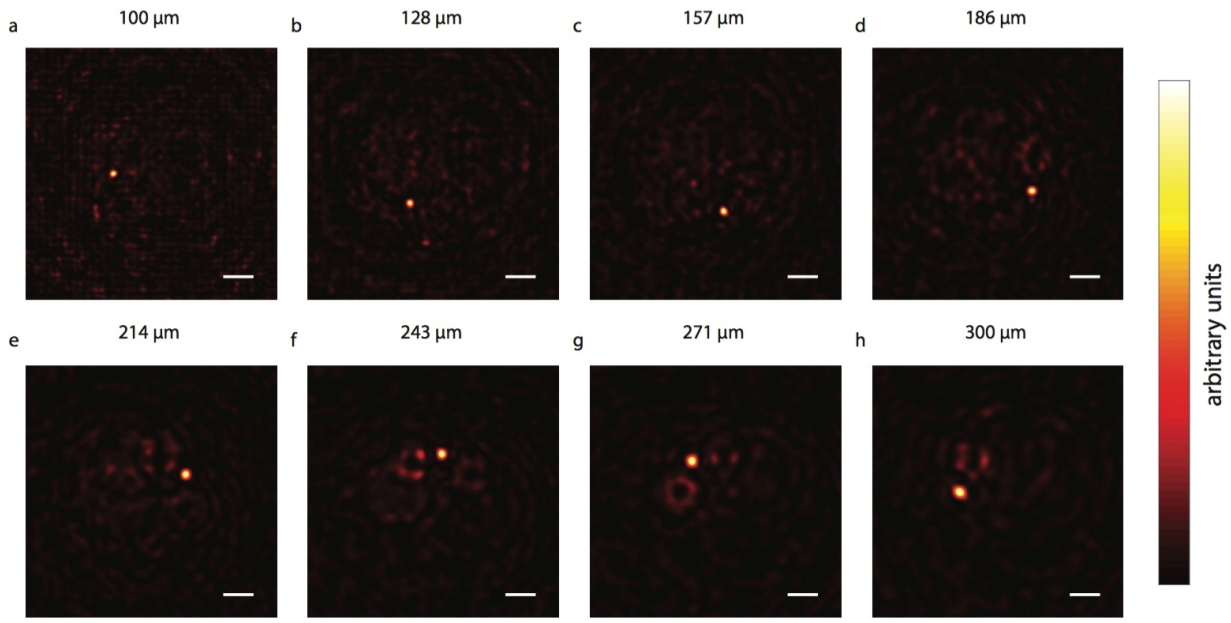

Figure 5.3: Simulated device performance (a)-(h) are images of the intensity profiles produced at the specific distances from the device showing the focal spot rotate around the x-y plane as the element is defocused. Solid white scale bar is 10 µm, and the window size is 80 µm $\times$80 µm. The color bar is a linear scale.

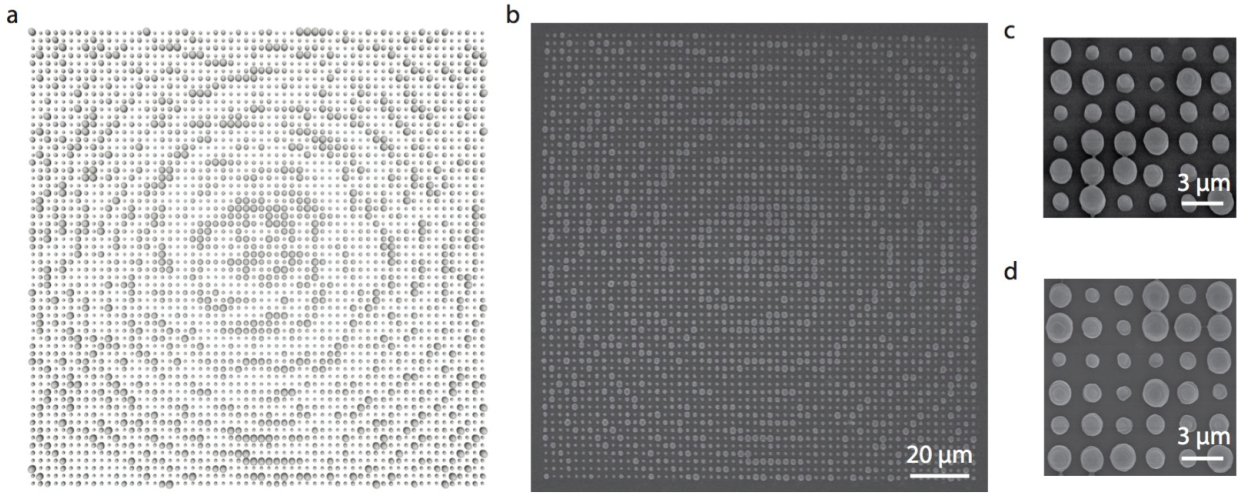

Figure 5.4: Schematic (a) and SEMs of the 1.55 μm device (b)-(d). (b) is a top down view of the entire device. (c) and (d) are zoomed in SEMs showing the fabrication imperfections from an angled and top down view respectively. All SEMs are of a gold coated device.

imperfections and the addition of a substrate are not accounted for in our simulation and optimization process, though in Chapter 4 we found only a small effect from the substrate.

5.3.2 Performance

The device was measured using a Santec TSL-510 centered at 1.55 μm emitting 15 mW continuous wave. The light is incident normal to the device, and is collected by a microscope with a movable objective. The microscope consists of an infinity corrected 40× Nikon Plan Fluor and a 20 cm focal length tube lens. The detector is a Xenics Bobcat-6583 infrared camera with a 320 × 256-pixel array and the camera exposure time was set to 10 μs.

In experiment, the eight clear focal spots are produced quantitatively matching the locations shown in the simulation. However, when compared to the simulation, the experiment shows a noticeably lower contrast between the focal spot and the background. In addition, in Figures 5.5a, b, and f we can identify smaller hot spots of significant intensity that are

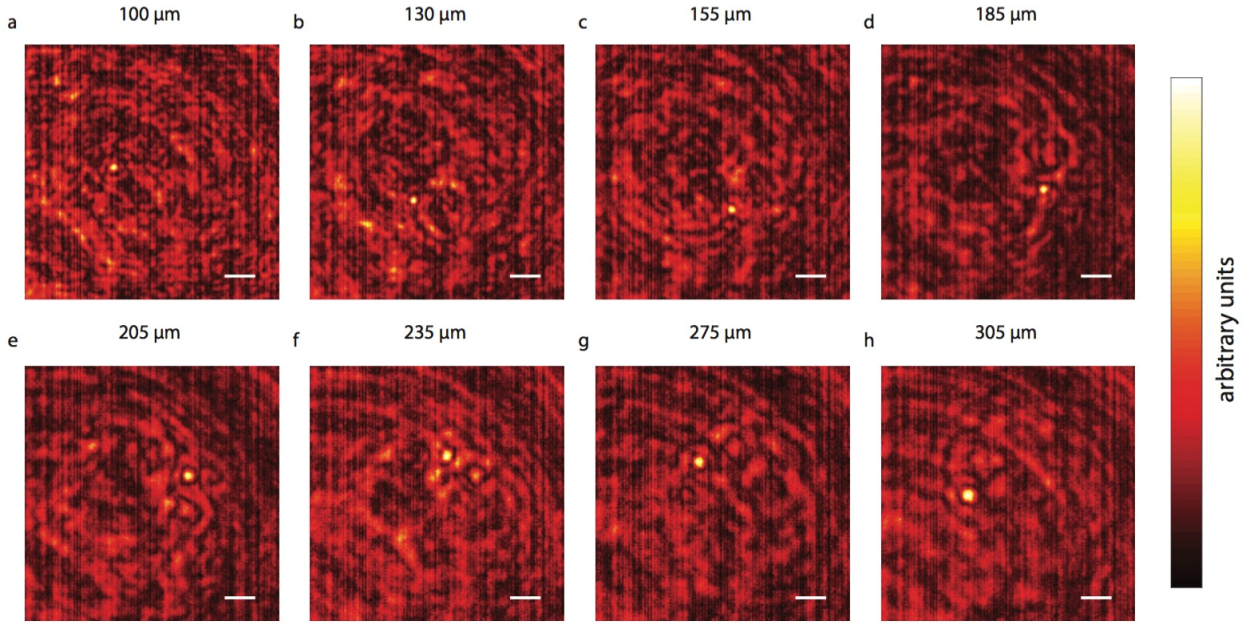

Figure 5.5: Experimental device performance (a)-(h) are images of the intensity profiles produced at the specific distances from the device showing the focal spot rotate around the x-y plane as the element is defocused. Solid white scale bar is 10 µm, and the window size is 80 µm ×80 µm. Images can be directly compared to the simulation results in Figure 5.3. The color bar is a linear scale.

not present in simulation. The actual focal spots are produced in the correct spatial locations in plane, but there is a slight offset between the expected focal spot along the optical axis for the spots shown in Figures 5.5e and f. We attribute these discrepancies between the simulation and experiment primarily to fabrication errors, which we will show have a significant effect on the device performance. Both the experimental and simulation results show a gradual increase in focal spot size with increasing focal plane distance, as we did not control for this quantity in our regularization.

We compared the in-plane locations of the focal spots between the simulation and experimental results. The simulated (red) spots shown in Figure 5.6a lie on the dashed black

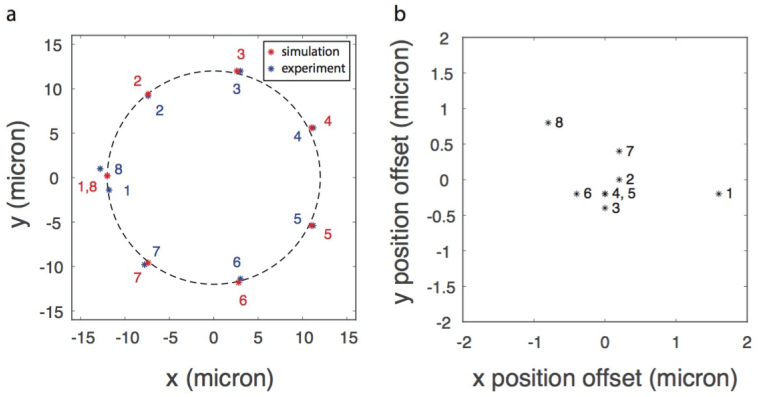

Figure 5.6: Comparison between experiment and simulation showing (a) the simulated focal spot locations relative to the experimental positions based on the location of maximum intensity. Simulated (experimental) data are plotted in red (blue). Dashed black line is a circle with radius 12 μm serving as an eye guide. (b) is the relative positional error of each of the focal spots. Numbers correspond to the order in which spots appear with 1 being the closest focal plane to the device (100 μm) and 8 being the furthest (300 μm)

circle with radius 12 μm. The experimental (blue) spots largely trace out the same shape and qualitatively behave according to the defined FOM. However, there are some deviations from the simulated spots, e.g. the first and last spot do not lie perfectly on top of each other. The position differences between the simulated and experimentally measured focal spots are shown in Figure 5.6b. These discrepancies can be attributed to an amount of alignment error during optical characterization in addition to the known fabrication imperfections.

5.4 Effects of Fabrication Quality

We attribute the difference between experimental and simulated performance largely to fabrication quality due to the performance of our initial fabricated devices. In this section we will present an initial device with more pronounced fabrication imperfections as shown in Figure 5.7. In comparison with Figure 5.4, we can see that the scatterers are noticeably

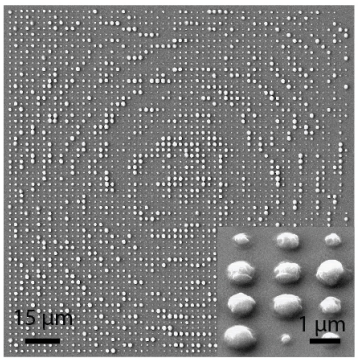

Figure 5.7: SEM of a previous fabrication run coated in gold. Top-down view of the entire device, with inset showing noticeable asymmetry in the spherical scatterers

rougher, and less spherically shaped, and this has a concrete effect on the experimental performance shown in Figure 5.8. The experimental data for this device shows less contrast than the device presented in Figure 5.5. Noticeably, the focal spots in Figures 5.8a-c are hard to discern due to both the low contrast and also the presence of numerous hot spots. The later focal spots are more clearly discernable, and more similar to the simulated result, though they do appear at different values of defocus. When compared to the simulation results in Figure 5.9 (same data as Figure 5.3, different colorbar), the contrast is clearly lower, though the spots show up in the same qualitative locations.

To be able to compare the experimental and simulated results directly, we extract the positions of the focal spots from the simulated data, and search those locations in the experimental data in an 8 µm ×8 µm window as shown in Figure 5.10. Within the window, we take the focal spot to be the point of maximum intensity. This data is then used to compare with the locations of the maximums as shown in Figure 5.11. Relative to the previously presented experimental data in Section 5.3, it is clear that improved fabrication both increased the contrast of the closer focal spots and the accuracy of the focal spot location.

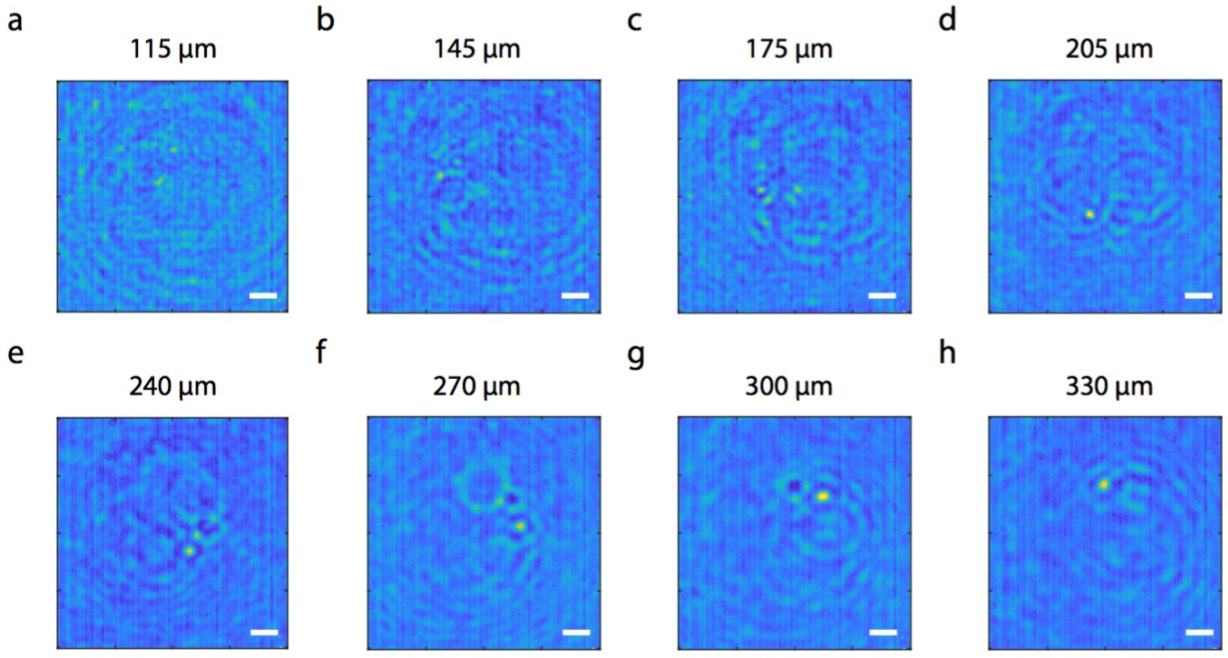

Figure 5.8: Experimental device performance of an initial device. (a)-(h) are images of the intensity profile produced at specific distances from the device showing the focal spot rotating in the x-y plane. Solid white scale bar is 10 µm. The color bar is a linear scale.

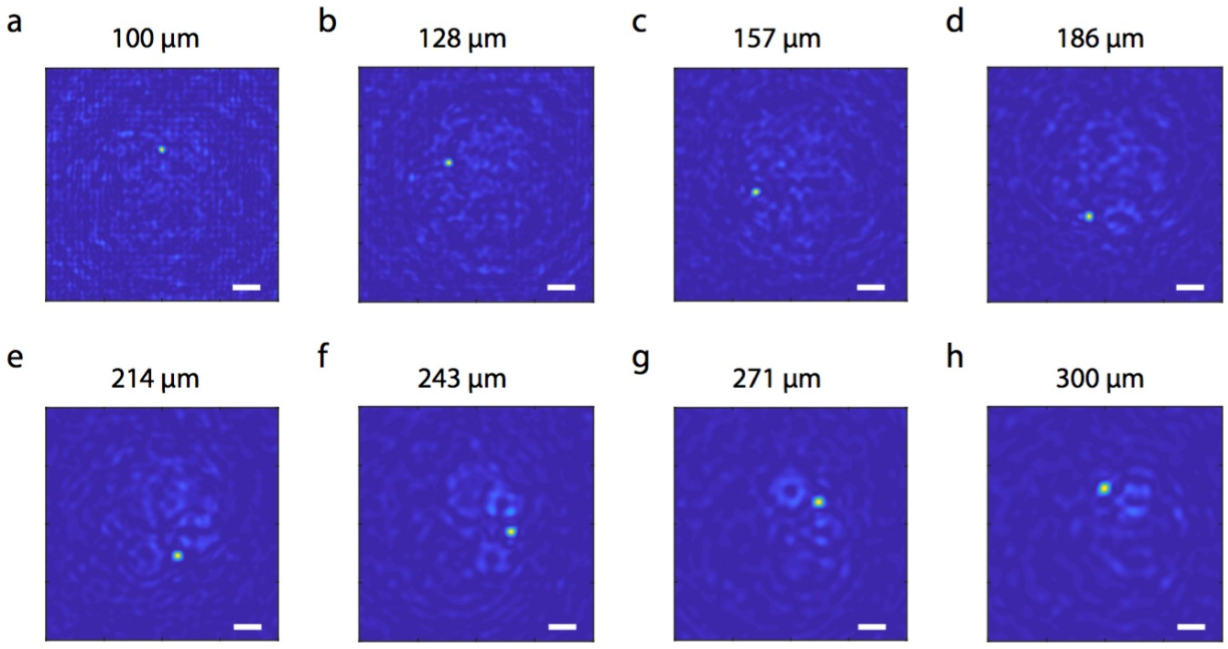

Figure 5.9: Simulated device performance of an initial device. This is the same data as Figure 5.3 with a different colorbar for ease of comparison. (a)-(h) are images of the intensity profile produced at specific distances from the device showing the focal spot rotating in the x-y plane. Solid white scale bar is 10 µm.

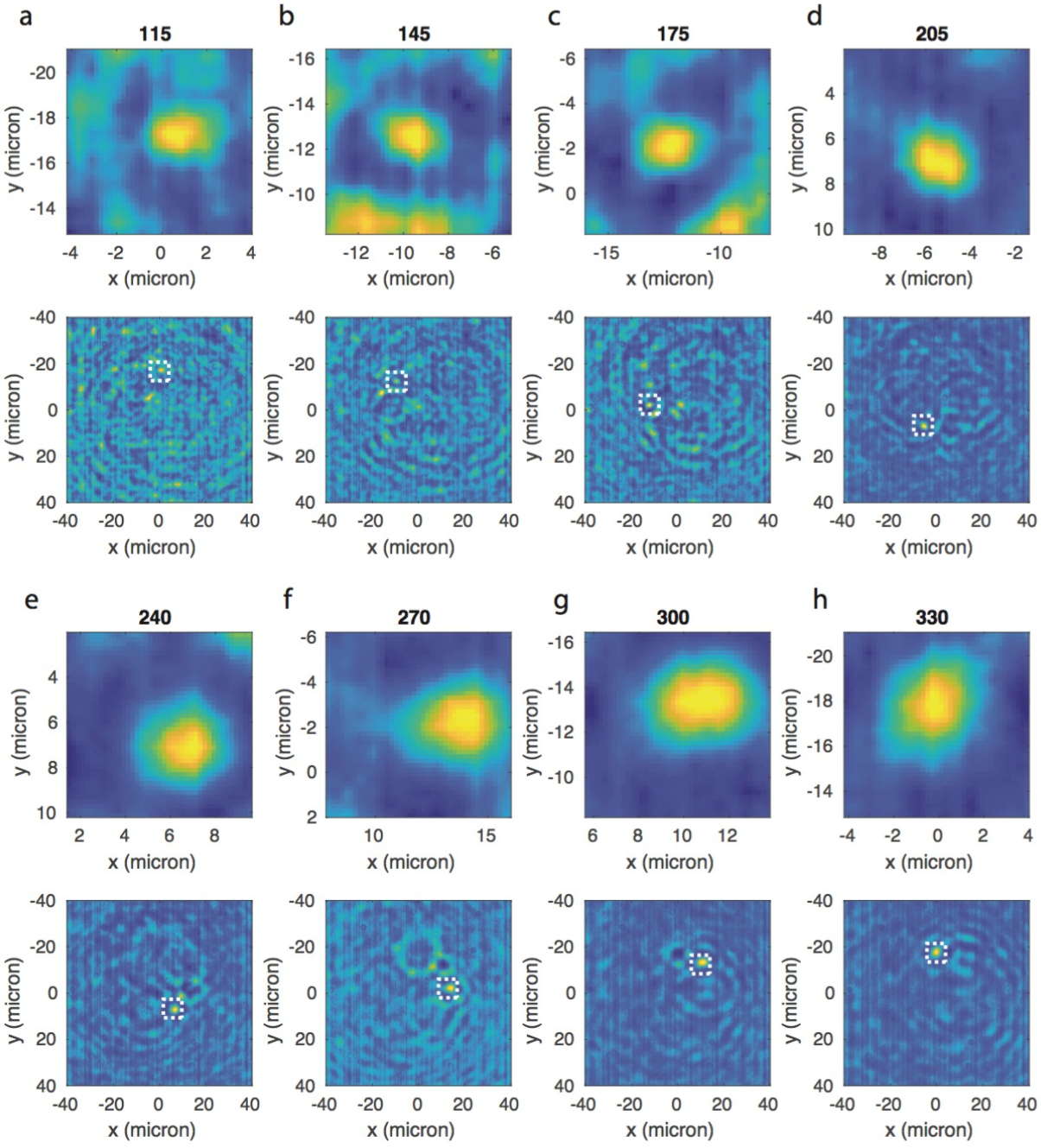

Figure 5.10: Extracted experimental focal spots and locations based on simulation data. (a)-(h) exracted focal spot profiles (top) and their locations in the x-y plane (bottom). The white dashed box has dimensions of 8 μm ×8 μm and represents where the focal spot profiles are.

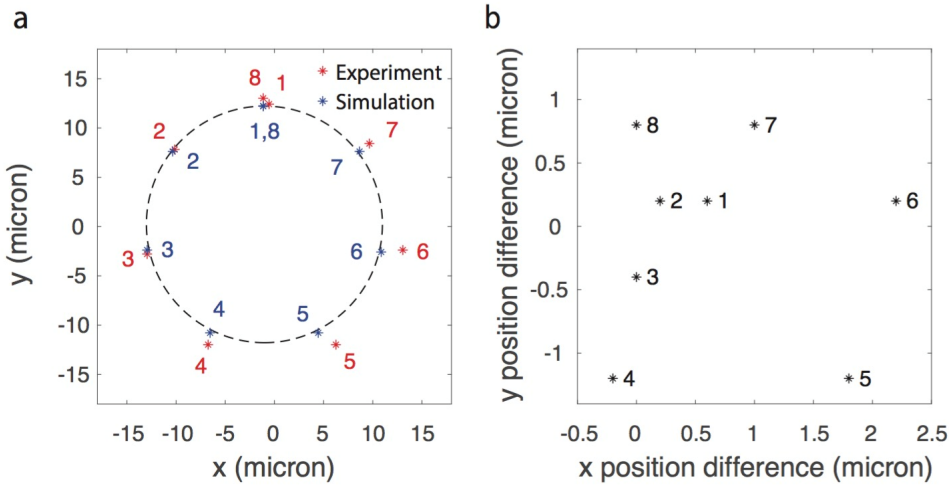

Figure 5.11: In-plane focal spot comparison of an initial device. (a) Focal spot locations of the experimental and simulated focal spots are shown in red and blue respectively. (b) Difference between expected location based on simulation, and actual location of the focal spot in experiment.

5.5 3 Micron Device

In addition to the 1.55 μm device, we also designed and fabricated a similar device for operation at 3 μm. While the 1.55 μm device has a super-wavelength periodicity, the 3 μm device has a sub-wavelength periodicity, qualifying it as a metasurface. The same experiment for measuring the helical focal spots is proposed for this device, and this device was tested by collaborators at the Air Force Research Labs.

5.5.1 Simulation

The simulated performance of the device shown in Figure 5.12 shows a clear focal spot in the design locations. However, when compared to the focal spots shown in Figure 5.3, the 3 μm device simulations shown in Figure 5.13 show clearly higher background. The final optimization result had a higher (worse) figure of merit than that of the previous 1.55 μm device, leading us to expect decreased performance.

5.5.2 Fabrication

The final fabricated device from the optimization process is shown in Figure 5.14. Again we see that the scatterers are arranged in an unintuitive manner. The inset shows the fabrication quality of the individual spherical scatterers. In this case, the scatterers show noticeable asymmetry in their design and are clearly not entirely spherical in shape.

5.5.3 Results

The mid-wave infrared (MWIR) idler of a Ti-sapphire pumped optical parametric oscillator (OPO), M Squared Firefly IR, was used to illuminate the metalens at normal incidence. A 0.56 NA GeSbSe anti-reflective coated infrared aspherical lens (effective focal length = 4 mm, working distance = 3.05 mm) was translated in steps of 0.1 μm along the optical axis behind the metasurface. The focal spots of the metasurface at $\lambda = 3$ μm were imaged directly onto an InSb 640 × 512 pixel focal plane array (FPA), FLIR SC6700, with a 15 μm pitch cooled

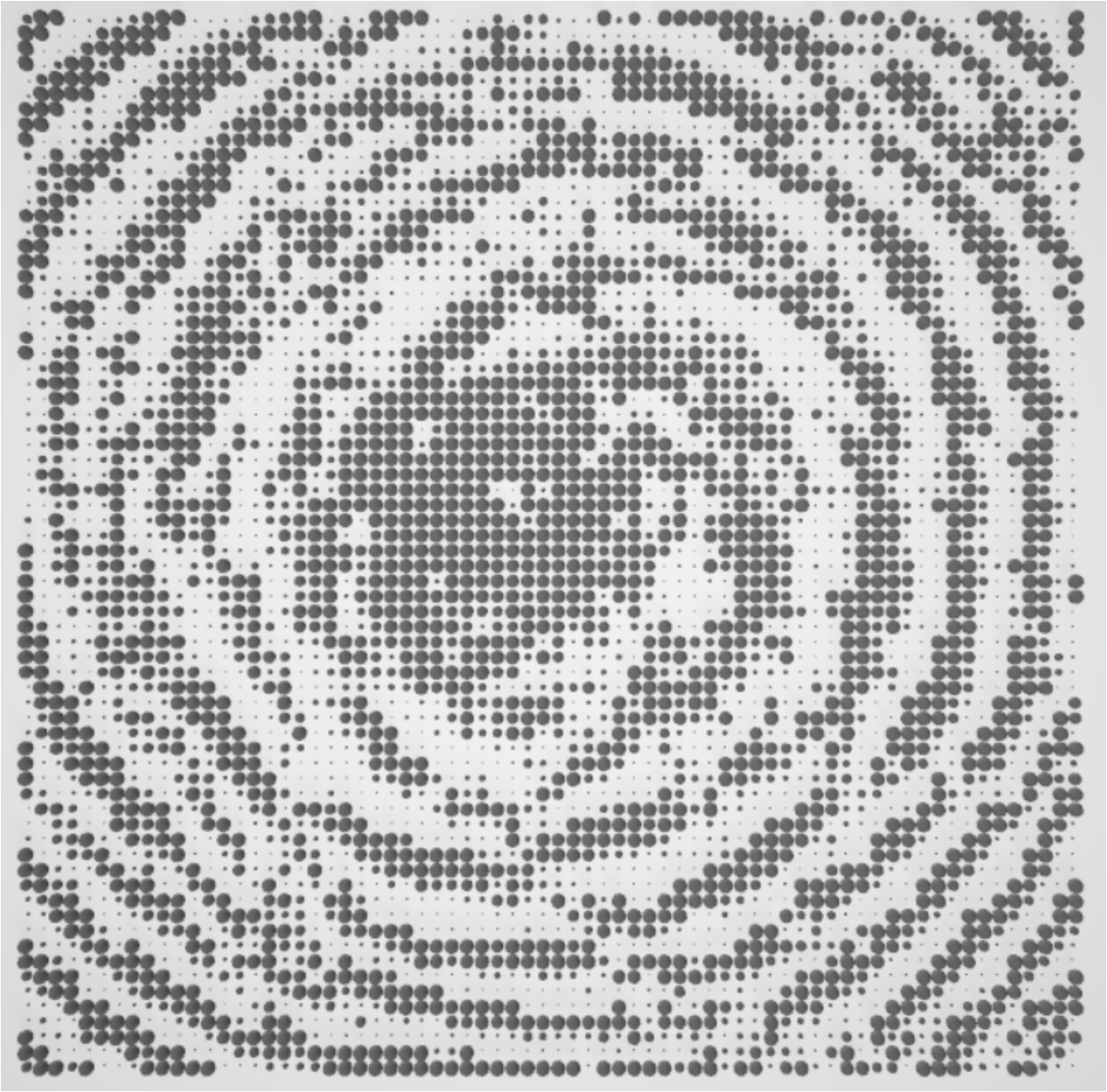

Figure 5.12: 3 μm device scheme. The device has dimensions 200 μm × 200 μm.

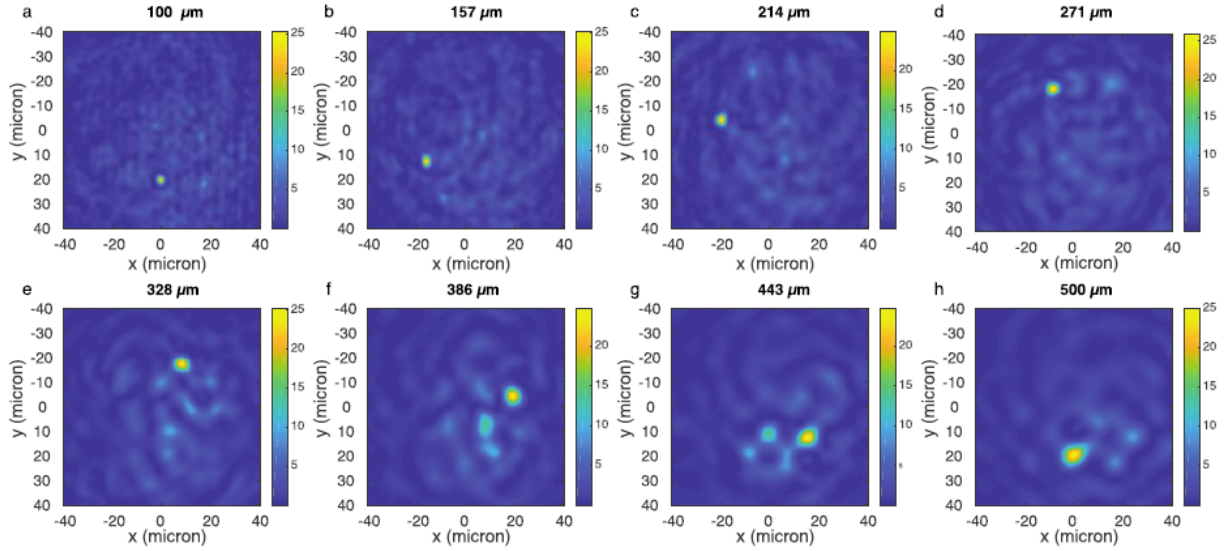

Figure 5.13: 3 μm simulated device performance. (a)-(h) Images of the intensity profile produced at specific focal planes located at distances from the device surface showing the focal spot rotating in the x-y plane.

to 76K. This optical setup gives a magnification of about 56.2×. The exposure time of the camera was set to 0.9 ms and integrates 135 pulses from the 150.6 kHz (< 10 ns pulses, 105 mW average power) from the OPO per frame. To maximize the 14-bit dynamic range of the FPA an ND1 filter is used to attenuate the light prior to the metasurface.

The fabricated device performed relatively poorly in experiment. While there are focal spots that are identifiable producing a helical pattern, many of the simulated focal spots fail to appear, and also the contrast between the design focal spot and the other hot spots is relatively low. We were not able to identify the correct locations of all the focal spots in the experiment. We attribute this discrepancy to a degree of fabrication error, and the contamination of the device by a noticeable dust particle visible in Figure 5.15e. In addition, we note that the design of this device had higher backgrounds and lower performance as shown by the simulated performance in Figure 5.13.

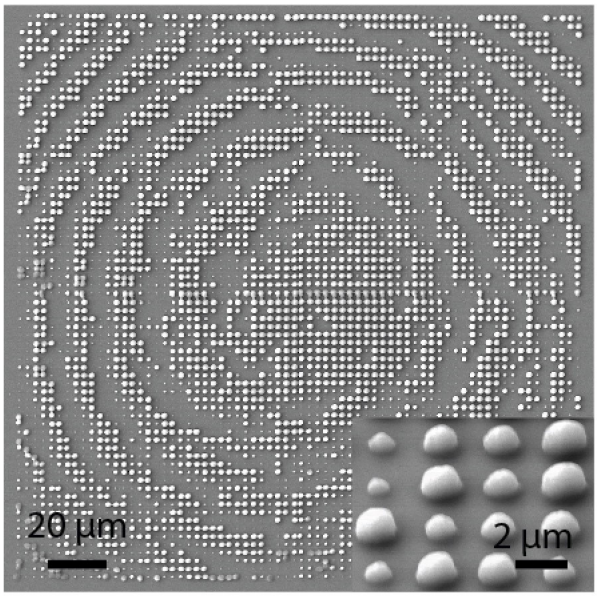

Figure 5.14: Scanning electron micrograph of final device produced by the optimization algorithm showing a top down view of the entire device, and a zoom in picture showing the fabrication quality of individual spheres.

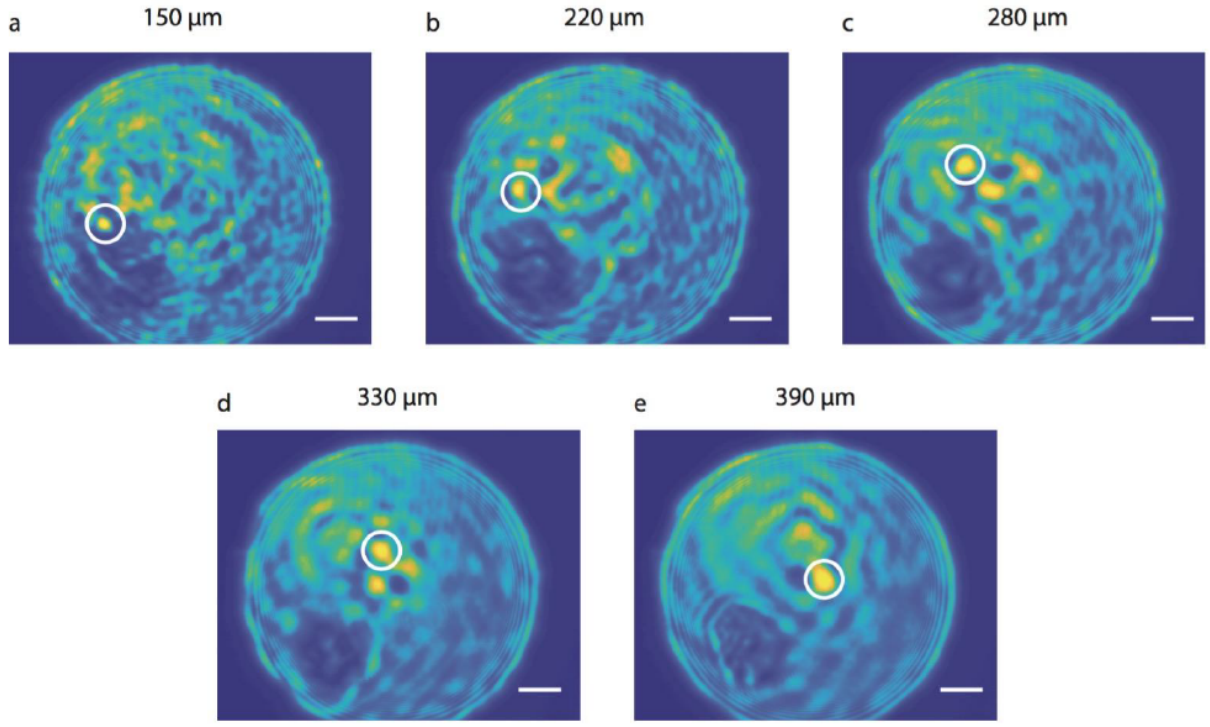

Figure 5.15: 3 µm experimental device performance. Shows five focal spots ranging in distances from 150 µm to 390 µm. Scale bar is 5 µm.

5.6 Machine Specifications and Software

The forward simulation is a branch of the freely available CELES software [103]. The inverse simulation is a custom written extension to CELES. The specification of the hardware and software used in this paper are as follows:

- AMD Ryzen Threadripper 1920x
- NVIDIA Titan Xp 12 GB
- 64 GB DDR4
- CentOS 7
- Matlab 2017b
- CUDA 8.0

5.7 Conclusion

In conclusion, we experimentally demonstrated an electromagnetic inverse-design method capable of handling large area arrays of discrete, dielectric, spherical scatterers. The design method efficiently takes advantage of the large number of degrees of freedom available in these large arrays of scatterers and is able to tune individual scatterer properties to optimize their performance. We use the presented inverse-design method to create a new optical element capable of focusing an incident beam of light into eight focal spots arranged on a discrete, helical pattern. This demonstrated optical element has no analogue in traditional optics and is impractical to design via intuition. While this method is restricted to spherical scatterers, this method can be readily extended to scatterers with different geometries by extending it using the T-matrix method. This work is a step towards enabling a flexible model of 'designer' optics where optical elements can be exquisitely tailored to specific, user-designed functionalities.

Chapter 6

INVERSE DESIGN BASED ON THE T-MATRIX METHOD

In this chapter, we introduce an extension of GLMT to particles of arbitrary sized ellipsoidal particles using the T-matrix method (TMM). The TMM is a natural extension to GLMT using the same coordinate system and basis functions. We present a brief introduction to the idea of the TMM, and present the computation of the T-matrix for an ellipsoidal particle. Then, we derive the expressions used to compute the derivative of the T-matrix of the ellipsoid with respect to the principle axes, and the orientation in terms of four surface integrals. Finally, we present numerical verification of the derivative.

6.1 Motivation

The previous two chapters have been focused on a gradient-based inverse-design method using GLMT focused on optimizing arrays of spherical scatterers toward performing a specific optical function defined by a figure of merit. While this method is capable of simulating and then optimizing large arrays, its application is limited to spherical scatterers. The restriction to spherical scatterers presents two major limitations on the applicability of the method. First, spheres are very difficult to fabricate using conventional lithography processes, and in chapter 4, we used two-photon lithography to circumvent this. Although this resulted in a reasonably high-performance device, the low refractive index of the resist, and the low aspect ratios limit further experiments. Second, while spheres are electromagnetically simple, this also means that they offer fewer degrees of freedom to tune and optimize. In particular, spheres are not ideal for use in polarization optics, as the spherical scatterer itself behaves identically for different polarizations. The TMM is a straightforward extension of GMMT to particles of arbitrary geometries such as ellipsoids and cylinders that extends the inverse-

design method to a larger design space, and also better experimental demonstrations.

6.2 The T-Matrix Method

The T-matrix characterizes the scattering properties of a particle in spherical coordinates. It depends only on the geometric and material properties of particle itself, the medium surrounding the particle, and the wavelength of excitation. In the previous section, the T-matrices of the spheres were diagonal matrices, and easily calculated using closed form expressions. The T-matrix of the ellipsoid requires the computation of the Q and RgQ matrices that represent the coupling between the scattered field and the incident field to the surface fields respectively [110, 111]. The T-matrix is then given by [110–112]:

$$T = RgQ(Q)^{-1} \tag{6.1}$$

The Q matrix is composed of four square submatrices $\bar{P}$, $\bar{R}$, $\bar{S}$, and $\bar{U}$, given by:

$$Q = \begin{bmatrix} \bar{P} & \bar{R} \\ \bar{S} & \bar{U} \end{bmatrix}, \tag{6.2}$$

and these individual square matrices are given as in [113]:

$$\bar{P}_{lml'm'} = -ikk_s J^{(21)}_{lml'm'} - ik^2 J^{(12)}_{lml'm'}, \tag{6.3}$$

$$\bar{R}_{lml'm'} = -ikk_s J^{(11)}_{lml'm'} - ik^2 J^{(22)}_{lml'm'}, \tag{6.4}$$

$$\bar{S}_{lml'm'} = -ikk_s J^{(22)}_{lml'm'} - ik^2 J^{(11)}_{lml'm'}, \tag{6.5}$$

$$\bar{U}_{lml'm'} = -ikk_s J^{(12)}_{lml'm'} - ik^2 J^{(21)}_{lml'm'}, \tag{6.6}$$

where the J terms represent surface integrals over the surface of the particle, and the individual terms are given by:

$$J^{(11)}_{lml'm'} = (-1)^m \int_S dS\hat{n}(\mathbf{r}) \cdot \mathbf{\Psi}^{(1)}_{1,l',m'}(k_s r, \theta, \phi) \times \mathbf{\Psi}^{(3)}_{1,l,-m}(kr, \theta, \phi), \tag{6.7}$$

$$J^{(12)}_{lml'm'} = (-1)^m \int_S dS\hat{n}(\mathbf{r}) \cdot \mathbf{\Psi}^{(1)}_{1,l',m'}(k_s r, \theta, \phi) \times \mathbf{\Psi}^{(3)}_{2,l,-m}(kr, \theta, \phi), \tag{6.8}$$

$$J^{(21)}_{lml'm'} = (-1)^m \int_S dS\hat{n}(\mathbf{r}) \cdot \mathbf{\Psi}^{(1)}_{2,l',m'}(k_s r, \theta, \phi) \times \mathbf{\Psi}^{(3)}_{1,l,-m}(kr, \theta, \phi), \tag{6.9}$$

$$J^{(22)}_{lml'm'} = (-1)^m \int_S dS\hat{n}(\mathbf{r}) \cdot \mathbf{\Psi}^{(1)}_{2,l',m'}(k_s r, \theta, \phi) \times \mathbf{\Psi}^{(3)}_{2,l,-m}(kr, \theta, \phi), \tag{6.10}$$

where S is the surface bounding the particle, dS is some infinitesimal area on the surface S, and $\hat{n}$ is a outward pointing unit normal at dS. We are also using spherical vector wave functions $\mathbf{\Psi}^{(1)}$ and $\mathbf{\Psi}^{(3)}$ which are again [111]:

$$\mathbf{\Psi}^{(\nu)}_{1lm}(\mathbf{r}) = \frac{e^{im\phi}}{\sqrt{2l(l+1)}} b_l(kr)\big[im\pi_{lm}(\theta)\hat{\theta} - \tau_{lm}(\theta)\hat{\phi}\big], \tag{6.11}$$

$$\begin{aligned}\mathbf{\Psi}^{(\nu)}_{2lm}(\mathbf{r}) =& \frac{e^{im\phi}}{\sqrt{2l(l+1)}} \Bigg\{ l(l+1)\frac{b_l(kr)}{kr} P_l^{|m|}(cos\theta)\hat{r} \\ &+ \frac{1}{kr}\frac{\partial(krb_l(kr))}{\partial(kr)}\big[\tau_{lm}(\theta)\hat{\theta} + im\pi_{lm}(\theta)\hat{\phi}\big] \Bigg\},\end{aligned} \tag{6.12}$$

where we have defined:

$$\pi_{lm}(\theta) = \frac{P_l^{|m|}(cos\theta)}{sin\theta}, \tag{6.13}$$

$$\tau_{lm}(\theta) = \frac{\partial P_l^{|m|}(cos\theta)}{\partial\theta}. \tag{6.14}$$

$P_l^m(x)$ is the associated Legendre polynomial. j_l is the spherical Bessel function of order l, and b_l is either a spherical Bessel function (j_l) for $\nu = 1$ or spherical Hankel function of the first kind ($h_l^{(1)}$) of order l for $\nu = 3$, depending on whether RgQ or Q is being computed, respectively.

In spherical coordinates, the product of the unit normal and the infinitesmal area is:

$$dS\hat{n}(\mathbf{r}) = r^2 sin(\theta)\sigma(\mathbf{r})d\theta d\phi, \tag{6.15}$$

and σ is given by:

$$\sigma(\mathbf{r}) = \hat{r} - \hat{\theta}\frac{1}{r}\frac{\partial r}{\partial\theta} - \hat{\phi}\frac{1}{rsin\theta}\frac{\partial r}{\partial\theta}. \tag{6.16}$$

In this case, r is parameterizing the surface of a particle, and for an ellipsoid in spherical coordinates, r is given by:

$$r(\theta,\phi) = \left[sin^2\theta\left(\frac{cos^2\phi}{a^2} + \frac{sin^2\phi}{b^2}\right) + \frac{cos^2\theta}{c^2}\right]^{-1/2} \tag{6.17}$$

To compute RgQ rather than Q, we simply need to replace $\mathbf{\Psi}^{(3)}$ in the J integrals with $\mathbf{\Psi}^{(1)}$.

6.3 Computing T-Matrix Derivatives

Now to take a derivative of the T-matrix of this particle with respect to some parameter p, we find that:

$$\frac{\partial T}{\partial p} = \left(\frac{\partial RgQ}{\partial p} - T \frac{\partial Q}{\partial p} \right) Q^{-1}, \tag{6.18}$$

where we must now find the derivatives of the submatrices $\bar{P}$, $\bar{R}$, $\bar{S}$, and $\bar{U}$ with respect to p. These are given by:

$$\frac{\partial \bar{P}_{lml'm'}}{\partial p} = -ikk_s \frac{\partial J^{(21)}_{lml'm'}}{\partial p} - ik^2 \frac{\partial J^{(12)}_{lml'm'}}{\partial p}, \tag{6.19}$$

$$\frac{\partial \bar{R}_{lml'm'}}{\partial p} = -ikk_s \frac{\partial J^{(11)}_{lml'm'}}{\partial p} - ik^2 \frac{\partial J^{(22)}_{lml'm'}}{\partial p}, \tag{6.20}$$

$$\frac{\partial \bar{S}_{lml'm'}}{\partial p} = -ikk_s \frac{\partial J^{(22)}_{lml'm'}}{\partial p} - ik^2 \frac{\partial J^{(11)}_{lml'm'}}{\partial p}, \tag{6.21}$$

$$\frac{\partial \bar{U}_{lml'm'}}{\partial p} = -ikk_s \frac{\partial J^{(12)}_{lml'm'}}{\partial p} - ik^2 \frac{\partial J^{(21)}_{lml'm'}}{\partial p}. \tag{6.22}$$

This requires us to take the derivatives of the surface integrals J with respect to the parameter p. In general, our parameter of interest p will be some geometric quantity that determines the shape of the surface of integration S. In the specific case of ellipsoidal scatterers, they will be the three independent axes a, b, and c along the x, y, and z axes respectively.

The expressions for the derivatives with respect to a spatial variable (a, b, c) are as follows where p represents any of the ellipsoid axes:

$$\begin{aligned} \frac{\partial J^{(11)}_{lml'm'}}{\partial p} = &- i \iint \alpha_{lml'm'} \left(m' \pi_{l'm'} \tau_{lm} + m \pi_{lm} \tau_{l'm'} \right) \\ &\left[r \left(k \frac{\partial b_l}{\partial p} j_{l'} + k_s b_l \frac{\partial j_{l'}}{\partial p} \right) + 2 b_l j_{l'} \right] r sin\theta d\theta d\phi, \end{aligned} \tag{6.23}$$

$$\begin{aligned} \frac{\partial J^{(12)}_{lml'm'}}{\partial p} = \iint \alpha_{lml'm'} \Bigg\{ &\left[\frac{\partial R^{(12)}_{lml'm'}}{\partial r} + (\Theta^{(12)}_{lml'm'} E_\theta + \Phi^{(12)}_{lml'm'} E_\phi) \frac{\partial \rho_{l,l'}}{\partial r} \right] \frac{\partial r}{\partial p} \\ &+ \left(\Theta^{(12)}_{lml'm'} \frac{\partial E_\theta}{\partial p} + \Phi^{(12)}_{lml'm'} \frac{\partial E_\phi}{\partial p} \right) \rho_{l,l'} \Bigg\} d\theta d\phi, \end{aligned} \tag{6.24}$$

$$\frac{\partial J^{(21)}_{lml'm'}}{\partial p} = \iint \alpha_{lml'm'} \Bigg\{ \left[\frac{\partial R^{(21)}_{lml'm'}}{\partial r} + (\Theta^{(21)}_{lml'm'} E_\theta + \Phi^{(21)}_{lml'm'} E_\phi) \frac{\partial \rho_{l,l'}}{\partial r} \right] \frac{\partial r}{\partial p} + \left(\Theta^{(21)}_{lml'm'} \frac{\partial E_\theta}{\partial p} + \Phi^{(21)}_{lml'm'} \frac{\partial E_\phi}{\partial p} \right) \rho_{l,l'} \Bigg\} d\theta d\phi, \tag{6.25}$$

$$\frac{\partial J^{(22)}_{lml'm'}}{\partial p} = \iint \alpha_{lml'm'} \Bigg\{ \left[\frac{\partial R^{(22)}_{lml'm'}}{\partial r} + \frac{\partial \Theta^{(22)}_{lml'm'}}{\partial r} E_\theta + \frac{\partial \Phi^{(22)}_{lml'm'}}{\partial r} E_\phi \right] \frac{\partial r}{\partial p} + \Theta^{(22)}_{lml'm'} \frac{\partial E_\theta}{\partial p} + \Phi^{(22)}_{lml'm'} \frac{\partial E_\phi}{\partial p} \Bigg\} d\theta d\phi, \tag{6.26}$$

where we have defined:

$$\alpha_{lml'm'} = \frac{(-1)^m (1 + (-1)^{m'-m})(1 + (-1)^{l'+l+1}}{2\sqrt{l(l+1)l'(l'+1)}} e^{i(m'-m)\phi} \tag{6.27}$$

k and k_s are the k vectors of light in the medium surrounding the particle, and in the particle itself. Then we define:

$$E_\theta = \frac{cos^2\phi}{a^2} + \frac{sin^2\phi}{b^2} - \frac{1}{c^2}, s \tag{6.28}$$

$$E_\phi = \frac{1}{b^2} - \frac{1}{a^2}, \tag{6.29}$$

$$\rho_{l,l'} = r^3 j_{l'} b_l, \tag{6.30}$$

Now, we can define the specific terms used to construct each J surface integral. For $J^{(12)}$, we define:

$$\frac{\partial R^{(12)}_{lml'm'}}{\partial r} = \frac{sin\theta}{k} (mm' \pi_{l'm'} \pi_{lm} + \tau_{l'm'} \tau_{lm}) \Bigg(j_{l'} \frac{\partial (krb_l)}{\partial (kr)} + r \left(k_s \frac{\partial j_{l'}}{\partial r} \frac{\partial (krb_l)}{\partial (kr)} + k j_{l'} \frac{\partial}{\partial r} \left(\frac{\partial (krb_l)}{\partial (kr)} \right) \right) \Bigg), \tag{6.31}$$

$$\Theta^{(12)}_{lml'm'} = -\frac{sin\theta}{k} l(l+1) P_l^{|m|} \tau_{l'm'}, \tag{6.32}$$

$$\Phi^{(12)}_{lml'm'} = -i \frac{sin\theta}{k} l(l+1) m' P_l^{|m|} \pi_{l'm'}. \tag{6.33}$$

For $J^{(21)}$, we define:

$$\frac{\partial R^{(21)}_{lml'm'}}{\partial r} = -\frac{sin\theta}{k_s} (mm' \pi_{l'm'} \pi_{lm} + \tau_{l'm'} \tau_{lm}) \Bigg(\frac{\partial (k_s r j_{l'})}{\partial (k_s r)} b_l + r \left(k_s \frac{\partial}{\partial r} \left(\frac{\partial (k_s r j_{l'})}{\partial (k_s r)} \right) b_l + k \frac{\partial b_l}{\partial r} \frac{\partial (k_s r j_{l'})}{\partial (k_s r)} \right) \Bigg), \tag{6.34}$$

$$\Theta^{(21)}_{lml'm'} = \frac{sin\theta}{k_s} l'(l'+1) P_{l'}^{|m'|} \tau_{lm}, \tag{6.35}$$

$$\Phi^{(21)}_{lml'm'} = -i\frac{sin\theta}{k_s} l'(l'+1) m P_{l'}^{|m'|} \pi_{lm}. \tag{6.36}$$

Finally, for $J^{(22)}$ we define:

$$\begin{aligned}\Theta^{(22)}_{lml'm'} =& i\frac{r^2 sin\theta}{kk_s}\Bigg(m'l(l+1)\frac{\partial(k_s r j_{l'})}{\partial(k_s r)} b_l P_l^{|m|}\pi_{l'm'} \\ &+ ml'(l'+1) j_{l'}\frac{\partial(krb_l)}{\partial(kr)} P_{l'}^{|m'|}\pi_{lm}\Bigg)\end{aligned} \tag{6.37}$$

$$\begin{aligned}\Phi^{(22)}_{lml'm'} =& \frac{r^2 sin\theta}{kk_s}\Bigg(l'(l'+1) j_{l'} P_{l'}^{|m'|}\frac{\partial(krb_l)}{\partial(kr)}\tau_{lm} \\ &- l(l+1)\frac{\partial(k_s r j_{l'})}{\partial(k_s r)}\tau_{l'm'} b_l P_{lm}\Bigg)\end{aligned} \tag{6.38}$$

and the three derivative terms:

$$\begin{aligned}\frac{\partial R^{(22)}_{lml'm'}}{\partial r} =& -i\frac{sin\theta}{kk_s}(m'\pi_{l'm'}\tau_{lm} + m\pi_{lm}\tau_{l'm'}) \\ &\left(k\frac{\partial}{\partial r}\left(\frac{\partial(krb_l)}{\partial(kr)}\right)\frac{\partial(k_s r j_{l'})}{\partial(k_s r)}\right. \\ &\left.+ k_s\frac{\partial}{\partial r}\left(\frac{\partial(k_s r j_{l'})}{\partial(k_s r)}\right)\frac{\partial(krb_l)}{\partial(kr)}\right)\end{aligned} \tag{6.39}$$

$$\begin{aligned}\frac{\partial\Theta^{(22)}_{lml'm'}}{\partial r} =& i\frac{sin\theta}{kk_s}\Bigg(ml'(l'+1)P_{l'}^{|m'|}\pi_{lm}\Bigg(2r\frac{\partial(krb_l)}{\partial(kr)} j_{l'} \\ &+ r^2\left(k\frac{\partial}{\partial r}\left(\frac{\partial(krb_l)}{\partial(kr)}\right) j_{l'} + k_s\frac{\partial j_{l'}}{\partial r}\frac{\partial(krb_l)}{\partial(kr)}\right)\Bigg) \\ &+ m'l(l+1)P_l^{|m|}\tau l'm'\Bigg(2rb_l\frac{\partial(k_s r j_{l'})}{\partial(k_s r)} \\ &+ r^2\left(k\frac{\partial b_l}{\partial r}\frac{\partial(k_s r j_{l'})}{\partial(k_s r)} + k_s b_l\frac{\partial}{\partial r}\left(\frac{\partial(k_s r j_{l'})}{\partial(k_s r)}\right)\right)\Bigg)\Bigg)\end{aligned} \tag{6.40}$$

$$\begin{aligned}\frac{\partial\Phi^{(22)}_{lml'm'}}{\partial r} =&\frac{sin\theta}{kk_s}\Bigg(l'(l'+1)P_{l'}^{|m'|}\tau_{lm}\Bigg(2r\frac{\partial(krb_l)}{\partial(kr)}j_{l'}\\&+r^2\Bigg(\frac{\partial}{\partial r}\left(\frac{\partial(krb_l)}{\partial(kr)}\right)j_{l'}+k_s\frac{\partial j_{l'}}{\partial r}\frac{\partial(krb_l)}{\partial(kr)}\Bigg)\Bigg)\\&-l(l+1)P_l^{|m|}\tau_{l'm'}\Bigg(2rb_l\frac{\partial(k_srj_{l'})}{\partial(k_sr)}\\&+r^2\Bigg(k\frac{\partial b_l}{\partial r}\frac{\partial(k_srj_{l'})}{\partial(k_sr)}\frac{\partial}{\partial r}\left(\frac{\partial(k_srj_{l'})}{\partial(k_sr)}\right)\Bigg)\Bigg)\Bigg).\end{aligned} \tag{6.41}$$

Now with these J integrals, we can compute the quantity $\frac{\partial T}{\partial p}$ for a given axis of an ellipsoid in its own particle frame where a, b, and c are aligned along the x_{part}, y_{part}, and z_{part} axes.

In addition to computing the response of the T-matrix of the ellipsoid to the contraction or extension of one of its axes, we are also interested in its response to rotations about the z_{part} axis. To do this we will first define the transformation of the T-matrix or a derivative matrix from the particle frame to some rotated lab frame that has new axes x_{lab} and y_{lab}, but shares $z_{lab} = z_{part}$. Given some rotation angle ϕ_{rot}, we can then define our new axes:

$$x_{lab} = x_{part}cos(\phi_{rot}) + y_{part}sin(\phi_{rot}) \tag{6.42a}$$

$$y_{lab} = -x_{part}sin(\phi_{rot}) + y_{part}cos(\phi_{rot}) \tag{6.42b}$$

$$z_{lab} = z_{part} \tag{6.42c}$$

The general form of this orthogonal transformation in three dimensions can be represented by the Euler angles α, β, and γ. The general transformation of an element of an operator O from the particle frame to the lab frame can be written as [111]:

$$O^{lab}_{plmp'l'm'}(\alpha,\beta,\gamma) = \sum_{m_1=-l}^{l}\sum_{m_2=-l'}^{l'} D^l_{mm_1}(\alpha,\beta,\gamma)O^{particle}_{plm_1p'l'm_2}D^{l'}_{m_2m'}(-\gamma,-\beta,-\alpha), \tag{6.43}$$

where the D operator is a Wigner D-function. It can be represented as:

$$D^l_{m'm}(\alpha,\beta,\gamma) = e^{-im'\alpha}d^l_{m'm}(\beta)e^{-im\gamma}, \tag{6.44}$$

where $d^l_{m'm}(\beta)$ is Wigner's (small) d-matrix given by:

$$d^l_{m'm}(\beta) = \langle l,m'|\, e^{-i\beta J_y}\, |l,m\rangle\,. \tag{6.45}$$

However, as we are only concerned with rotations about the z axis, we can simplify our expressions knowing that α is our only nonzero angle, and equation (6.43) becomes:

$$O^{lab}_{plmp'l'm'}(\alpha,0,0) = \sum_{m_1=-l}^{l}\sum_{m_2=-l'}^{l'} D^{l}_{mm_1}(\alpha,0,0)O^{particle}_{plm_1,p'l'm_2}D^{l'}_{m_2m'}(0,0,-\alpha). \tag{6.46}$$

In this case, our D operator has a much simplified form:

$$D^{l}_{m'm}(\alpha,0,0) = e^{-im'\alpha}\delta_{m'm} \tag{6.47a}$$

$$D^{l}_{m'm}(0,0,\gamma) = e^{-im\gamma}\delta_{m'm}. \tag{6.47b}$$

Combining equations (6.46), (6.47a), and (6.47b), we obtain a simple expression transforming O from the particle frame to the lab frame:

$$O^{lab}_{plmp'l'm'}(\alpha) = e^{i(m'-m)\alpha}O^{particle}_{plmp'l'm'}. \tag{6.48}$$

Equation (6.48) allows us to transform both T-matrices and the derivative matrices computed in the particle frame into the lab frame. It also gives us a prescription for computing the derivative matrix with respect to the particle's angular orientation. We already have derivatives characterizing the response of the particle to contractions and extensions of its principal axes, and can now rotate these to a lab frame where the particle has an arbitrary angular orientation relative to the z axis. We can now compute the derivative with respect to the particle's angular orientation α as:

$$\frac{\partial T^{lab}_{plmp'l'm'}(\alpha)}{\partial\alpha} = i(m'-m)e^{i(m'-m)\alpha}T^{particle}_{plmp'l'm'}. \tag{6.49}$$

With Equations (6.18) and (6.49), we have characterized the derivatives of the T-matrix representing an ellipsoid with respect to its axes and orientation.

6.4 Results

These integrals are implemented in MATLAB, and performed using Gaussian quadrature. The integrals are numerically verified by comparing the numerical derivative with the computed analytical derivative for different step sizes. For the axes a, b, and c, we find that the

error decreases as expected as the step size is decreased as shown in Figures 6.1. In addition, we find similar behavior for the angular derivative with respect to the angle α in Figure 6.2.

6.5 Conclusion

In this final section, we have shown the derivation of an expression for the computation for the derivatives of the T-matrix of an ellipsoidal scatterer. The T-matrix method is capable of handling the scattering properties of particles with arbitrary geometry, provided a surface can be parameterized in spherical coordinates. By implementing the derivatives of the T-matrix, we can extend the optimization method based on GLMT shown in Chapters 4 and 5 previously to arrays of particles with arbitrary geometry. This step can further increase the functionality of the optimization method to allow scatterer geometries that can utilize different materials and fabrication methods.

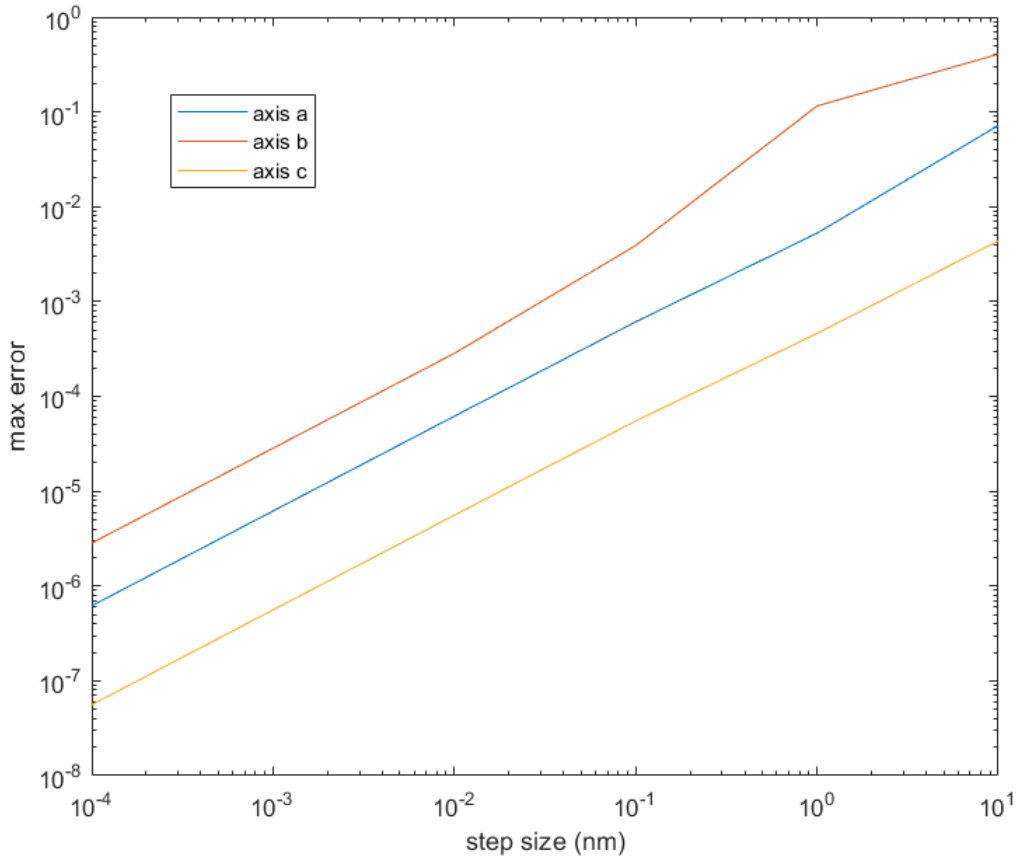

Figure 6.1: Maximum error of an element of the analytical derivative with respect to the axes a, b, and c plotted against the step size. The error in a, b, c are shown in blue, red, and yellow respectively. This is computed for an ellipsoid with $a = 400$ nm, $b = 300$ nm, $c = 500$ nm with refractive index $n = 3$, and background index $n_i = 1$ and incident wavelength $\lambda = 1000$ nm.

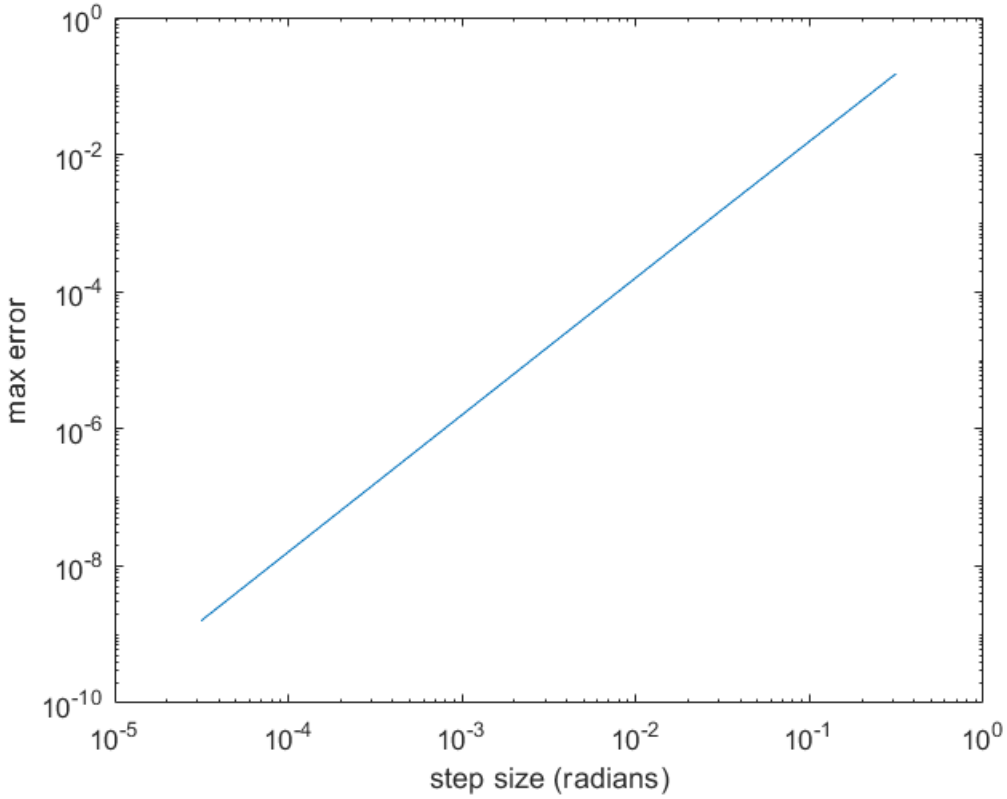

Figure 6.2: Maximum error of an element of the analytical derivative with respect to the angle α plotted against the step size in radians. This is computed for an ellipsoid with $a = 400$ nm, $b = 300$ nm, $c = 500$ nm with refractive index $n = 3$, and background index $n_i = 1$ and incident wavelength $\lambda = 1000$ nm.

Chapter 7

CONCLUSION AND OUTLOOK

Metasurface optics provides a powerful platform for wavefront manipulation by allowing high efficiency operation while exerting control over the propagation of incident light. Over the course of the timeline of this thesis (2014 to 2019), there has been an explosion of research in the development and study of optical metasurfaces due to their ability to mimic and miniaturize existing optical elements and systems, in addition to providing functionalities that do not exist in conventional optics. This breadth of capabilities lies in the large numbers of modifiable degrees of freedom that characterizes these large, coupled systems of discrete scatterers. In this thesis, I described and utilized both forward and inverse methods to aid in the design and optimization of metasurfaces. Rapidly accelerating research in both forward and inverse-design methods have resulted in a great deal of theoretical designs and experimental demonstrations of metasurfaces with improved performance or new functionalities relative to conventional optics. However, despite these advancements there are still many challenging problems to address in both device design, and method implementation.

There are a few outstanding challenges in device design relating specifically to high performance lenses that include efficient, high-numerical-aperture operation [114], chromatic aberration correction [52,53,55,61], and geometric aberration correction [62]. A wide variety of approaches have been demonstrated including both forward and inverse-design methods [75, 80, 100] to attempt to solve these problems. These approaches have yielded some success in solving these problems independently, but to date it has been difficult to design a lens or lens system that is able to incorporate all of these desirable qualities akin to a miniaturized microscope objective. In particular, it could be even more difficult to solve these problems using a material that is transparent to visible wavelengths [115], as the lower

refractive index materials tend to have comparably poor parameter sets relative to the higher index materials available for infrared operation. Solving these problems would likely require a better understanding and usage of the available degrees of freedom in these complicated optical systems, and a combination of both forward and inverse design methods.

Another exciting challenge is the realization of volume optics [78] where a three-dimensional volume of scatterers is designed to implement new functions. At this point it is well known that a two-dimensional surface is unable to generate any arbitrary pattern, and is limited in its potential input and output fields [77]. Preliminary results based on very low contrast volumes have demonstrated angular and spectral multiplexing [78], and some inverse design methods have shown compatibility with optimizing fully three dimensional structures [75]. In addition to this computational advancement, there has been rapid development in fabrication technologies capable of realizing three-dimensional nanostructures such as the Nanoscribe GT, which has been shown to be capable of fabricating high quality optical components [108, 109]. The wealth of computational electromagnetics techniques developed in the metasurface community would be applicable to those of metamaterials as well. Volume optical elements are truly exciting because they break with the common dogma of conventional optical element design (of which metasurfaces are currently constrained by). With the addition of a third spatial dimension, fully non-paraxial optics will be required to accurately characterize the system, and with this opens new possibilities of optical design that are not constrained to merely two-dimensional planes for the input, operation, and output.

On the method development side, the use of inverse design methods in computational electromagnetics is still in relative infancy, and has great potential for the design of two-dimensional surfaces, and three-dimensional volumes. Currently, the dominant techniques involve solving Maxwell's equations directly [80, 98, 100, 116], though there have been other methods, including methods that use periodic cell approximations [81, 116]. However, while these methods have shown some success, one major hurdle for inverse design demonstrations is the balancing of numerical accuracy with large area/volume designs. Methods which solve Maxwell's equations directly have extremely high numerical accuracy, but scale poorly with

higher simulation volumes. Conversely, recently developed methods which use the local phase approximation are able to handle larger volumes, but can have considerable numerical error. The method presented in this thesis has potential to be numerically accurate while still able to simulate relatively large areas and volumes. However, it is limited in its ability to simulate arbitrary structures as it requires a parameterization of continuous or piecewise continuous surfaces. In this manner it cannot nucleate new structures, or handle the splitting of individual scatterers that is possible in the other methods. Given the large degrees of complexity of volume optics systems, it is likely that inverse design techniques will be critical for their design, and this may be one topic that motivates further advancement in inverse methods. In addition, inverse methods may prove to be beneficial for exploring solutions to produce high performance metalenses with aberration corrections and large numerical aperture.

In addition to research on the appropriate theoretical basis for inverse design (finite difference methods, Mie scattering/T-matrix theory, local phase approximation etc) there is also a considerable amount of research on the method used to optimize the structure. These methods include stochastic, global-optimization methods such as particle swarm optimization, and genetic algorithms in addition to local gradient-based optimizations such as the method presented in this thesis. In addition to these methods, there has been interest in the use of neural networks in inverse design [117–119]. It is unclear if the neural network methods will be able to generalize to large area structures, though they seem to be numerically accurate and relatively fast when successfully trained. It is very possible that an amalgamation of these techniques would be required to realize a truly scalable formalism for inverse design.

Last, but certainly not least, is the field of dynamically tunable metasurfaces analogous in function to deformable micromirrors and spatial light modulators. These devices could find applications in a wide variety of applications including biological imaging, beam steering for LIDAR, and augmented or virtual reality systems. This is currently an active and exciting area of research, though there have been few experimental demonstrations. Proposed designs generally seek to modulate the refractive index at a single pixel level using mechanisms such

as the thermo-optic effect [120], electro-optic effect [121], phase change materials [122], and plasmonic resonances [123]. Here the key goal is to fabricate a device that achieves a small pixel size and high modulation (MHz, GHz) frequency for phase values between 0 and 2π. This is an extremely difficult task that likely requires combined expertise from materials scientists, optical and electrical engineers, and optical and condensed matter physicists.

BIBLIOGRAPHY

[1] Amir Arbabi, Yu Horie, Alexander J. Ball, Mahmood Bagheri, and Andrei Faraon. Subwavelength-thick lenses with high numerical apertures and large efficiency based on high-contrast transmitarrays. *Nature Communications*, 6:7069 EP –, May 2015. Article.

[2] JAY M. ENOCH. History of mirrors dating back 8000 years. *Optometry and Vision Science*, 83(10), 2006.

[3] Timothy C. Kriss and Vesna Martich Kriss. History of the operating microscope: From magnifying glass to microneurosurgery. *Neurosurgery*, 42(4):899–907, Apr 1998.

[4] David C. Lindberg. Alhazen's theory of vision and its reception in the west. *Isis*, 58(3):321–341, Oct 1967.

[5] Richard Davies and Markus Kasper. Adaptive optics for astronomy. *Annual Review of Astronomy and Astrophysics*, 50(1):305–351, 2012.

[6] Lothar Schermelleh, Alexia Ferrand, Thomas Huser, Christian Eggeling, Markus Sauer, Oliver Biehlmaier, and Gregor P. C. Drummen. Super-resolution microscopy demystified. *Nature Cell Biology*, 21(1):72–84, 2019.

[7] Nanfang Yu and Federico Capasso. Flat optics with designer metasurfaces. *Nature Materials*, 13:139 EP –, Jan 2014. Review Article.

[8] Patrice Genevet, Federico Capasso, Francesco Aieta, Mohammadreza Khorasaninejad, and Robert Devlin. Recent advances in planar optics: from plasmonic to dielectric metasurfaces. *Optica*, 4(1):139–152, 2017.

[9] Philippe Lalanne and Pierre Chavel. Metalenses at visible wavelengths: past, present, perspectives. *Laser & Photonics Reviews*, 11(3):1600295, May 2017.

[10] Kamali Seyedeh Mahsa, Arbabi Ehsan, Arbabi Amir, and Faraon Andrei. *nanoph*, volume 7, chapter A review of dielectric optical metasurfaces for wavefront control, page 1041. 2019 2018. 6.

[11] Alexander V. Kildishev, Alexandra Boltasseva, and Vladimir M. Shalaev. Planar photonics with metasurfaces. *Science*, 339(6125):1232009, Mar 2013.

[12] W. Stork, N. Streibl, H. Haidner, and P. Kipfer. Artificial distributed-index media fabricated by zero-order gratings. *Opt. Lett.*, 16(24):1921–1923, Dec 1991.

[13] Michael W. Farn. Binary gratings with increased efficiency. *Applied Optics*, 31(22):4453–4458, 1992.

[14] Philippe Lalanne, Simion Astilean, Pierre Chavel, Edmond Cambril, and Huguette Launois. Design and fabrication of blazed binary diffractive elements with sampling periods smaller than the structural cutoff. *Journal of the Optical Society of America A*, 16(5):1143–1156, 1999.

[15] D. E. Aspnes. Local-field effects and effective-medium theory: A microscopic perspective. *American Journal of Physics*, 50(8):704–709, 1982.

[16] Philippe Lalanne and Dominique Lemercier-lalanne. On the effective medium theory of subwavelength periodic structures. *Journal of Modern Optics*, 43(10):2063–2085, Oct 1996.

[17] D. Mikolas, R. Bojko, H. G. Craighead, F. Haas, D. A. Honey, and H. F. Bare. Fabrication of aspheric high numerical aperture reflective diffractive optic elements using electron beam lithography. *Journal of Vacuum Science & Technology B: Microelectronics and Nanometer Structures Processing, Measurement, and Phenomena*, 12(1):20–25, Jan 1994.

[18] F. T. Chen and H. G. Craighead. Diffractive phase elements based on two-dimensional artificial dielectrics. *Optics Letters*, 20(2):121–123, 1995.

[19] Frederick T. Chen and Harold G. Craighead. Diffractive lens fabricated with mostly zeroth-order gratings. *Optics Letters*, 21(3):177–179, 1996.

[20] Philippe Lalanne, Simion Astilean, Pierre Chavel, Edmond Cambril, and Huguette Launois. Blazed binary subwavelength gratings with efficiencies larger than those of conventional échelette gratings. *Optics Letters*, 23(14):1081–1083, 1998.

[21] Simion Astilean, Philippe Lalanne, Pierre Chavel, Edmond Cambril, and Huguette Launois. High-efficiency subwavelength diffractive element patterned in a high-refractive-index material for 633??nm. *Optics Letters*, 23(7):552–554, 1998.

[22] Philippe Lalanne. Waveguiding in blazed-binary diffractive elements. *J. Opt. Soc. Am. A*, 16(10):2517–2520, Oct 1999.

[23] M. G. Moharam, Eric B. Grann, Drew A. Pommet, and T. K. Gaylord. Formulation for stable and efficient implementation of the rigorous coupled-wave analysis of binary gratings. *J. Opt. Soc. Am. A*, 12(5):1068–1076, May 1995.

[24] M S L Lee, Ph Lalanne, J C Rodier, P Chavel, E Cambril, and Y Chen. Imaging with blazed-binary diffractive elements. *Journal of Optics A: Pure and Applied Optics*, 4(5):S119–S124, aug 2002.

[25] S. Pancharatnam. Generalized theory of interference, and its applications. *Proceedings of the Indian Academy of Sciences - Section A*, 44(5):247–262, Nov 1956.

[26] Berry Michael Victor. Quantal phase factors accompanying adiabatic changes. *Proceedings of the Royal Society of London. A. Mathematical and Physical Sciences*, 392(1802):45–57, Mar 1984.

[27] Ze'ev Bomzon, Gabriel Biener, Vladimir Kleiner, and Erez Hasman. Space-variant pancharatnam–berry phase optical elements with computer-generated subwavelength gratings. *Opt. Lett.*, 27(13):1141–1143, Jul 2002.

[28] Ze'ev Bomzon, Vladimir Kleiner, and Erez Hasman. Pancharatnam–berry phase in space-variant polarization-state manipulations with subwavelength gratings. *Opt. Lett.*, 26(18):1424–1426, Sep 2001.

[29] J. B. Pendry, A. J. Holden, W. J. Stewart, and I. Youngs. Extremely low frequency plasmons in metallic mesostructures. *Phys. Rev. Lett.*, 76:4773–4776, Jun 1996.

[30] J. B. Pendry, D. Schurig, and D. R. Smith. Controlling electromagnetic fields. *Science*, 312(5781):1780–1782, 2006.

[31] Xingjie Ni, Satoshi Ishii, Alexander V. Kildishev, and Vladimir M. Shalaev. Ultra-thin, planar, babinet-inverted plasmonic metalenses. *Light: Science &Amp; Applications*, 2:e72 EP –, Apr 2013. Original Article.

[32] Francesco Aieta, Patrice Genevet, Mikhail A. Kats, Nanfang Yu, Romain Blanchard, Zeno Gaburro, and Federico Capasso. Aberration-free ultrathin flat lenses and axicons at telecom wavelengths based on plasmonic metasurfaces. *Nano Letters*, 12(9):4932–4936, Sep 2012.

[33] Mohammadreza Khorasaninejad, Antonio Ambrosio, Pritpal Kanhaiya, and Federico Capasso. Broadband and chiral binary dielectric meta-holograms. *Science Advances*, 2(5):e1501258, May 2016.

[34] Xingjie Ni, Alexander V. Kildishev, and Vladimir M. Shalaev. Metasurface holograms for visible light. *Nature Communications*, 4:2807 EP –, Nov 2013. Article.

[35] Ehsan Arbabi, Amir Arbabi, Seyedeh Mahsa Kamali, Yu Horie, and Andrei Faraon. Multiwavelength polarization-insensitive lenses based on dielectric metasurfaces with meta-molecules. *Optica*, 3(6):628–633, 2016.

[36] Ehsan Arbabi, Amir Arbabi, Seyedeh Mahsa Kamali, Yu Horie, and Andrei Faraon. High efficiency double-wavelength dielectric metasurface lenses with dichroic birefringent meta-atoms. *Optics Express*, 24(16):18468–18477, 2016.

[37] Ehsan Arbabi, Jiaqi Li, Romanus J. Hutchins, Seyedeh Mahsa Kamali, Amir Arbabi, Yu Horie, Pol Van Dorpe, Viviana Gradinaru, Daniel A. Wagenaar, and Andrei Faraon. Two-photon microscopy with a double-wavelength metasurface objective lens. *Nano Letters*, 18(8):4943–4948, Aug 2018.

[38] Mohammadreza Khorasaninejad, Wei Ting Chen, Robert C. Devlin, Jaewon Oh, Alexander Y. Zhu, and Federico Capasso. Metalenses at visible wavelengths: Diffraction-limited focusing and subwavelength resolution imaging. *Science*, 352(6290):1190, Jun 2016.

[39] Francesco Aieta, Mikhail A. Kats, Patrice Genevet, and Federico Capasso. Multiwavelength achromatic metasurfaces by dispersive phase compensation. *Science*, 347(6228):1342, Mar 2015.

[40] M. Khorasaninejad, A. Y. Zhu, C. Roques-Carmes, W. T. Chen, J. Oh, I. Mishra, R. C. Devlin, and F. Capasso. Polarization-insensitive metalenses at visible wavelengths. *Nano Letters*, 16(11):7229–7234, Nov 2016.

[41] M. Khorasaninejad, Z. Shi, A. Y. Zhu, W. T. Chen, V. Sanjeev, A. Zaidi, and F. Capasso. Achromatic metalens over 60 nm bandwidth in the visible and metalens with reverse chromatic dispersion. *Nano Letters*, 17(3):1819–1824, Mar 2017.

[42] David Fattal, Jingjing Li, Zhen Peng, Marco Fiorentino, and Raymond G. Beausoleil. Flat dielectric grating reflectors with focusing abilities. *Nature Photonics*, 4:466 EP –, May 2010.

[43] Dianmin Lin, Pengyu Fan, Erez Hasman, and Mark L. Brongersma. Dielectric gradient metasurface optical elements. *Science*, 345(6194):298, Jul 2014.

[44] Xingjie Ni, Naresh K. Emani, Alexander V. Kildishev, Alexandra Boltasseva, and Vladimir M. Shalaev. Broadband light bending with plasmonic nanoantennas. *Science*, 335(6067):427, Jan 2012.

[45] M. Khorasaninejad, W. T. Chen, A. Y. Zhu, J. Oh, R. C. Devlin, D. Rousso, and F. Capasso. Multispectral chiral imaging with a metalens. *Nano Letters*, 16(7):4595–4600, Jul 2016.

[46] Shane Colburn, Alan Zhan, and Arka Majumdar. Varifocal zoom imaging with large area focal length adjustable metalenses. *Optica*, 5(7):825–831, Jul 2018.

[47] Alan Zhan, Shane Colburn, Christopher M. Dodson, and Arka Majumdar. Metasurface freeform nanophotonics. *Scientific Reports*, 7(1):1673, 2017.

[48] Amir Arbabi, Ehsan Arbabi, Yu Horie, Seyedeh Mahsa Kamali, and Andrei Faraon. Planar metasurface retroreflector. *Nature Photonics*, 11:415 EP –, Jun 2017.

[49] Amir Arbabi, Yu Horie, Mahmood Bagheri, and Andrei Faraon. Dielectric metasurfaces for complete control of phase and polarization with subwavelength spatial resolution and high transmission. *Nature Nanotechnology*, 10:937 EP –, Aug 2015.

[50] Nanfang Yu, Francesco Aieta, Patrice Genevet, Mikhail A. Kats, Zeno Gaburro, and Federico Capasso. A broadband, background-free quarter-wave plate based on plasmonic metasurfaces. *Nano Letters*, 12(12):6328–6333, Dec 2012.

[51] Seyedeh Mahsa Kamali, Ehsan Arbabi, Amir Arbabi, Yu Horie, MohammadSadegh Faraji-Dana, and Andrei Faraon. Angle-multiplexed metasurfaces: Encoding independent wavefronts in a single metasurface under different illumination angles. *Phys. Rev. X*, 7:041056, Dec 2017.

[52] Shuming Wang, Pin Chieh Wu, Vin-Cent Su, Yi-Chieh Lai, Mu-Ku Chen, Hsin Yu Kuo, Bo Han Chen, Yu Han Chen, Tzu-Ting Huang, Jung-Hsi Wang, Ray-Ming Lin, Chieh-Hsiung Kuan, Tao Li, Zhenlin Wang, Shining Zhu, and Din Ping Tsai. A broadband achromatic metalens in the visible. *Nature Nanotechnology*, 13(3):227–232, 2018.

[53] Shuming Wang, Pin Chieh Wu, Vin-Cent Su, Yi-Chieh Lai, Cheng Hung Chu, Jia-Wern Chen, Shen-Hung Lu, Ji Chen, Beibei Xu, Chieh-Hsiung Kuan, Tao Li, Shining Zhu, and Din Ping Tsai. Broadband achromatic optical metasurface devices. *Nature Communications*, 8(1):187, 2017.

[54] Ehsan Arbabi, Amir Arbabi, Seyedeh Mahsa Kamali, Yu Horie, and Andrei Faraon. Controlling the sign of chromatic dispersion in diffractive optics with dielectric metasurfaces. *Optica*, 4(6):625–632, 2017.

[55] Wei Ting Chen, Alexander Y. Zhu, Vyshakh Sanjeev, Mohammadreza Khorasaninejad, Zhujun Shi, Eric Lee, and Federico Capasso. A broadband achromatic metalens for focusing and imaging in the visible. *Nature Nanotechnology*, 13(3):220–226, 2018.

[56] Mohammadreza Khorasaninejad, Francesco Aieta, Pritpal Kanhaiya, Mikhail A. Kats, Patrice Genevet, David Rousso, and Federico Capasso. Achromatic metasurface lens at telecommunication wavelengths. *Nano Letters*, 15(8):5358–5362, Aug 2015.

[57] Ramón Paniagua-Domínguez, Ye Feng Yu, Andrey E. Miroshnichenko, Leonid A. Krivitsky, Yuan Hsing Fu, Vytautas Valuckas, Leonard Gonzaga, Yeow Teck Toh, Anthony Yew Seng Kay, Boris Luk'yanchuk, and Arseniy I. Kuznetsov. Generalized brewster effect in dielectric metasurfaces. *Nature Communications*, 7:10362 EP –, Jan 2016. Article.

[58] MohammadSadegh Faraji-Dana, Ehsan Arbabi, Amir Arbabi, Seyedeh Mahsa Kamali, Hyounghan Kwon, and Andrei Faraon. Compact folded metasurface spectrometer. *Nature Communications*, 9(1):4196, 2018.

[59] Mooseok Jang, Yu Horie, Atsushi Shibukawa, Joshua Brake, Yan Liu, Seyedeh Mahsa Kamali, Amir Arbabi, Haowen Ruan, Andrei Faraon, and Changhuei Yang. Wavefront shaping with disorder-engineered metasurfaces. *Nature Photonics*, 12(2):84–90, 2018.

[60] Hyounghan Kwon, Ehsan Arbabi, Seyedeh Mahsa Kamali, MohammadSadegh Faraji-Dana, and Andrei Faraon. Computational complex optical field imaging using a designed metasurface diffuser. *Optica*, 5(8):924–931, 2018.

[61] Shane Colburn, Alan Zhan, and Arka Majumdar. Metasurface optics for full-color computational imaging. *Science Advances*, 4(2), 2018.

[62] Amir Arbabi, Ehsan Arbabi, Seyedeh Mahsa Kamali, Yu Horie, Seunghoon Han, and Andrei Faraon. Miniature optical planar camera based on a wide-angle metasurface doublet corrected for monochromatic aberrations. *Nature Communications*, 7:13682 EP –, Nov 2016. Article.

[63] Alan Zhan, Shane Colburn, Rahul Trivedi, Taylor K. Fryett, Christopher M. Dodson, and Arka Majumdar. Low-contrast dielectric metasurface optics. *ACS Photonics*, 3(2):209–214, 2016.

[64] Joseph W. Goodman. *Introduction to Fourier Optics*. McGraw Hill.

[65] Ilhan Kaya, Kevin P. Thompson, and Jannick P. Rolland. Comparative assessment of freeform polynomials as optical surface descriptions. *Optics Express*, 20(20):22683–22691, 2012.

[66] Kyle Fuerschbach, Jannick P. Rolland, and Kevin P. Thompson. Theory of aberration fields for general optical systems with freeform surfaces. *Optics Express*, 22(22):26585–26606, 2014.

[67] Kyle Fuerschbach, Gregg E. Davis, Kevin P. Thompson, and Jannick P. Rolland. Assembly of a freeform off-axis optical system employing three φ-polynomial zernike mirrors. *Optics Letters*, 39(10):2896–2899, 2014.

[68] Fabian Duerr, Youri Meuret, and Hugo Thienpont. Potential benefits of free-form optics in on-axis imaging applications with high aspect ratio. *Optics Express*, 21(25):31072–31081, 2013.

[69] Edward R. Dowski and W. Thomas Cathey. Extended depth of field through wave-front coding. *Applied Optics*, 34(11):1859–1866, 1995.

[70] Ian M. Barton, Sham N. Dixit, Leslie J. Summers, Charles A. Thompson, Kenneth Avicola, and Julia Wilhelmsen. Diffractive alvarez lens. *Optics Letters*, 25(1):1–3, 2000.

[71] Guangya Zhou, Hongbin Yu, and Fook Siong Chau. Microelectromechanically-driven miniature adaptive alvarez lens. *Optics Express*, 21(1):1226–1233, 2013.

[72] Likai Li, Thomas W. Raasch, Ingo Sieber, Erik Beckert, Ralf Steinkopf, Ulrich Gengenbach, and Allen Y. Yi. Fabrication of microinjection-molded miniature freeform alvarez lenses. *Applied Optics*, 53(19):4248–4255, 2014.

[73] Sergio Barbero. The alvarez and lohmann refractive lenses revisited. *Optics Express*, 17(11):9376–9390, 2009.

[74] Sara C. Tucker, W. Thomas Cathey, and Edward R. Dowski. Extended depth of field and aberration control for inexpensive digital microscope systems. *Opt. Express*, 4(11):467–474, May 1999.

[75] Alan Zhan, Taylor K. Fryett, Shane Colburn, and Arka Majumdar. Inverse design of optical elements based on arrays of dielectric spheres. *Appl. Opt.*, 57(6):1437–1446, Feb 2018.

[76] Zhaocheng Liu, Dayu Zhu, Sean P. Rodrigues, Kyu-Tae Lee, and Wenshan Cai. Generative model for the inverse design of metasurfaces. *Nano Letters*, 18(10):6570–6576, Oct 2018.

[77] Rafael Piestun, Boris Spektor, and Joseph Shamir. Wave fields in three dimensions: analysis and synthesis. *Journal of the Optical Society of America A*, 13(9):1837–1848, 1996.

[78] Tim D. Gerke and Rafael Piestun. Aperiodic volume optics. *Nature Photonics*, 4:188 EP –, Feb 2010. Article.

[79] Jierong Cheng, Sandeep Inampudi, and Hossein Mosallaei. Optimization-based dielectric metasurfaces for angle-selective multifunctional beam deflection. *Scientific Reports*, 7(1):12228, 2017.

[80] David Sell, Jianji Yang, Sage Doshay, Rui Yang, and Jonathan A. Fan. Large-angle, multifunctional metagratings based on freeform multimode geometries. *Nano Letters*, 17(6):3752–3757, Jun 2017.

[81] Raphaël Pestourie, Carlos Pérez-Arancibia, Zin Lin, Wonseok Shin, Federico Capasso, and Steven G. Johnson. Inverse design of large-area metasurfaces. *Opt. Express*, 26(26):33732–33747, Dec 2018.

[82] Victor Egorov, Michal Eitan, and Jacob Scheuer. Genetically optimized all-dielectric metasurfaces. *Optics Express*, 25(3):2583–2593, 2017.

[83] Massimo Donelli. Design of broadband metal nanosphere antenna arrays with a hybrid evolutionary algorithm. *Optics Letters*, 38(4):401–403, 2013.

[84] Raphaël Pestourie, Carlos Pérez-Arancibia, Zin Lin, Wonseok Shin, Federico Capasso, and Steven G. Johnson. Inverse design of large-area metasurfaces. *Optics Express*, 26(26):33732–33747, 2018.

[85] Martin Philip Bendsøe and Noboru Kikuchi. Generating optimal topologies in structural design using a homogenization method. *Computer Methods in Applied Mechanics and Engineering*, 71(2):197–224, 1988.

[86] Jesse Lu and Jelena Vuckovic. Inverse design of nanophotonic structures using complementary convex optimization. *Optics Express*, 18(4):3793–3804, 2010.

[87] Sean Molesky, Zin Lin, Alexander Y. Piggott, Weiliang Jin, Jelena Vuckovic, and Alejandro W. Rodriguez. Inverse design in nanophotonics. *Nature Photonics*, 12(11):659–670, 2018.

[88] R. D. Carter, L. F. Kemp, A. C. Piece, and D. L. Williams. Performance matching with constraints. *Soc. Pet. Eng. J.*, 14:74–86, 1974.

[89] W. H. Chavent, M. Dupuy, and P. Lemonnier. History matching by use of optimal theory. *Soc. Pet. Eng. J.*, 15:593–608, 1975.

[90] N. K. Georgieva, S. Glavic, M. H. Bakr, and J. W. Bandler. Feasible adjoint sensitivity technique for em design optimization. *IEEE Transactions on Microwave Theory and Techniques*, 50(12):2751–2758, 2002.

[91] Christopher M. Lalau-Keraly, Samarth Bhargava, Owen D. Miller, and Eli Yablonovitch. Adjoint shape optimization applied to electromagnetic design. *Optics Express*, 21(18):21693–21701, 2013.

[92] Alexander Y. Piggott, Jan Petykiewicz, Logan Su, and Jelena Vuckovic. Fabrication-constrained nanophotonic inverse design. *Scientific Reports*, 7(1):1786, 2017.

[93] Weijie Chang, Xinshu Ren, Yingquan Ao, Longhui Lu, Mengfan Cheng, Lei Deng, Deming Liu, and Minming Zhang. Inverse design and demonstration of an ultracompact broadband dual-mode 3 db power splitter. *Optics Express*, 26(18):24135–24144, 2018.

[94] Alexander Y. Piggott, Jesse Lu, Konstantinos G. Lagoudakis, Jan Petykiewicz, Thomas M. Babinec, and Jelena Vuckovic. Inverse design and demonstration of a compact and broadband on-chip wavelength demultiplexer. *Nature Photonics*, 9:374 EP –, May 2015.

[95] Bing Shen, Peng Wang, Randy Polson, and Rajesh Menon. An integrated-nanophotonics polarization beamsplitter with 2.4 x 2.4 mm2 footprint. *Nature Photonics*, 9:378 EP –, May 2015.

[96] Paul Hansen and Lambertus Hesselink. Accurate adjoint design sensitivities for nano metal optics. *Optics Express*, 23(18):23899–23923, 2015.

[97] Jianji Yang and Jonathan A. Fan. Topology-optimized metasurfaces: impact of initial geometric layout. *Optics Letters*, 42(16):3161–3164, 2017.

[98] F. Callewaert, V. Velev, P. Kumar, A. V. Sahakian, and K. Aydin. Inverse-designed broadband all-dielectric electromagnetic metadevices. *Scientific Reports*, 8(1):1358, 2018.

[99] Jianji Yang and Jonathan A. Fan. Analysis of material selection on dielectric metasurface performance. *Optics Express*, 25(20):23899–23909, 2017.

[100] Zin Lin, Benedikt Groever, Federico Capasso, Alejandro W. Rodriguez, and Marko Lončar. Topology-optimized multilayered metaoptics. *Phys. Rev. Applied*, 9:044030, Apr 2018.

[101] Daniel W. Mackowski and Michael I. Mishchenko. Calculation of the t matrix and the scattering matrix for ensembles of spheres. *Journal of the Optical Society of America A*, 13(11):2266–2278, 1996.

[102] Yu-lin Xu. Electromagnetic scattering by an aggregate of spheres. *Applied Optics*, 34(21):4573–4588, 1995.

[103] Amos Egel, Lorenzo Pattelli, Giacomo Mazzamuto, Diederik S. Wiersma, and Uli Lemmer. Celes: Cuda-accelerated simulation of electromagnetic scattering by large ensembles of spheres. *Journal of Quantitative Spectroscopy and Radiative Transfer*, 199:103–110, 2017.

[104] Seymour Stein. Addition theorems for spherical wave functions. *Quarterly of Applied Mathematics*, 19:15–24, 1961.

[105] Orval Cruzan. Translational addition theorems for spherical vector wave functions. *Quarterly of Applied Mathematics*, 20:33–40, 1962.

[106] Roy G. Grainger, Jonathan Lucas, Gareth E. Thomas, and Graham B. L. Ewen. Calculation of mie derivatives. *Applied Optics*, 43(28):5386–5393, 2004.

[107] Yang Li and Nicola Bowler. Computation of mie derivatives. *Applied Optics*, 52(20):4997–5006, 2013.

[108] Timo Gissibl, Simon Thiele, Alois Herkommer, and Harald Giessen. Two-photon direct laser writing of ultracompact multi-lens objectives. *Nature Photonics*, 10:554 EP –, Jun 2016. Article.

[109] Timo Gissibl, Simon Thiele, Alois Herkommer, and Harald Giessen. Sub-micrometre accurate free-form optics by three-dimensional printing on single-mode fibres. *Nature Communications*, 7:11763 EP –, Jun 2016. Article.

[110] P. C. Waterman. Symmetry, unitarity, and geometry in electromagnetic scattering. *Phys. Rev. D*, 3:825–839, Feb 1971.

[111] Michael I. Mishchenko, Larry D. Davis, and Andrew A. Lacis. *Scattering, Absoprtion, and Emission of Light by Small Particles*. NASA Goddard Institute for Space Studies, 2002.

[112] Adrian Doicu, Thomas Wriedt, and Jurij A. Eremin. *Light Scattering by Systems of Particles: Null-Field Method with Discrete Sources*. Springer, 2006.

[113] J. B. Schneider and I. C. Peden. Differential cross section of a dielectric ellipsoid by the t-matrix extended boundary condition method. *IEEE Transactions on Antennas and Propagation*, 36(9):1317–1321, Sep. 1988.

[114] Steven J. Byrnes, Alan Lenef, Francesco Aieta, and Federico Capasso. Designing large, high-efficiency, high-numerical-aperture, transmissive meta-lenses for visible light. *Optics Express*, 24(5):5110–5124, 2016.

[115] Elyas Bayati, Alan Zhan, Shane Colburn, Maksym Viktorovich Zhelyeznyakov, and Arka Majumdar. Role of refractive index in metalens performance. *Appl. Opt.*, 58(6):1460–1466, Feb 2019.

[116] Thaibao Phan, David Sell, Evan W. Wang, Sage Doshay, Kofi Edee, Jianji Yang, and Jonathan A. Fan. High-efficiency, large-area, topology-optimized metasurfaces. *Light: Science & Applications*, 8(1):48, 2019.

[117] Dianjing Liu, Yixuan Tan, Erfan Khoram, and Zongfu Yu. Training deep neural networks for the inverse design of nanophotonic structures. *ACS Photonics*, 5(4):1365–1369, 2018.

[118] Mohammad H. Tahersima, Keisuke Kojima, Toshiaki Koike-Akino, Devesh Jha, Bingnan Wang, Chungwei Lin, and Kieran Parsons. Deep neural network inverse design of integrated photonic power splitters. *Scientific Reports*, 9(1):1368, 2019.

[119] John Peurifoy, Yichen Shen, Li Jing, Yi Yang, Fidel Cano-Renteria, Brendan G. DeLacy, John D. Joannopoulos, Max Tegmark, and Marin Soljačić. Nanophotonic particle simulation and inverse design using artificial neural networks. *Science Advances*, 4(6), 2018.

[120] Shane Colburn, Alan Zhan, and Arka Majumdar. Tunable metasurfaces via subwavelength phase shifters with uniform amplitude. *Scientific Reports*, 7:40174 EP –, Jan 2017. Article.

[121] Jiaqi Zhang, Yuji Kosugi, Akira Otomo, Yoshiaki Nakano, and Takuo Tanemura. Active metasurface modulator with electro-optic polymer using bimodal plasmonic resonance. *Opt. Express*, 25(24):30304–30311, Nov 2017.

[122] Qian Wang, Edward T. F. Rogers, Behrad Gholipour, Chih-Ming Wang, Guanghui Yuan, Jinghua Teng, and Nikolay I. Zheludev. Optically reconfigurable metasurfaces

and photonic devices based on phase change materials. *Nature Photonics*, 10:60 EP –, Dec 2015. Article.

[123] Alexei Smolyaninov, Abdelkrim El Amili, Felipe Vallini, Steve Pappert, and Yeshaiahu Fainman. Programmable plasmonic phase modulation of free-space wavefronts at gigahertz rates. *Nature Photonics*, 13(6):431–435, 2019.

Appendix A

FABRICATION RECIPES

Below are the fabrication procedures used for the fabrication of the thesis.

A.1 Silicon Nitride Metasurface Fabrication

We begin with a double-side polished 0.5 mm fused quartz or silica wafer.

1. Deposit 633 nm silicon nitride using PECVD2-SPTS recipe AM_SiN_LDR_350C.

2. Evaporate 50 nm aluminum at 0.1 nm/s using EVAP1. This layer serves as both a hard mask for inductively-coupled plasma (ICP) etching and charge dissapation layer for EBL.

3. Clean with acetone and isopropyl alcohol.

4. Spin a 160 nm layer of ZEP 520A 1:1 diluted in anisole.

5. Bake for two minutes at 180 C.

6. Pattern using EBL (JEOL JBX-6300 FS 100 kV).

7. Develop resist for two minutes using amyl acetate. Lightly agitate.

8. Etch for 50 seconds using ICP-Chlorine recipe RJB - Al v2. Expect dull green plasma color

9. Etch for 160 seconds using ICP-Fluorine recipe AMLAB-SiN-Etch-10C. Expect a deep pink or purple color

10. Remove aluminum hard mask using AD-10 photoresist developer

A.2 Nanoscribe Fabrication

We begin with a high resolution glass slide provided by Nanoscribe. First, any device layout that is to be used should be compiled into an .stl file. In my , this is done using Blender, a free 3D modeling software.

1. Convert .stl file into Nanoscribe .gwl files using the proprietary DeScribe software.

2. Load converted files into Nanoscribe computer.

3. Place a small bead of IP-Dip resist (a 3 mm x 3 mm bead should suffice) onto a high resolution glass slide provided by Nanoscribe.

4. Load slide into the holder.

5. Begin exposure (should take around 20-30 minutes for a 200 μm × 200 μm device.

6. Unload sample.

7. Develop in Microchem SU-8 Developer for 20 minutes.

8. Rinse with water, and dry. Be very careful when blow drying as structures can be prone to blowing off or being deformed.